Fragmentation Properties of Strange Particles Produced in High Transverse Momentum Hadronic Interactions

by

Vijay Kapoor

Submitted in Fulfillment
of the
Requirements for the Degree
DOCTOR OF PHILOSOPHY

Department of Physics and Astrophysics
University of Delhi
Delhi

October 1990

DECLARATION

This thesis deals with the fragmentation properties of strange particles produced in high transverse momentum away-side jets in interactions of 530 GeV/c π^- and proton beams on beryllium and copper targets.

Most of the work presented in this thesis has been published or is in the process of publication.

This work has been done under the supervision of Dr. R. K. Shivpuri. The work has been done by the candidate himself and, to the best of his knowledge, no part of this work has earlier been submitted for any degree or diploma of this or any other university.

(Vijay Kapoor)
Candidate

(R. K. Shivpuri)
Supervisor

Head, Dept. of Physics and Astrophysics
University of Delhi, Delhi 110007, India.

I dedicate this thesis to my

Parents

for their patience, love and support.

Acknowledgements

An experiment of size as big as E706 requires involvement from many people at all levels. Therefore, I would like to extend my gratitude to everybody who participated directly or indirectly in the success of this experiment.

My heartfelt thanks goes to all the fellow graduate students and postdocs for their friendship and with whom I had a chance to work and share knowledge. I am greatly indebted to them for their friendship. E706 is really a group of hardworking and wonderful people and they love to party as much as they love to work.

There are some people who deserves special recognition and I would like to thank them by giving their names here. First of all, I would like to thank Dr. S. Mani for helping me to choose this project and then being there until the completion of this thesis. I am personally grateful to him and I just don't have enough words to thank him. I enjoyed working with him and learned a lot.

Next person on the list is my supervisor, Dr. Ram K. Shivpuri. I would like to thank him for his continuing support, encouragement and for providing a suitable working atmosphere. I have known him for more than 10 years and during these years our relation has developed more into friendship than just another student-teacher relationship.

The other person who deserves a special recognition is Dr. George Ginther, a very energetic fellow. He is always there when you need him for any help.

I would like to thank the spokesman of this experiment, Prof. Paul Slattery for his wonderful and remarkable leadership quality and also for signing on my salary bills. My thanks goes to Prof. Tom Ferbel also for his helping nature and his love for India.

I wish to thank Prof. Carl Bromberg for introducing me to The E706 program. I just wish we had collaborated more. Another person whom I would love to thank is Prof. Gene Engels, a wonderful man. Knowing and working with him is a pleasure.

Among fellow graduate students, I would like to express my thanks to B. C. Choudhary, D. Weerasundra, K. Hartman, A. Sinanidis, C. Yosef, S. Easo, S. Kartik and D. Orris for their friendship and help.

I would also like to thank Phyllis Hale, from the Users Office, for her motherly love when I needed one. She has become my American mother since.

I also need to express my thanks to Mr. P. C. Gupta and Mr. Prem Dhingra at University of Delhi for their advice and brotherly love.

The other thing which I don't want to forget to mention is that during my stay here, I made many new wonderful friends. It gives me a great pleasure to remember that they are going to be a part of my future.

I would also like to thank University Grant Commission (UGC) and Department of Science and Technology (DST) of India for providing funds for this experiment.

Abstract

During the 1987-88 fixed target run at Fermilab*, the E706 spectrometer was exposed to both positive and negative polarity 530 GeV/c tagged hadronic beams incident on Be and Cu targets. The spectrometer triggered on high transverse momentum (p_T) electromagnetic showers detected in a 1.6m radius liquid argon calorimeter.

Significant K°, Λ and $\overline{\Lambda}$ signals have been observed in these events. Fragmentation properties of charged particles and neutral strange particles produced in association with high p_T away-side jets have been presented here. The evidence for the softening of fragmentation functions with increasing mass has been given. Also, the ratios of neutral kaon to charged particles as well as strange baryons to strange mesons have been measured in away-side jets. These results have been compared with Feynman-Field model predictions.

⋆ Fermi National Accelerator Laboratory

Publications

1. G. Alverson *et al.*, "Production of Direct-Photons and Neutral Mesons at Large Transverse Momenta by π^- and p Beams at 500 GeV/c", (submitted to Physical Review D).

2. James M. Dunlea *et al.*, "LARGE P_T PRODUCTION OF DIRECT PHOTONS AND π^0 MESONS AT 500 GEV/C", in *Proceedings of the DPF92 Meeting, Fermilab, Nov 1992* (submitted for publication).

3. Dhammika D. S. Weeasundara *et al.*, "PRODUCTION OF JETS RECOILING FROM LARGE P_T π^0 MESONS AND DIRECT PHOTONS IN 500 GeV/c HADRON-NUCLEON COLLISIONS", in *Proceedings of the DPF92 Meeting, Fermilab, Nov 1992* (submitted for publication).

4. David S. Brown *et al.*, "A STUDY OF π^0+jet AND γ+jet EVENTS PRODUCED IN 500 GeV HADRON-NUCLEON COLLISIONS", in *Proceedings of the DPF92 Meeting, Fermilab, Nov 1992* (submitted for publication).

5. M. Zieliński *et al.*, "Large P_T Production of Direct Photons and π^0 Mesons at 500 GeV/c", in *Proceedings of the XXVI International Conference on High Energy Physics, Dallas, Aug 6-12, 1992*, (submitted for publication).

6. G. K. Fanourakis *et al.*, "Direct Photon Physics Results From Fermilab E706" in *Proceedings of the XXVIIth Rencontres de Moriond, Les Arcs, Savoie, France, March 1992*, (submitted for publication by Editions Frontières)

7. G. Alverson *et al.*, "Production of π^0 Mesons at High-P_T in π^-Be and pBe Collisions at 500 GeV/c", Phys. Rev. D45, R3899 (1992).

8. G. Alverson *et al.*, "Direct Photon Production at High-P_T in π^-Be and pBe Collisions at 500 GeV/c", Phys. Rev. Lett. 68, 2584 (1992).

9. G. Alverson *et al.*, "Direct Photon Production at High-P_T in π^-Be and pBe Collisions at 500 GeV/c", Fermilab-Pub-91/212.

10. G. Alverson *et al.*, "Production of π^0 Mesons at High-P_T in π^-Be and pBe Collisions at 500 GeV/c", Fermilab-Pub-91/211.

11. P. F. Slattery *et al.*, "Direct Photons Results from E706", in *Proceedings of the Joint International Lepton-Photon Symposium and Europhysics Conference on High Energy Physics, Geneva, Aug 1991*, (World Scientific, Singapore, 1991), pp. 452-454.

12. J. Dunlea *et al.*, "Production of Jets Recoiling from Direct Photons", in *The Vancouver Meeting - Particles and Fields '91, Vancouver, 18-22 Aug 1991*, edited by David Axen, Douglas Bryman, and Martin Comyn (World Scientific, Singapore, 1992), pp. 681-683.

13. J. Mansour *et al.*, "Inclusive Production of π^0Mesons and Direct Photons at Large Transverse Momentum", in *The Vancouver Meeting - Particles and Fields '91, Vancouver, 18-22 Aug 1991*, edited by David Axen, Douglas Bryman, and Martin Comyn (World Scientific, Singapore, 1992), pp. 678-680.

14. C. Bromberg *et al.*, "Design and Operation of Large Straw-Tube Drift Chamber Planes", *Nucl. Instr. and Meth.* **A307** (1991), 292.

15. K. Hartman *et al.*, "Hadronic Production of Direct Photons at Large Transverse Momentum" in *Proceedings of the XXVIth Rencontres de Moriond, Les Arcs, Savoie, France, March 17-23 1991*, (Editions Frontières) pp. 107-112.

16. E. Engels *et al.*, "Direct Photon Production in Hadron-Hadron Collisions at 530 GeV", in *Proceedings of the XXV International Conference on High Energy Physics, Singapore, Aug 2-8, 1990*, edited by K. K. Phua and Y. Yamaguchi (Southeast Asia Theoretical Physics Association and the Physical Society of Japan), pp. 1439-1441.

17. P. Gutierrez *et al.*, "Inclusive Production of π^0, η and Direct Photons at Large P_T" in *Proceedings of the XXVth Rencontres de Moriond, Les Arcs, Savoie, France, March 11-17 1990*, (Editions Frontières), p. 265.

18. S. Mani *et al.*, "Event Structure and Cross Sections for Single Photon Production at 530 GeV/c" in *Proceedings of the Rice Meeting, Houston, Texas, 3-6 Jan 1990*, edited by Billy Bonner and Hannu Miettinen (World Scientific, Singapore, 1990), pp. 564-568.

19. E. Engels Jr., *et al.*, "Performance Characteristics and Radiation Damage Results from the Fermilab E706 Silicon Microstrip Detector System", *Nucl. Instr. and Meth.* **A279** (1989), 272.

20. G. Ginther *et al.*, "Preliminary Results from Fermilab Experiment E706 A Study of Direct Photon Production in Hadronic Interactions" in *Proceedings of the XXIVth Rencontres de Moriond - New Results in Hadronic Interactions, Les Arcs, Savoie, France, March 12-18 1989*, edited by J. Tran Thanh Van, (Editions Frontières) pp. 181-186.

21. C. Johnstone *et al.*, "A-Dependence of Leading Particle Production by 800 GeV Protons" in *Proceedings of the DPF meeting, Storrs, Aug 15-18 1988*, World Scientific, pp. 666-668.

22. P. Lukens *et al.*, "Preliminary Results from Fermilab Experiment E-706 - A Study of Direct Photon Production in Hadronic Collisions" in *Proceedings of the DPF meeting, Storrs, Aug 15-18 1988*, World Scientific, pp. 683-684.

23. G. Alverson, *et al.*, "Preliminary Results from Fermilab Experiment E-706 - A Study of Direct Photon Production in Hadronic Collisions", in *XXIVth International Conference on High Energy Physics*, R. Kotthaus and J.H. Kühn, eds., (1988), p. 719.

24. W. F. Baker *et al.*, "A-Dependence of Leading Particle Production by 800 GeV Protons", *ibid.*, p. 1400.

25. G. Ginther *et al.*, "Current Status of Fermilab E-706 A Direct Photon Study" in *New Data and Theoretical Trends - Proceedings of the XIXth International Symposium on Multiparticle Dynamics 1988, Arles, France, June 13-17 1988*, edited by D. Schiff and J. Tran Thanh Van, (Editions Frontières) pp. 217-222.

26. G.K. Fanourakis, *et al.*, "Direct Photon Studies: Current Status of Experiment E706 (Fermilab)", *Proc. of the Advanced Research Workshop on QCD Hard Hadronic Processes*, St. Croix, Oct 8-13, 1987, pp. 291-302, edited by B. Cox, NATO ASI Series, Series B, Physics Vol 197

27. E. Engels Jr., *et al.*, "A Silicon Microstrip Vertex Detector for Direct Photon Physics", *Nucl. Instr. and Meth.* **A253** (1987), 523.

28. P. Gutierrez, *et al.*, "E706 Liquid Argon Calorimeter", *Proc. of the International Europhysics Conf. on High Energy Physics*, Bari, L. Nitti and G. Preparata, eds., (1986).

29. F. Lobkowicz, *et al.*, "A Large Liquid Argon Photon/Hadron Calorimeter at FNAL", *Nucl. Instr. and Meth.* **A235** (1985), 332.

30. G. Alverson, *et al.*, "Investigation of Direct Photon Production at Fermilab", *Proc. of the 18th International Conference on Cosmic Rays*, P.V. Ramana Murthy, ed., (1983).

Table of Contents

FIGURE CAPTIONS

TABLE CAPTIONS

1. INTRODUCTION

1.1 Physics Motivation

Recently, a tremendous amount of interest has been generated in strange particle production in very high energy interactions[1]. Strange particles, because of their production characteristics provide an important tool for the study of color confinement mechanisms in the processes of hadronization. Since the center-of-mass energy of a high energy reaction is typically much larger than strange-hadron masses and therefore not constrained by the phase space limitations, the production rates of these particles will improve the understanding of dynamical behaviour of the strong interaction. Further, a study of strange resonance production is of great importance in order to understand multihadron production dynamics from the point of view of a fundamental interaction occurring in the constituent quark system. By investigating the production of strange particles like kaons and lambdas, one can study both the strange quark and baryon production mechanisms in the fragmentation of quarks to hadrons. Also the study of ratio of strange quark production to light quark production, s/u, would give the additional information on the strangeness suppression.

Knowledge on the interaction of the colored partons is always extracted from the observed jets of colorless hadrons since jets are generally regarded as a manifestation of pointlike constituents or partons. A good understanding of fragmentation is therefore mandatory to extract dynamical features of parton processes. Since strange particles can be easily identified, they can be used as strangeness tag to study the process of quark hadronization into jets. It is the purpose of this work to explore the fragmentation processes through studying

the production of these strange particles like K°_{s}, Λ and $\overline{\Lambda}$ in high transverse momentum jets produced in high energy reactions.

1.2 Quarks and Gluons

During the last thirty years, a new framework to understand the strong interactions physics has emerged. The main key to the new understanding is the representation of all hadrons as composites of basic fermions called quarks (q) and antiquarks($\bar{q}$), with Quantum Chromodynamics (QCD) as the non-abelian gauge field theory describing the strong interaction between q's and $\bar{q}$'s, the gluons being the quanta of the QCD gauge fields analogous to Quantum Electrodynamics (QED) where fermions with electrical charge couple to massless photons. The generic name of partons is commonly used for gluons and all types of (anti)quarks. All basic fermions undergo with various couplings the electroweak interactions, described by another non-abelian gauge field theory called Electroweak Theory (EWT) with the photons and the recently discovered weak bosons W^{+}, W^{-} and Z° as quanta of the gauge fields. The description of matter in terms of quarks and leptons, QCD and EWT with their gauge field quanta, is usually called the Standard Model of particle physics[2].

There are at present three families of quarks and leptons thought to exist in nature. It is well understood by now that stable matter consists of electrons and the up and down quarks. The heavy quarks s, c, b and t and the leptons μ and τ are unstable and can be formed at machine energies or in cosmic ray interactions. The characteristics of these particles together with their unstable relatives are given in table 1.

	First family	Second family	Third family
Quarks	u_r d_r	c_r s_r	t_r b_r
	u_g d_g	c_g s_g	t_g b_r
	u_b d_b	c_b s_b	t_b b_b
electric charge	$+2/3$ $-1/3$	$+2/3$ $-1/3$	$+2/3$ $-1/3$
Leptons	e ν_e	μ ν_μ	τ ν_τ
electric charge	-1 0	-1 0	-1 0

Table 1 – The three families of quarks and leptons.

Quarks come with an additional quantum number called color. There are three possible colors, red, green and blue. This color may be considered as a strong charge which has six signs, analogous to the two signs of charge in the electromagnetic interaction, QED. The extraordinary thing about quarks and gluons is that they are never seen as free particles. Whenever attempts are made to dislodge quarks from a proton (or neutron) or to *ionize* the quark and antiquark which contribute the structure of mesons, then a *stream* or *jet* of particles (mesons, baryons, leptons, photons) emerges along the expected flight path of quark or antiquark. The quark itself neither appears as an isolated identifiable particle, nor even as a minority member of the jet of particles; it remains confined by the potential which binds it into the proton. This property, called "confinement" implies that all observable particles with strong interactions, i.e., all hadrons and nuclei, have zero color charges. They must be "colorless" composites of the basic color-charge carriers. Indeed, all known hadrons are composites of this type: qqq for baryons, $\bar{q}\bar{q}\bar{q}$ for antibaryons and $q\bar{q}$ for mesons.

While they are confined inside hadrons, the color force between the quarks

is relatively small, say 20 times stronger than the electromagnetic force, and the quarks enjoy a relatively free existence. If one attempts to remove a quark from a hadron, the color force gets stronger as the quark is pulled away. At short distance, $\leq 10^{-15}$ m, the color force increases with separation. The QCD coupling constant α_s has a Q^2 dependence, which, to lowest order corrections to the gluon propagator has the form[3]

$$\alpha_s(Q^2) = \frac{12\pi}{(33-2f)\,ln\,Q^2/\Lambda^2} \tag{4}$$

where Q^2 is the square of an appropriate momentum transfer (of order p_T^2) that characterizes the hardness of the parton-parton interaction, f is the number of quark flavors that can contribute to the scattering, and Λ sets the scale for Q^2. The above expression is valid only for $Q^2 >> \Lambda^2$ [and $ln\,Q^2 >> ln(ln\,Q^2)$], i.e., when $\alpha_s << 1$. It is clear from equation (4) that if the number of flavors is less than 17 (at SPS/Fermilab energies f = 4), then $\alpha_s \rightarrow 0$ as $Q^2 \rightarrow \infty$. As the separation increases, the energy stored in the color field becomes sufficiently large to produce a quark-antiquark pair out of the vacuum. The struck quark is said to fragment into a jet of hadrons. Feynman scaling[4] predicts that the hadrons share the energy of the quark in a way which is energy independent. This is written as

$$\frac{1}{N_{jet}}\frac{dn}{dz} = D(z) \tag{5}$$

where $n(z)$ is the number of hadrons with momentum between z and $z + dz$, $z = P_h/P_q$ (i.e. the fraction of the quark momentum carried by any hadron) and N_{jet} is the total number of hadrons in the jet.

1.3 JETS

The large transverse momentum collisions are those very rare high energy collisions of hadrons which produce particles with transverse momenta (p_T), much larger than 1 GeV/c. The first observation of the departure of the single-particle transverse momentum distribution from the thermodynamical distribution [$Ed^3\sigma/dp^3 \sim e^{-bt}$], was reported in 1972 at the CERN Interacting Storage Rings (ISR)[5]. It was found that the spectrum of large transverse momentum of secondaries produced in hadronic collisions did not exhibit strong damping as observed from its behavior at low p_T values.

This historical result suggested that the large-p_T particle production took place through an interaction between point-like elementary constituents of the proton (similar to the Rutherford scattering) that could not be of an electromagnetic nature as formerly proposed by Berman *et al.*[6], but the large value of the ISR cross-section suggested that this interaction was mediated by the strong force. It is now widely believed that the production of objects with a large transverse momentum in collisions of two hadrons is due to the hard scattering of their constituents.

The parton model[7] constituted a first fruitful framework for interpreting the large-p_T phenomena: the wave function of the colliding hadrons is the sum of subfields -the partons- weakly interacting with each other. At high-p_T, the reaction occurs through hard binary collisions of artons, with a subsequent fragmentation of the both the struck (active) par s and those not directly involved in the hard collisions (spectators). As th r of the struck parton increases in any collision, it becomes easier to resolv the particles from the

fragmenting spectator partons. This is shown in the Fig. 1.

The cluster of particles coming from parton fragmentation , as interpreted by QCD, are called Jets. Jets are now a well established phenomena in hadron collisions. As the manifestation of a scattered parton they allow one to study the basic strong interaction process of parton-parton scattering. When two partons collide, the collision means occurring between a pair of gluons or a pair of quarks or between a pair of gluon and a quark.

According to fig. 1, two scattered constituents with large momentum show up as two jets of hadrons. One of them which is used to trigger the experiment is called a Trigger Jet and the other one on the opposite side is called Away-side Jet. Two incoming hadrons, each with one constituent removed by the hard scattering are expected to create two spectator jets or known as Beam jet, along the beam direction and Target Jet, along the target particles direction.

1.4 Jet Cross-Section

The use of perturbation theory in QCD calculations is made possible by the feature of asymptotic freedom. This term is used to describe the weakening of the effective quark-gluon coupling at short distances or, equivalently large momentum transfers.

The prescription provided by the parton model has met with much success in describing a variety of large momentum transfers processes. Since the interaction time of the hard scattering is much less than the time scale of the initial-state weak interaction among partons and of the final-state hadronization (impulse approximation) one can assume to factorize the process into two parts

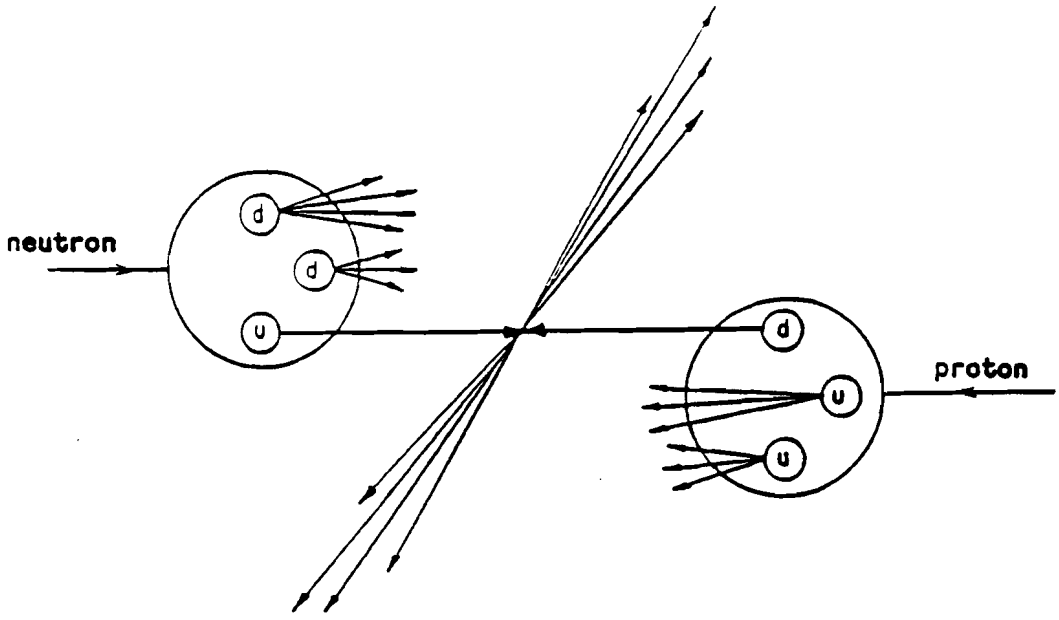

Figure 1 – Quark-quark scattering diagram in which the quarks have received a large transverse momentum, p_T. The jets of particles produced in the fragmentation of the struck quarks and the spectator quarks are indicated.

by utilizing the impulse approximation. The probability of finding a parton a(b) in a hadron A(B) with a momentum fraction lying between x and $x + dx$ is denoted by the distribution function $G_{a/A}(x)\,(G_{b/B}(x))$. The probability of obtaining a hadron C with a momentum fraction between z and $z + dz$ from a parton c is denoted by the fragmentation function $D_{C/c}(z)$. These functions cannot be calculated using perturbation theory and must therefore be obtained from data for various types of hard scattering processes. The cross-section for the process under consideration is then built up by an incoherent summation over all possible constituent scatterings, each of which is weighed by the appropriate parton distribution and fragmentation functions. In the parton model the hard scattering is described by the lowest order subprocesses which, for high-p_T particle, jet, or photon production , correspond to two-body scattering. This is shown schematically in Fig. 2. The corresponding expression for the invariant cross section is

$$E_C \frac{d\sigma}{d^3P_C}(AB \to C + X) = \sum_{abcd} \int dx_a\, dx_b\, dz_c\, G_{a/A}(x_a) G_{b/B}(x_b) D_{C/c}(z_c) \frac{\hat{s}}{z_c^2 \pi} \frac{d\sigma}{d\hat{t}}(ab \to cd)\, \delta(\hat{s} + \hat{t} + \hat{u}). \tag{6}$$

The delta function appearing in Eq.(6) is that which is appropriate for the two-body scattering of massless partons and follows simply from two-body phase space. Furthermore, the initial and final partons have been assumed to be collinear with the corresponding initial and final hadrons, i.e. no parton transverse momentum (k_T) smearing has been included. In the above equation s, t, u

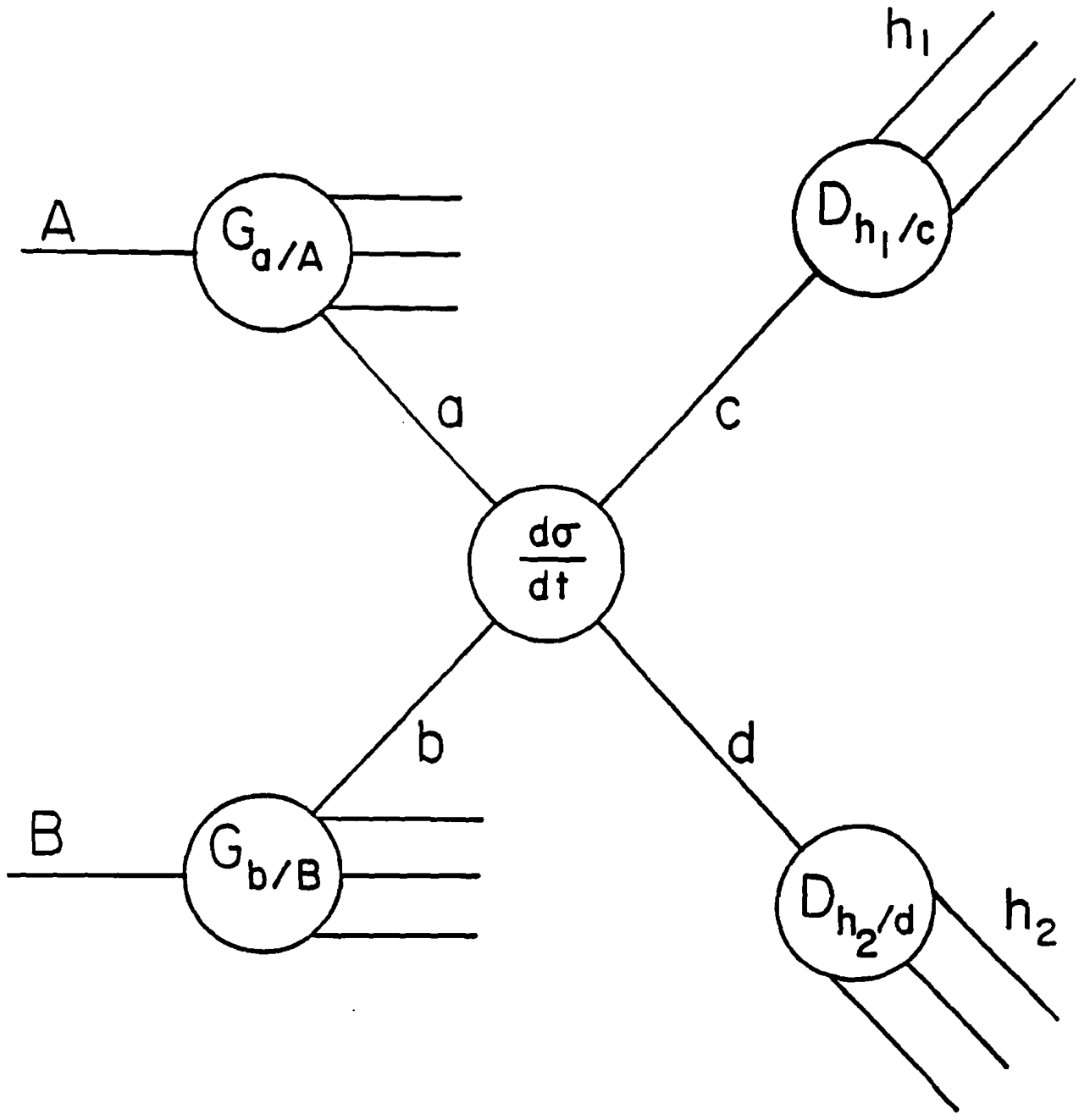

Figure 2 – A schematic representation of a two-body hard scattering process.

are the mandelstam variables for the hadrons as defined below

$$s = (P_A + P_B)^2 \tag{7a}$$

$$t = (P_A - P_C)^2 \tag{7b}$$

$$u = (P_B - P_C)^2 \tag{7c}$$

A similar set of variables $\hat{s}$, $\hat{t}$, $\hat{u}$ exist for the constituents scattering subprocess (hard subprocess). For the case of massless two body scattering, they satisfy the constraint $\hat{s} + \hat{t} + \hat{u} = 0$. The $d\sigma/d\hat{t}$ is the elementary cross section for the interaction between a and b. For the jet cross section the four vectors of the interacting partons are defined as follows[8]:

Let parton a carry a fraction x_a of hadron A's longitudinal momentum and similarly for parton b let the fractional longitudinal momentum be x_b. The four-vectors for a and b in the overall hadron-hadron center-of-mass system assuming massless partons and neglecting any parton transverse moment can be written as

$$p_a = \frac{x_a \sqrt{s}}{2}(1,0,0,1) \tag{8a}$$

$$p_b = \frac{x_b \sqrt{s}}{2}(1,0,0,-1) \tag{8b}$$

where the positive z axis is taken to be along the direction of the incident hadron A. If the scattered parton c has transverse momentum, p_T and rapidity y_1, then

its four-vector is

$$p_c = \mathrm{p}_T(coshy_1, 1, 0, sinhy_1) \tag{9}$$

and similarly for parton d with rapidity y_2, its four-vector is

$$p_d = \mathrm{p}_T(coshy_2, 1, 0, sinhy_2) \tag{10}$$

In the approximation that parton-k_T effects can be neglected, the dijet cross section in terms of rapidities of the two jets and the transverse momentum, p_T, (possessed by each) can be written as

$$\frac{d\sigma}{dy_1 dy_2 d\mathrm{p}_T{}^2}(AB \to jet_1 + jet_2 + X) = \sum_{ab} x_a G_{a/A}(x_a) x_b G_{b/B}(x_b) \frac{d\sigma}{d\hat{t}}(ab \to 12). \tag{11}$$

where

$$x_a = \frac{\mathrm{p}_T}{\sqrt{s}}(e^{y_1} + e^{y_2}) \tag{12a}$$

and

$$x_b = \frac{\mathrm{p}_T}{\sqrt{s}}(e^{-y_1} + e^{-y_2}) \tag{12b}$$

1.5 Production of Strange Particles in High-P_T Jets

The mechanism of color confinement is one of the big open questions in particle physics and has attracted considerable attention. The study of hadronization in general, and of strange particle production particularly in jets provide one of the handles towards a deeper understanding of the strong forces responsible for confinement[9]:

- It is presently believed that the confining potential between a quark and an antiquark rises linearly with distance, i.e. the force field can be pictured as a basically one-dimensional field, a *color flux tube* or *string*. In such a model[10], confinement arises since once the primary quarks are separated by a certain distance (of the order of one fermi), it is energetically favorable to form a new quark-antiquark pair which screens the color field. In such a process, the rate of strange quark production as compared to production rates for light up or down quarks depends on the energy density in the color field. The ratio of strange to up or down quark rates provides therefore a measurement of this energy density, the *string constant*, or in other words of the typical scales of space, time and momentum transfer involved in confinement processes. In these string models, the particle composition is described by a number of parameters that are put in by hand, such as strange quark suppression factor, s/u, and the frequencies with which different parton flavors are produced in a string decay. The strange suppression factor enters directly in independent fragmentation models also and it is determined from experimental data.

- In general, strange particles, because of their larger masses, make a more reliable probe of the fragmentation process. Most of the final state hadrons stem from resonance decays. Since in a typical pion producing decay such as $\rho \rightarrow \pi\pi$ the Q-value of the decay is larger than the pion mass, the momentum of the final-state pion is a very poor estimator of its parent's momentum. Strange particles, however, are more likely to be a direct product of the fragmentation process because there are few resonances decaying into pairs of strange particles.

- An important question in hadronization is short range order from $q\bar{q}$ pair production. Studying this from non-strange mesons is hampered by the $q\bar{q}$ combinatorial background. In a typical high-energy reaction, 10 or more pions are produced in the hadronization process, but typically one or two pairs of strange particles. Because of this lower combinatorial background for $s\bar{s}$ pairs, flagging these pairs can throw light on their creation process[11]. The position in phase-space of a strange hadron with respect to its associated anti-strange partner provides clues to the momentum transfer in the confinement process. In this context, again, it is helpful that there are few resonances decaying into pairs of strange particles. Using their good strangeness identification detector, TPC[12] collaboration observed significant short range K^+K^- correlations in y which was well reproduced by the Lund model.

- Whereas meson production appears quite natural in most models of the confinement mechanism, the mechanisms responsible for baryon production are by no means obvious. The suppression factor for baryon production over meson production is also introduced as a parameter in most models. As before, the clean signature from a strange quark can be a useful tool for studying fragmentation of partons into strange baryons. Finally, strange baryons enable us to study polarization effects in the hadronization process. In particular, the lambda baryon polarization is easy to measure and provides a direct measurement of the polarization of the s-quark. String models, for example, do predict a significant polarization of secondary quarks produced in the color field[13].

Before entering into the details of strangeness component estimation, we need to discuss the measurements of the signal itself. Strangeness production is normally very small so that only a few percent of strange and antistrange quarks are produced in hadronic interactions due partly to the higher mass of the strange quark and the difficulty of concentrating enough energy to produce $s\bar{s}$ pairs in hadronic interactions. The normal convenient particles for observation are the short lived kaons (K_s^o), the lambdas (Λ) and the anti-lambdas ($\overline{\Lambda}$). While the measurement of a Λ particle gives evidence of the presence of a strange quark and that of a $\overline{\Lambda}$ an anti-strange quark, the observation of a K_s^o only shows (because its observation is by means of a weak decay not conserving strangeness) that there was either a strange or an anti-strange quark present.

1.6 Previous Experiments

The subject of measuring the correlations between high-p_T trigger (e.g., direct photon, π^o, η, etc.) and their associated jets of hadronic particles, with strange particle production in general, has attracted considerable attention so far. It becomes of great interest if it can be employed for flavour tagging of parton jets and hence to study QCD predictions in detail. In addition, production of large transverse momentum hadronic jets containing strange particles can be used as a tool to study the structure functions for valence quarks (in K mesons) as well as sea quarks of hadrons (in π and K mesons and protons)[14]. Here some results from previous experiments are presented.

Fragmentation studies First, consider the correlations between the trigger and hadrons which are on the same side of the events, i.e. which have an azimuthal

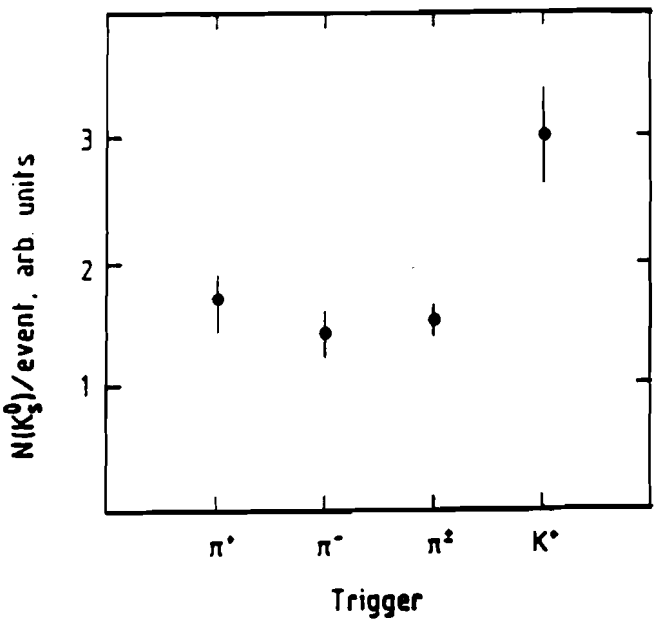

Figure 3 – Average number of reconstructed K_s^0 with $Z_f > 0.2$ per event for different triggers (ref 15).

angle ϕ within ± 90 degrees of the trigger. With the reconstruction of strange particles one can measure the strangeness production in the toward jets. This was done, for example, by an ISR experiment using Split Field Magnet Detector. In Fig. 3 , the average number of K_s^0 per event with $Z_f > 0.2$ (where $Z_f = \frac{P_\parallel}{P_{trigger}}$, $P_\parallel$ denotes the momentum component along the jet axis) is shown for pion and K^+ triggers[15]. For K^+ triggers, the observed rate of K_s^0 is about a factor of 2 larger than for pion triggers. Also, for K^- triggers with $p_T > 3$ GeV/c an increase of the K_s^0 flux in the toward jet by a factor of 2.3 ± 0.3 was observed[16] relative to pion triggers. Again, this provides evidence that K triggers come mostly from a flavour neutral parent parton such that strangeness is conserved locally in the trigger jet.

For the correlations among the trigger and the away-side particles, neither the away jet axis nor its parton flavour are constrained by the triggering particle. If these away side hadrons have sufficiently large p_T, they can be interpreted as having resulted from the recoiling partons. Hence in principle, one can even study inclusive jet fragmentation. For hadronic large-p_T collisions the variable $X_E(= p_T/p_{trigger})$ is a good approximation of z. Fig. 4 shows the dN/dX_E distribution of charged particles for various p_T slices[17]. Since the data points overlap it follows that jet fragments scale in the normalized longitudinal momentum, z, for transverse momenta of a trigger larger than 3 GeV/c. These measurements can be made for strange particles also. Results from experiments on jets in e^+e^- collisions are discussed below.

Studies in e^+e^- Interactions A number of investigations have been carried out in e^+e^- interactions also. In these reactions, the number of primary strange quarks is small compared to the number of strange particles produced because the latter can also result from the decay of heavy quarks (c or b) or from strange quarks produced during the fragmentation process. The study of strange particle production in e^+e^- reactions will reflect the production mechanism in the fragmentation of quarks to hadrons. in which they presented the Differential cross sections for K° production from various experiments (ref 1a) at different energies are shown in figure Fig. 5. The TASSO collaboration also investigated the strange meson production properties in jets by studying the rapidity and p_T^2 distributions as well as the evolution of the multiplicities as a function of event sphericity and found no evidence for increase in strange meson yields with increasing sphericity faster than the total charged multiplicity.

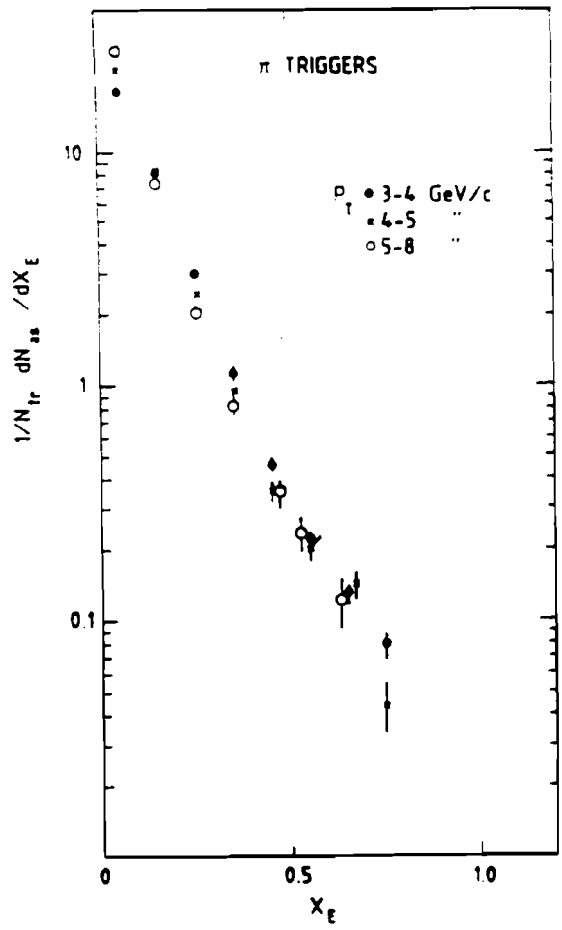

Figure 4 – Number of tracks per event in the away side jet as a function of X_E for pion trigger (ref 17).

Another study by HRS Collaboration (Ref 1a) in e^+e^- interactions presents comparison of K° and charged particle distributions in a study of the hadronization of quarks of known flavor. By tagging events, they were able to identify hadronic showers coming from quarks of known longitudinal momentum and flavor. For the lower momentum quark they found that the fractional energy spectrum scaled with the momentum of the quark in a simple way. Also for the high momentum quarks, they found no indication for the data flavor dependence of the ratio, R(K°/charged particle), as a function of the kinematical variable, z,

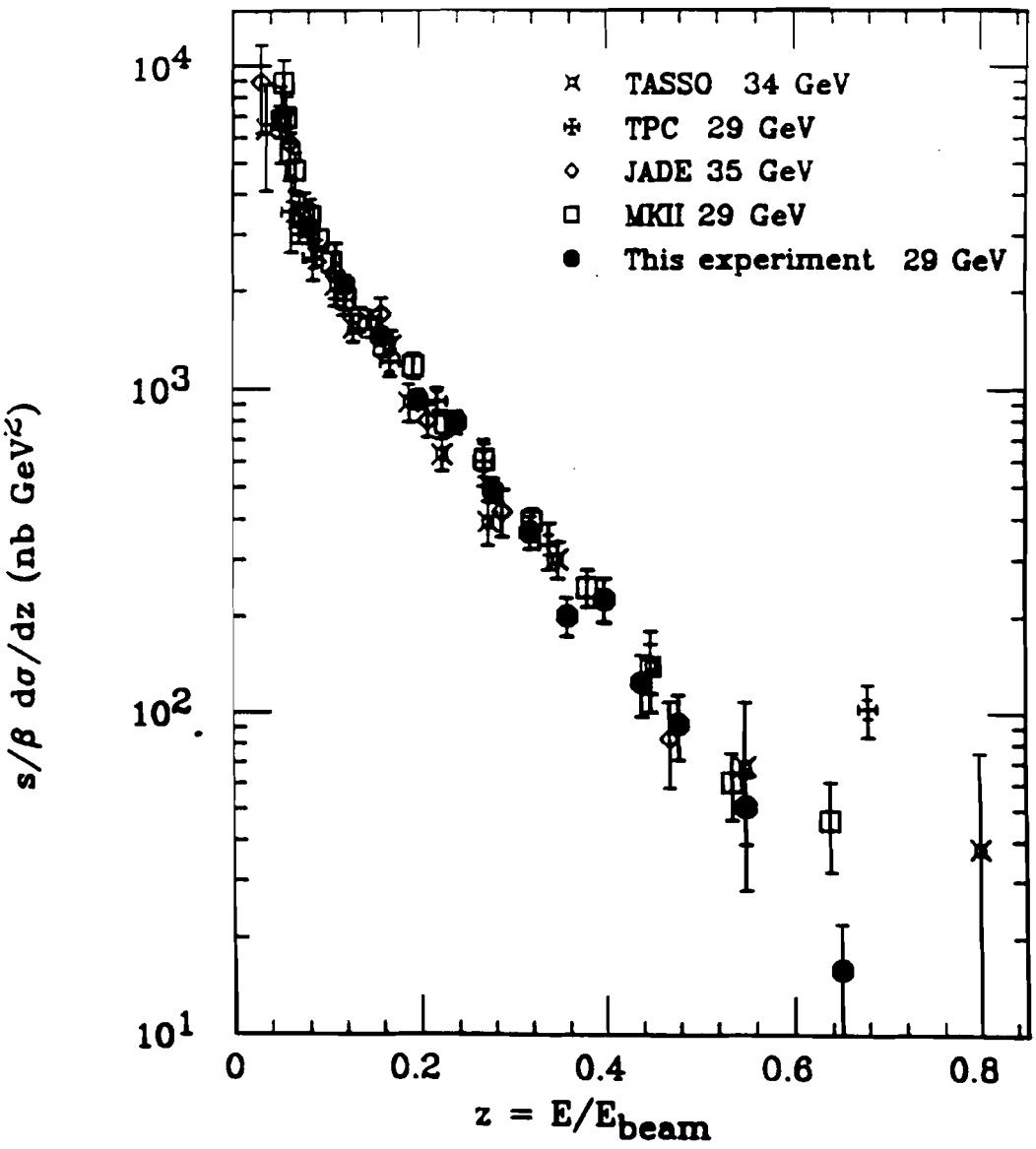

Figure 5 – K° scaling cross sections as a function of fractional energies for various experiments (ref 1a).

the fractional energy, and y, the rapidity. In Fig. 6 , rapidity distribution ratio for the K°'s and the charged particles is shown along with Lund String Model (ref 10) and Webber model[18] predictions as well. Both the model were able to produce the fall off seen in the data above 3.0 but they fail to agree at small $|y|$.

Tasso group[19] suggested enhancement of strange particle production in

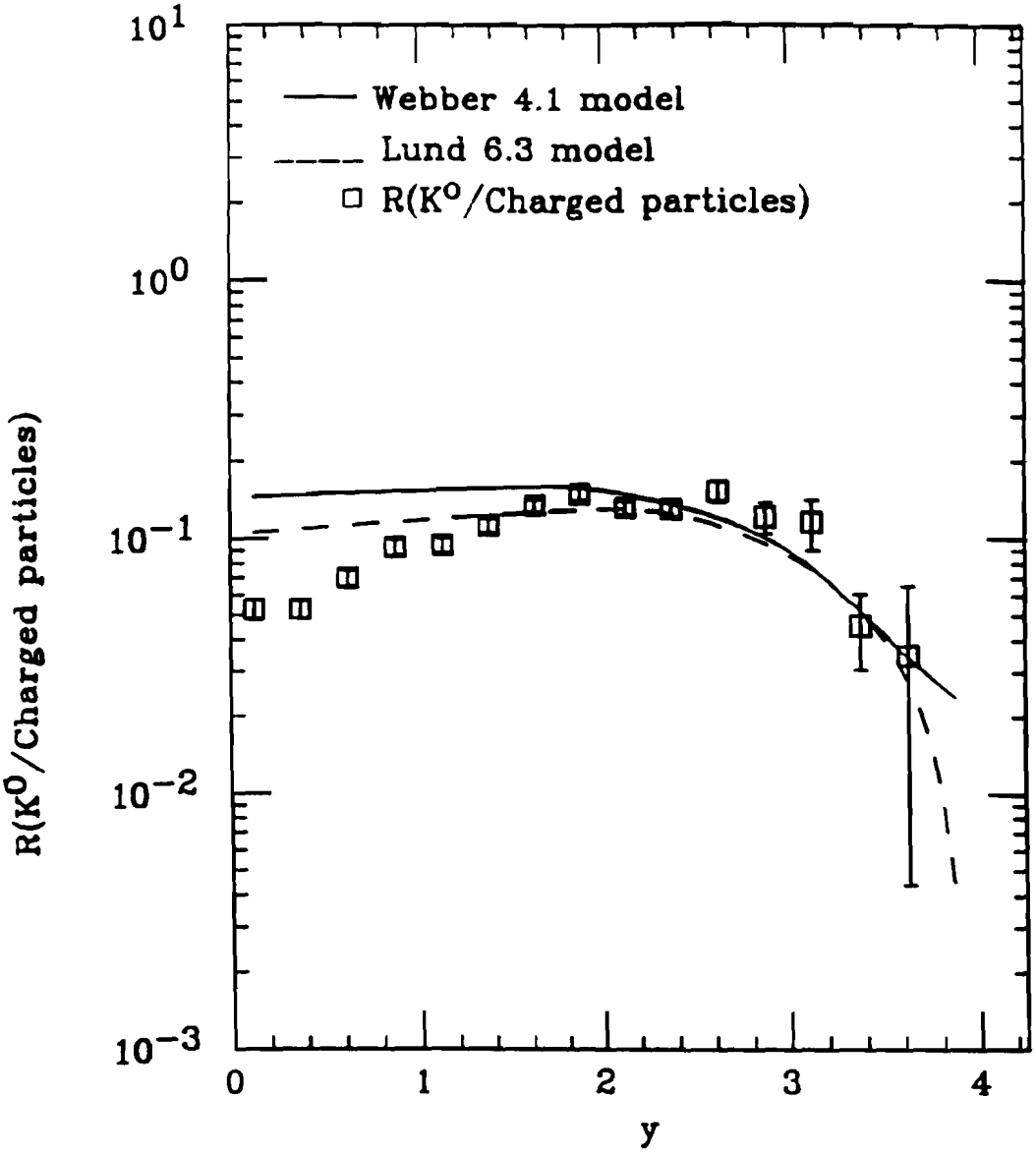

Figure 6 – Rapidity Distributions ratio for K°'s and charged particles with the Lund model (dashed) and the Webber model (solid) model predictions (ref 18).

gluon enriched samples. However, there are no definite tests till now for the strange particle enhancement or the flavor blindness of gluon.

Structure functions Since quarks and antiquarks from the *sea* are in many respects equivalent to gluons, they can also contribute to hadronization process. They are neutral on average, have much lower momenta than valence quarks,

and their fragments may carry any energetically allowed flavour. Sea quarks come in pairs. When a s-quark from the sea is scattered it turns up in one of the fragments of a transverse jet whereas its antiquark is contained in a fragment of a spectator jet. Contrary to that when an $s\bar{s}$ pair is created in the fragmentation of a scattered parton both will appear in the same transverse jet.

The reason why scattering of sea (anti-)quarks does not contribute strongly to the yields of large p_T particles is their low average longitudinal momentum, i.e. their soft structure functions. Therefore they cannot attain a significant transverse momentum when scattered off other partons. Nevertheless, there is one experimental observation indicating that at lower values of p_T strange sea quarks do play a role. If a $\bar{s}$-quark is scattered the associated s-quark remains in one spectator jet. There it may form a lambda hyperon. Fig. 7 shows the yields of a lambda hyperon produced along the direction of an incoming proton for proton-proton collisions with a trigger particle with $p_T > 1.15$ GeV/c at $\theta = 90$ degree[20]. The yield of lambda is much larger for events associated with K^+ triggers than for those which were selected by triggering on protons or pions.

1.7 Scope of the Thesis

The process of investigation of strange particle production in high energy interactions has been going on for a long time although most of the time emphasis was laid on cross-sections obtained for these particles at various energies and with different types of reactions[21]. Although several studies have been made in hadron-hadron interactions, this thesis can open grounds for new studies in this field. Firstly, a study of strange particles in away-side jets recoiling against a high p_T direct photon and diphoton triggers has not been done so far. Although

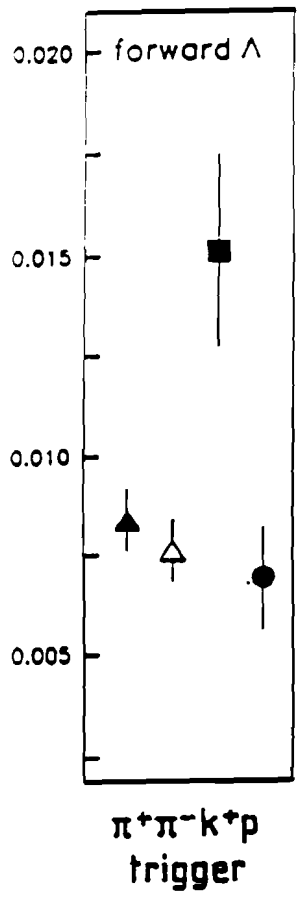

Figure 7 – Number of forward Λ per large p_T trigger particle at $\theta_T = 90°$ with 1.15 GeV/c $< p_T <$ 2.25 GeV/c (ref 20).

this work is limited to studying strange particle production in association with high p_T π^o's, it represents the necessary first step towards studying strange particles accompanying direct photons. Secondly, this is a study at the highest available beam energies in fixed target experiments. Also, the results presented here are based on the highest statistics of strange particles ever presented so far in high p_T hadron-hadron interactions. Although, no comparison on total cross-sections for K^o, Λ and $\overline{\Lambda}$ production is presented here (the data sample used here is trigger biased), various ratios have been studied that can shed some

light on this subject.

As mentioned earlier, the aim of this work is to study the strangeness composition in away side jets recoiling against high p_T triggers. The results presented here can be used along with those obtained in e^+e^- interactions in order to study any possible differences in hadronization that may arise due to the presence of spectator quarks in hadronic interactions.

Some unique features arise in the study of away side jets recoiling against high p_T direct photons. Let's consider the compton process for the production of direct photons. Since the photon couples to electric charge, the expectation for the compton process is that the recoiling quark will predominantly be a u quark. In proton-proton collisions the ratio of u to d quarks on the away-side will be approximately 8, with a factor of 4 coming from the square of the quark charge and a factor of 2 coming from the fact that there are two valence u quarks and one d quark in a proton. This ratio may give rise to an excess of positive over negative leading hadrons on the away-side if, as expected, a u quark yields on the average more positive hadrons than a d quark. This ratio should rise with the variable z. If an s quark participates in the compton process, similar charge ratios can be studied. For example, the ratio of neutral strange particles to negative charged particles can be expected to be constant with z. Now let's consider the annihilation process which becomes important at high p_T in production by π^- beams. Here a gluon recoils against the direct photon and this process can be used to study the contribution of gluon jets to strange particle production.

The organization of this work is done in the following way. The present

chapter gives the motivation and the theoretical background on the subject. In chapter 2, a detailed description of the E706 spectrometer used in this analysis is given. Chapter 3 is devoted to the discussion of the event reconstruction code using charged particle spectrometer, liquid argon calorimeter and the software description including ACP[22] (Advanced Computer Programming). Event selection for this work and the evidence for the strange particles in the data is given in chapter 4. This chapter also includes the Monte Carlo method used to determine the corrections to the data. The last two chapters are devoted to the jets observed in this data. In chapter 5, a further selection criteria for the jets is given. Algorithm for the jet reconstruction and the evidence for the jets in the data is also presented in this chapter. Results and the conclusions for strange particle production in the jets along with Monte Carlo comparison are summarized in chapter 6.

Throughout this work, K° distributions are referred to the summed K° and $\overline{K}^\circ$ distributions. Also the right-hand coordinate system is used here, with Z-direction pointing along the direction of incident beam, X-direction horizontal and Y-direction with the positive axis pointing upwards. While the term upstream points towards the direction of the incoming beam from the target, the term downstream means along the direction of the incident beam. The transverse momentum of any particle is denoted by "p_T".

2. Experimental Setup

This chapter contains a description of the particle spectrometer employed in the experiment. This spectrometer, built at Fermi National Accelerator Laboratory (FNAL), is located at the new Meson West (MW) beam line. Fig. 8 shows the schematic layout of the Meson west Spectrometer. The details of the individual components of the system is discussed in the following sections.

The apparatus consists of a set of a silicon strip detector (SSD) planes in front of and behind the target, an analyzing magnet, a set of multiwire proportional chambers (PWC's), a liquid argon calorimeter (LAC) with both electromagnetic and hadronic sections, and a forward calorimeter. Downstream of the forward calorimeter is a muon system provided by the experiment E672, which utilizes a toroidal magnet in conjunction with PWC's and drift chambers to identify muons. The cerenkov counter which is located in the beamline upstream of the MW hall is not shown in the figure 1.

2.1 The Beam Line

A primary proton beam of 800 GeV/c, with an average intensity of 2×10^{12} protons/spill, is incident on a primary upstream target (0.75 interaction length Al target). This beam line is designed to operate in two modes: the +ve and the -ve charged beam modes. When running with +ve polarity, it transported 530 GeV/c secondary +ve particles, mainly p ($\sim$91.3%), π^+ ($\sim$7.2%) and K^+ ($\sim$1.5%). In the -ve mode, it transported mainly π^-($\sim$97%), K^-($\sim$2.9%) and $\bar{p}$ ($\sim$0.2%)[23].

The production angle for -ve polarity beam were chosen to be 0 mrad and 1.4 mrad for the +ve polarity beam. This non-zero production angle was required for the +ve beam mode to avoid the possibility of transporting the primary beam into the E706 detector. By adjusting the magnetic field and the polarity of the magnets , the beam of desired momentum was directed through the collimators to the MW secondary beam line. The +ve beam had an intensity of upto 7×10^7 particles/spill and the -ve beam had an intensity of upto 4×10^7 particles/spill. The beam spills were separated by 40 sec and were 23 sec long. Within each of these spills, the beam particle came in 2 ns bunches, separated by 19 ns intervals. The momentum spread of the beam is typically less than 6%.

Three large 'spoiler' magnets were positioned in the beam line to deflect the background muon flux. Other major components of the beam line are a cerenkov counter for particle identification, a vertical sweeping magnet for e^- calibration of the calorimeter, a 6 m long, large hadron shield to eliminate beam halo and two veto walls for rejecting muons.

The particles which are produced (mainly decays from π and K) during the transportation of the beam through the beam line tend to form a halo around the beam pipe. Muon contamination in the beam was measured to be 0.4% for the +ve beam and 0.5% for the -ve beam. At the end of the beamline and in the front of the spectrometer, large sheets of steel, $\sim$ 6 inches thick, were placed, layered at an angle to the beam axis to prevent halo particles from passing through gaps between the steel.

To discriminate between π, K and p in the secondary beam, a differential gas cerenkov counter was used. This counter is placed about 100 m upstream of

the detector and is 42.1 m long and has a radius of 24.4 cm. Helium gas in the pressure range of 4 to 7 psia, is used as the radiator. The counter has a 32.3m focal length mirror which focuses light at two rings of scintillator. It has one coincidence and one anti coincidence ring, each containing six phototubes. The cerenkov angle for the coincidence ring was 5 mrad. The cerenkov detector was usually set to trigger on the minority beam particles with an efficiency of 57% for tagging K^- in the -ve beam with a contamination of remnant 3% pions. In the +ve beam , π^+ were tagged with $\sim$ 78% efficiency and contained a remnant 8% contamination from K^+.

The spectrometer was shadowed by two scintillator counter veto walls (VW) which further reduced the contamination of the triggers (explained later in this chapter) by halo muons. The two muon walls are in coincidence so that events that muons in the same region as the trigger from electromagnetic calorimeter can possibly be vetoed by the trigger. Each wall (3 m by 3 m) is made of 32 scintillators counters arranged in such a manner that there is a 10 cm $\times$ 10 cm hole at the center of the beam line.

2.2 Target Selection

The experiment decided to choose various segmented nuclear targets for the investigation of direct photon phenomena , since segmented target appears to be optimum for efficiency of track reconstruction, primary vertex location, and also the use of segmented target makes it easier to distinguish the secondary interactions originating in different target segments as well as decay particle vertices. Also, different materials allow a study of A - dependence of direct photon production.

A low Z (atomic number) material for the target was chosen to reduce the conversion rate of photon into e^+e^- pairs. The overall thickness and the spacing between target segments were determined by the position resolution of the z coordinate of the vertex measured by the SSD system.

The total thickness of the target was chosen to be 10% of a nuclear interaction length. For most of the time, the target consisted of two Cu target 0.08 cm thick and spaced 0.16 cm apart, followed by 20 Be targets 0.2 cm thick segments and separated by 0.16 cm gaps. The gap between Cu target and Be target was 3.2 mm. This whole target assembly was placed after 3 silicon strip modules in front of the rest of SSD system. Table 2 gives the summary of the various types of the targets used in this work.

Target type	Beryllium	Copper
X width (cm)	2.0	2.0
Y width (cm)	12.0	12.0
Number of Segments	20	2
Segment thickness (cm)	0.2	0.08
Gap thickness (cm)	0.16	0.16

Table 2 – Characteristics of the targets used.

2.3 Magnet

To determine the momenta of charged particles, a dipole magnet (referred to as MW9AN), along with the SSD's & PWC's was used. The center of the magnet was located 2 m downstream of the target. This magnet is a vertical

dipole with a maximum field of 15.2 KG. The magnet aperture expands from 35.6 cm × 25.4 cm to 137.2 cm × 124.5 cm over a length of 3.28 m. The magnet imparts a transverse kick of 0.450 GeV/c. The dipole magnet bends the charged tracks in the horizontal plane (X–Z). By measuring the amount of bending, the charge and momentum of the tracks are measured. Two ferro-magnetic mirror plates were installed on the magnets to reduce the fringe field outside the volume of the magnet.

2.4 Silicon Strip Detector

The purpose of Silicon Strip Detector (SSD) together with the PWC's after the analysis magnet is to measure the momenta of charged particles in hadronic jets associated with high transverse momentum photons and π^0. In addition the SSD's serve as a vertex detector which accurately locates the position of primary and secondary interactions in the segmented target.

The SSD system is constructed of 7 X–Y modules or 14 SSD planes with a total of 7120 active strips. All of the SSD's have a 50 μm pitch and a thickness of 250 – 300 μm. The 3 X–Y module upstream (called beam SSD's) and the first X–Y module immediately after the target are $3 \times 3\,cm^2$; the wafers of the last three X–Y modules are $5 \times 5\,cm^2$. The last four SSD's , downstream of the target, because of their function are called vertex SSD's. Fig. 9 shows the SSD/segmented target region. In Table 3 , the active areas of the SSD planes are given[24]. The total number of SSD channels for the readout part is 7200.

The readout system provides digital information on the traversal of strips by minimum ionizing particles with high efficiency and small dead time. A

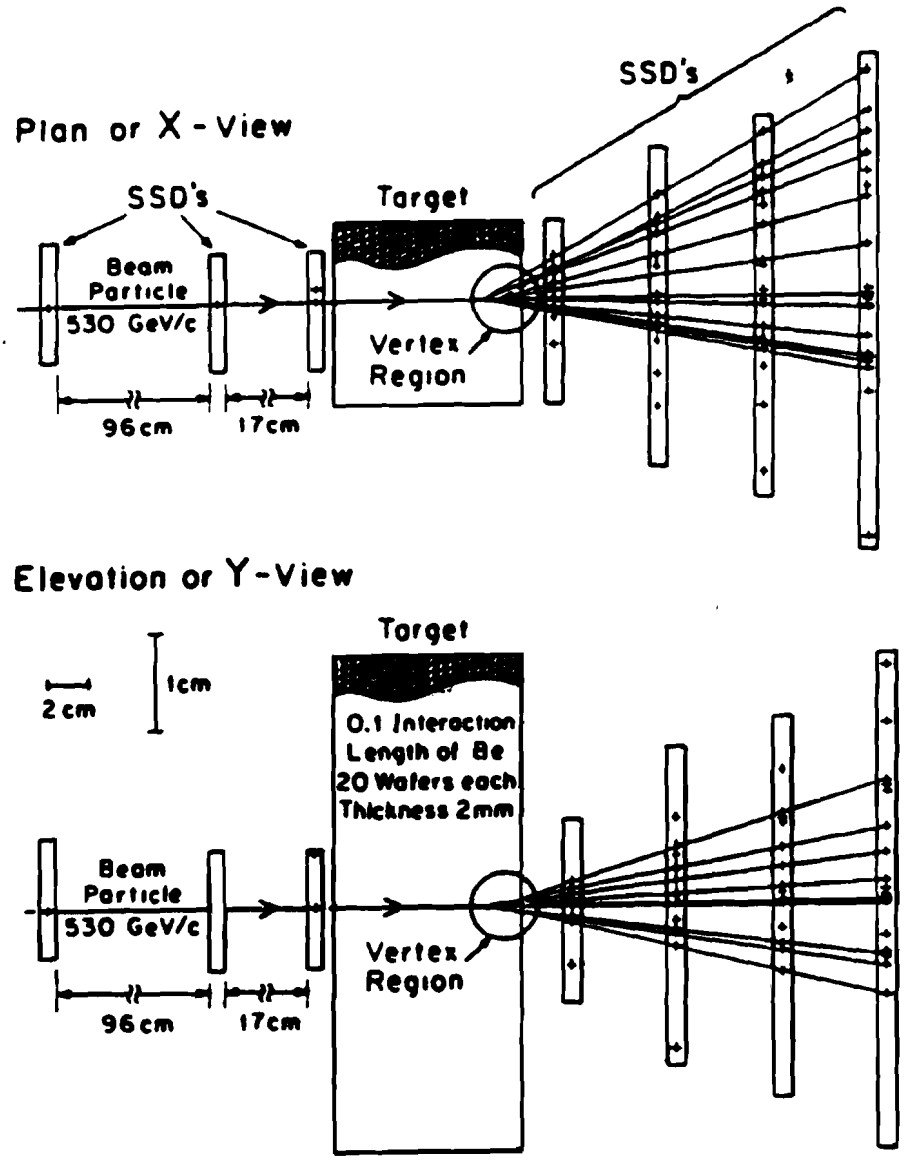

Figure 9 – Schematic of the segmented target/SSD system with a multivertex event superimposed on the planes.

SSD plane	X width (cm)	Y width (cm)	Z thickness (cm)	Z location (cm)
1	1.5	1.5	0.15	-132.51
2	1.5	1.5	0.15	-132.52
3	1.5	1.5	0.15	-36.4
4	1.5	1.5	0.15	-36.4
5	1.5	1.5	0.15	-18.9
6	1.5	1.5	0.15	-18.9
7	1.5	1.5	0.15	-1.8
8	1.5	1.5	0.15	-1.8
9	2.5	2.5	0.15	4.5
10	2.5	2.5	0.15	4.5
11	2.5	2.5	0.15	9.25
12	2.5	2.5	0.15	9.25
13	2.5	2.5	0.15	14.7
14	2.5	2.5	0.15	14.7

Table 3 – Properties of the SSD's.

minimum ionizing particle traversing one of the detector produces $(2.0-2.4)\times10^4$ electron-hole pairs, depending on the thickness of the wafer, and the charge is collected in $\sim$ 20 ns. This charge is then fed into a charge sensitive preamplifiers whose output is further amplified,discriminated, and converted to logic signals for storage as digital data. The data from the electronics is read out by PDP-11 computer and is sent to a micro-vax for concatenation with the data from the other parts of the spectrometer. A detailed description of SSDs can be found elsewhere[25].

2.5 Proportional Wire Chambers

The PWC system, located downstream of the analyzing magnet, consists of 4 modules. Each of the modules has four planes of wires, called "anode wires", labelled as X, Y, U & V view. The wires in an anode plane are equally spaced and the orientations of the wires in each of the four planes are 0° , 90° , 36.87^0 and -53.13^0 w.r.t. vertical (Y) direction in the E706 coordinate system. The chambers alongwith SSD's were designed to run at an interaction rate of 1 MHz. Fig. 10 shows the various planes in a chamber.

The anode or sense wire spacing was 0.254 cm, resulting in angular resolution of 0.03 mr. The sense wire are gold-plated tungsten with a pitch of 0.254 cm. Graphite coated mylar (0.00254 cm thick) were used as the cathodes of all the chambers. This graphite coating allowed the high voltage to be independently set over different segments of the wire so that the regions near the beam could be deadened selectively during high intensity running. The total number of PWC's channels were 13,400.

The readout system for the PWC also relies on the same Nanometric amplifier, discriminator and latching system used for the SSD's. The detailed description of the construction and the principles of the MWPC can be found elsewhere (ref 24).

2.6 Liquid Argon Calorimeter

A Liquid Argon Calorimeter (LAC), 3 m in diameter and 0.75 m long along the beam line , was designed to measure the position and energy of both photons/electrons and hadrons of very high energy and also to trigger on the events

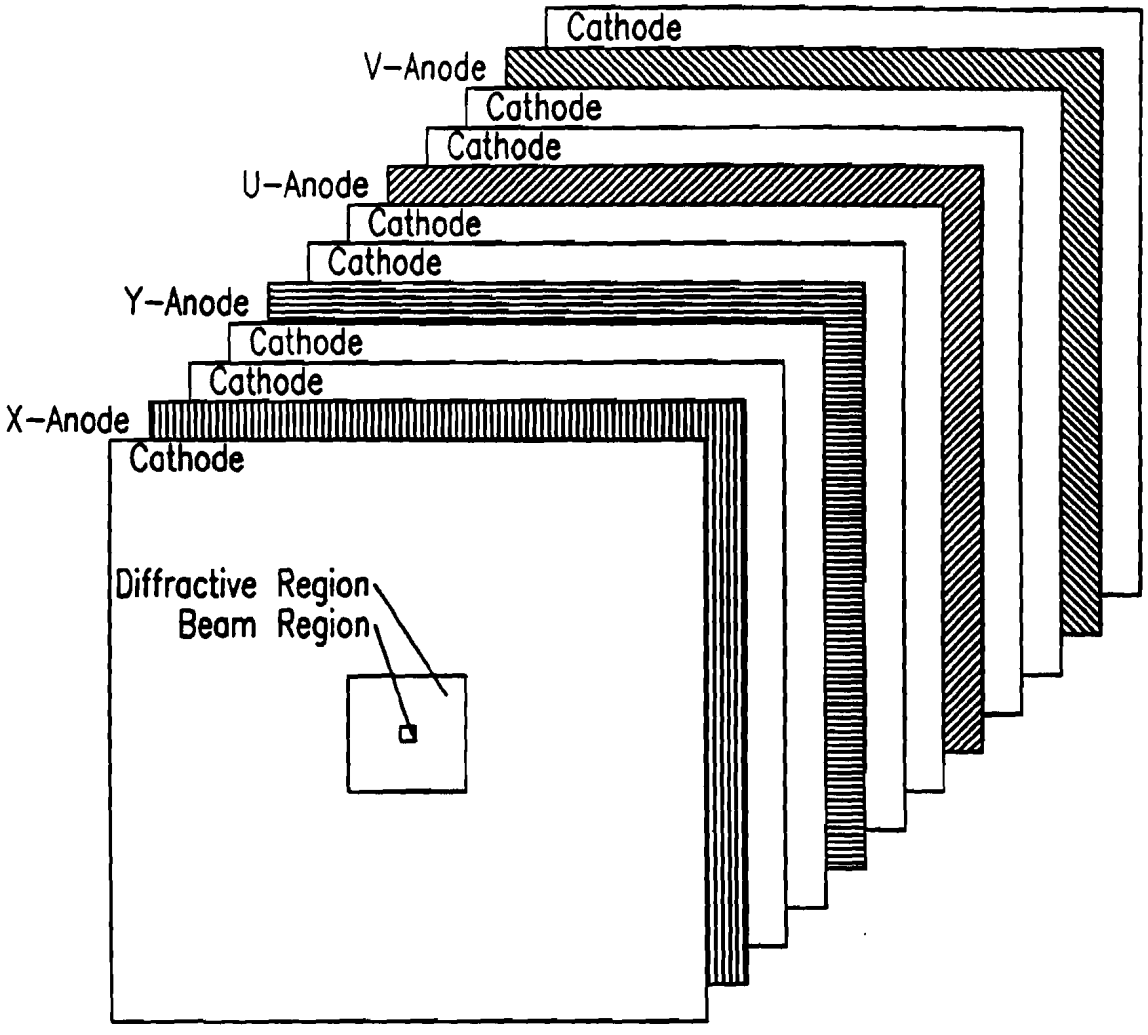

Figure 10 – Various planes of MWPC.

with high p_T electromagnetic showers. It was placed 9 m downstream from the target behind the tracking system. It consists of two sections, the Electromagnetic Calorimeter section (EMLAC) and the Hadron Calorimeter section (HALAC). Both the sections reside in a large stainless steel cryostat, supported by a gantry, which can be moved in a direction transverse to the beam axis. Fig. 11 shows a picture of the LAC. Within the cryostat, the electromagnetic calorimeter is located in front of the hadronic section. The cryostat was made of 1.43 cm thick stainless steel and covered on the outside with $\sim$ 25 cm of fiberglass and foam insulation. On the upstream side of the cryostat there was a 5.08 cm diameter beam hole covered with two thin layers of stainless steel sheets with a small gap between them. The beam window served the purpose of reducing the material placed in the beam. The beam was so adjusted that it pointed directly into this beam window of the cryostat. Two additional vessels were placed inside the cryostat along with the calorimeters. The first one, placed directly to upstream of EMLAC, was an argon excluder vessel filled with low density foam with a purpose to reduce the energy loss of the incident particles caused by the material in front of the readout sections of the LAC. The second vessel, made of stainless steel and filled with helium, had a cutoff conical shape. It was inserted into the beam hole of the calorimeters and served the same purpose as the beam window. A complete description of the LAC system can be found elsewhere[26].

The design specifications for the LAC were:

1. Nearly complete coverage at laboratory angles $22\,\text{mrad} < \theta < 160\,\text{mrad}$ for both photons and hadrons. At an incident momentum of 500 GeV/c,

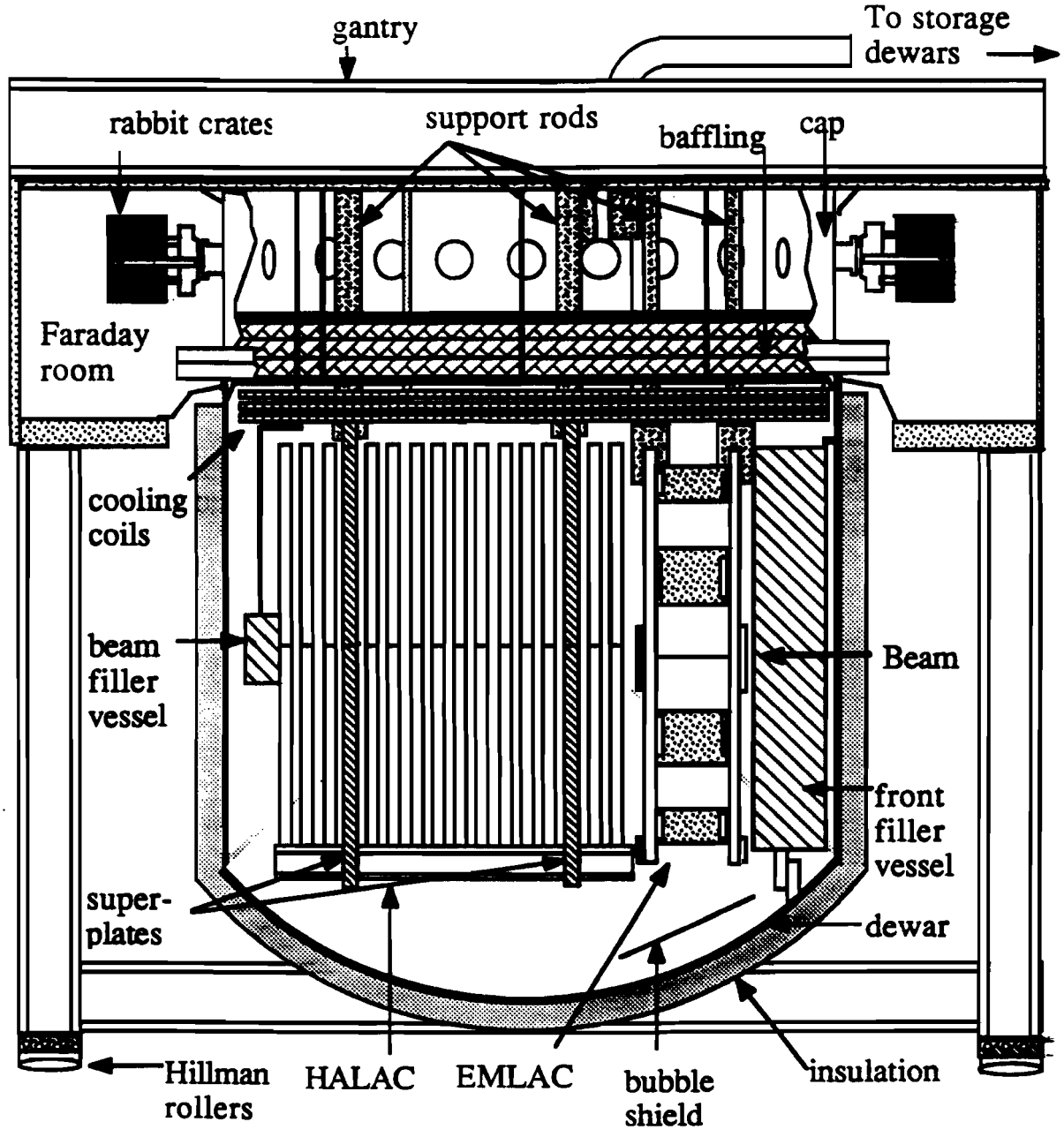

Figure 11 – The Liquid Argon calorimeter.

this corresponds to an angular range of $40° < \theta_{cm} < 138°$, or $\sim 77\,\%$ of the total 4π solid angle.

2. Energy resolution of $< 15\,\% \mathrm{E}^{1/2}$, and a positional resolution of < 0.1 cm for photons/electrons.

3. Good separation of isolated photons from photon pairs from π° decay up to energies of ~ 250 GeV/c.

4. Hadron energy resolution of $\leq 70\,\% E^{1/2}$, with a positional resolution of a few centimeters.

5. Electron/hadron separation at the 10^{-4} level.

6. Ability to sustain an interaction rate of $\geq 10^6$ Hz.

The Electromagnetic Calorimeter

The electromagnetic section of the LAC is subdivided into four mechanically independent quadrants, held together by the overall support structure. This is illustrated in Fig. 12. Each quadrant consists of 66 layers in which 2 mm thick lead plates are separated by 2.5 mm gaps of liquid argon from G-10 copper-cladded anode board (readout boards).

The G-10 readout boards are octant-sized and each octant is read out independently of the other. Alternate boards are used to read out the r coordinate and the ϕ coordinate in a polar coordinate system. The stack of these boards starts with a radial board. The radial boards consists of 256 strips in each octant, cut in such a manner that they are focussed on the target 9 m in front of the detector. The width of the strips on the first radial layer are ~ 0.55 cm.

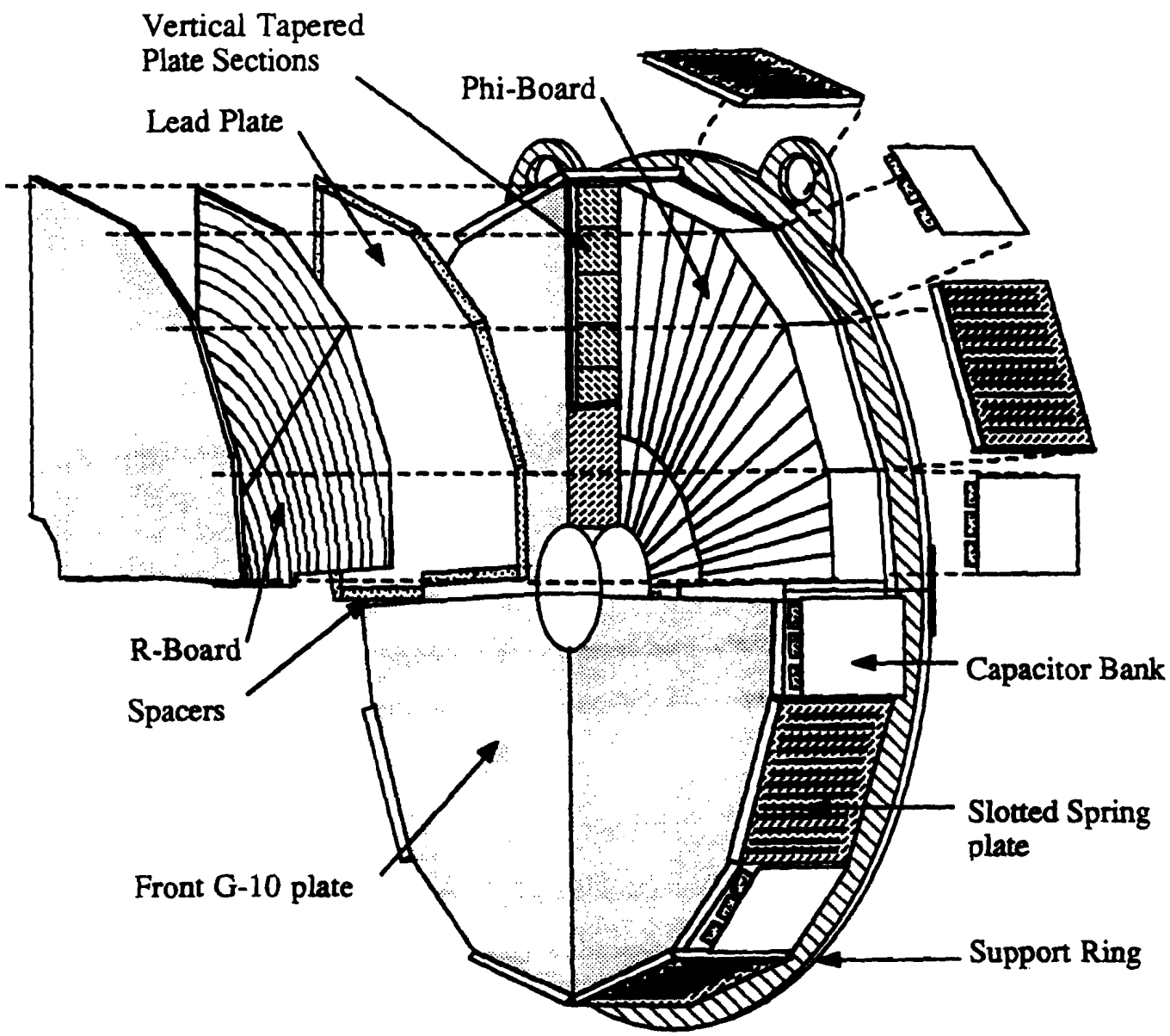

Figure 12 – The Electromagnetic Calorimeter. Also Shown are the alternating layers of r and ϕ view geometries.

The ϕ coordinate strips (azimuthal boards) are subdivided into inner and outer segments: inner region contains 96 copper strips and each strip subtends an azimuthal angle of 16.4 mrad while outer region contains 192 strips with each strip covering an angular range of 8.2 mrad. The transition from inner and outer ϕ -strips, occurring at a radius of 40.2 cm, corresponds to a laboratory angle from the target of 56 mrad, or a c.m. angle of 85° at an incident momentum of 500 GeV/c and helps to improve spatial resolution.

The EMLAC lead plates are 2 mm thick and have the shape of a single quadrant. In order to provide mechanical stiffness to the lead plates, a calcium-lead alloy was used. These plates have 20% more electrical conductivity than those of pure lead.

The calorimeter was read out in two sections called the front and back sections. The front section consists of 22 layers (about 10 radiation lengths), while the back section contains the remaining 44 layers.

The geometry covers a region of -1.0 to +1.0 units in center of mass rapidity for a beam energy of 530 GeV/c. It has full azimuthal coverage except at the quadrant and octant boundaries.

The Hadronic Calorimeter

Another sampling calorimeter which was positioned downstream of electromagnetic calorimeter was Hadronic Calorimeter (HALAC) whose purpose was to measure the energy and position of neutral hadrons. Since hadronic showers do not spread as wide as the electromagnetic ones, a very fine segmentation is not useful as it's in EMLAC. Therefore, readout pads rather than strips were used for hadronic calorimeter. The smallest pads, near the center, had areas of

$\sim 30\,cm^2$; the largest, at the outer edge, had areas of $\sim 150\,cm^2$. The design considerations for HALAC included good hadron energy and position resolution, enough longitudinal length to fully cover the hadronic showers, sufficient lateral segmentation to resolve neighbouring hadrons and with acceptance atleast as large as the EMLAC to detect the hadrons opposite high p_T π^o's and photons.

The HALAC consisted of 52 steel plates, 2.54 cm thick, for a total of ~ 10 interaction lengths. There were 53 layers of readout assembly and the readout planes were grouped into two sections longitudinally. The front section consisted of 14 layers (1206 readout pads) and the back section consisted of 39 layers (1134 readout pads). In between the steel plates there are detector planes called cookies which contain the charge collecting plates. These cookies consisted of seven layers of copper clad G–10 glued together into an octagonal unit of 4 cm diameter. The cookie contained the high voltage planes, argon drift gaps, and detector pads. Each high voltage board consisted of three double-sided 1/32 inches thick copper-clad G-10 boards, with the perimeter grounded. The readout pads, triangular in shape, were arranged in rows of two pad strips. These readout strips were covered with G-10 slats to provide structural rigidity for the cookies and to prevent the readout strips from themselves collecting any extraneous charge which might otherwise cause unwanted signal cross-talk between the pads. All pads were focussed in tower-like fashion towards the target, 9.83 m from the front of the HALAC. A detailed description of the HALAC can be found elsewhere[27].

2.7 Forward Calorimeter

The forward calorimeter (FCAL) placed approximately 15 m downstream of the target was designed to measure the energies of forward beam jet particles which escaped detection by the LAC because of low angle production along the beamline. The detector worked as a total absorption calorimeter.

The FCAL consisted of three cylindrical modules of alternating layers of iron and acrylic scintillator as shown in Fig. 13. The calorimeter had an outer radius of 57 cm with a 3.175 cm beam hole. The upstream and midstream modules contained 28 layers of iron and 29 layers of scintillator while the downstream module contained 32 layers of iron and 33 layers of scintillator for a total of 10.5 interaction lengths of material. These iron layers were 1.9 cm thick separated by gaps of 0.635 cm. The acrylic scintillator layers were 0.46 cm thick. The scintillator plates contained 76 clearance holes of 1.12 cm diameter on a 11.43 cm grid through which the 86.4 cm long wavelength-shifter (BBQ) bars were inserted. The outer rim and the beam hole of the scintillator was coated by a reflective white paint in order to reduce light losses. All hadrons which struck this detector were absorbed by iron producing scintillation light in layers of acrylic scintillator. The scintillation light was absorbed in light guides doped with BBQ which captured the blue light of the scintillator and converted into green light. This green light was transported to a photomultiplier tube which served as a readout system for the FCAL. By measuring the signals from the photomultiplier tubes and the location of the light pipes, one can easily determine the energy deposited in the calorimeter. A complete description of the FCAL can be found elsewhere[28].

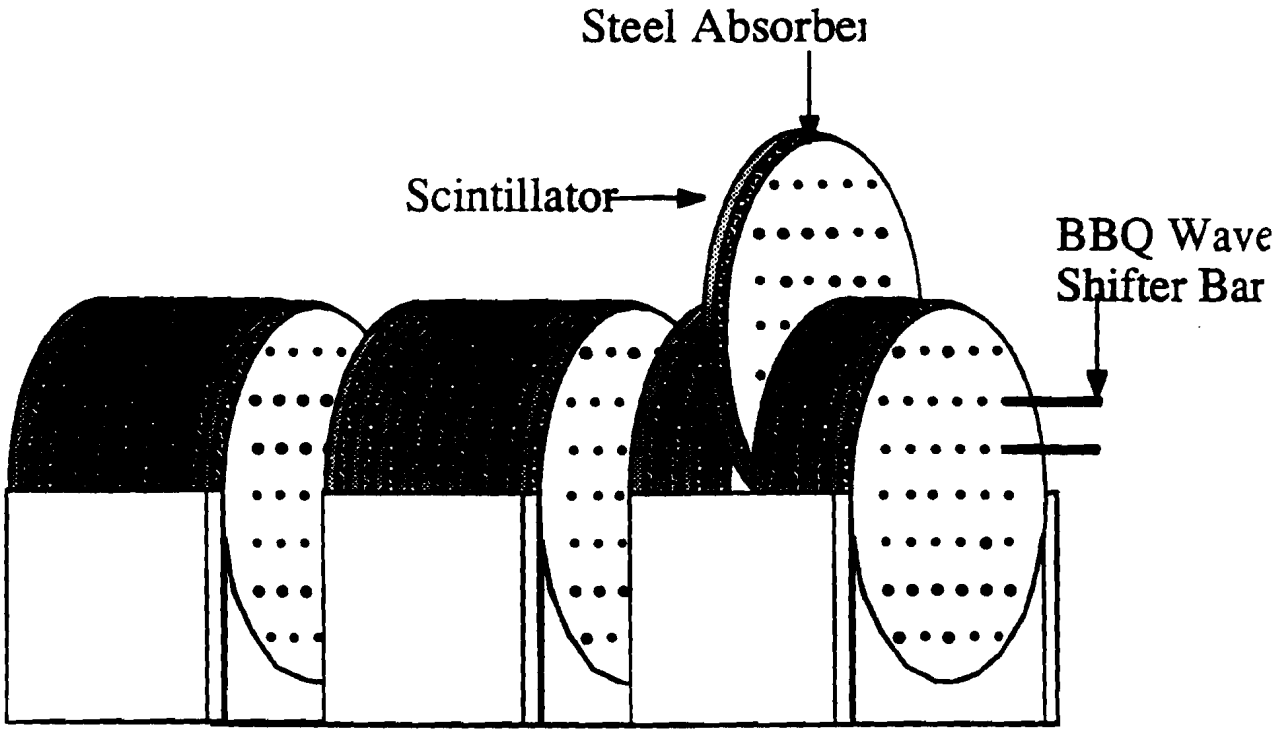

Figure 13 – The Forward Calorimeter.

2.8 TRIGGER

The experiment E706 was designed to trigger on the events which were of high interest as dictated by the physics goals of E706, namely the high p_T events. Since the direct photon cross-section falls off exponentially, the purpose of the trigger system was to select events with at least one high transverse momentum shower with ($p_T > 3.0$ GeV/c). The trigger was designed to perform at a rate of 10^6 interactions per second. The transverse momentum was estimated by the energy deposited in the EMLAC by the particles with high p_T. The trigger selection was done in three steps: beam and interaction definition, preselection of the interaction and the final selection of the event.

Beam and interaction definition Two plastic scintillation counters, BA and BB, were installed in the beam line directly upstream of the target. A beam particle (beam signal) was defined as the coincidence of the signals from these two counters without one in BH, ($BA \cdot BB \cdot \overline{BH}$), in coincidence with a *beam_gate* signal.

There were four other scintillation counters located downstream of the target. An interaction trigger was defined by the logical OR of the signals from these four scintillators (SE1, SW1, SE2, and SW2) in coincidence with a beam signal. A restriction was imposed on the interaction to qualify for the interaction trigger. It was required that no interaction took place within ± 60 ns of the present interaction in order to prevent overlapping of the signals from different events due to insufficient time resolution. The location of these scintillator counters and veto wall is shown in the Fig. 14. A more detailed description about the triggers used in this experiment can be found elsewhere[29].

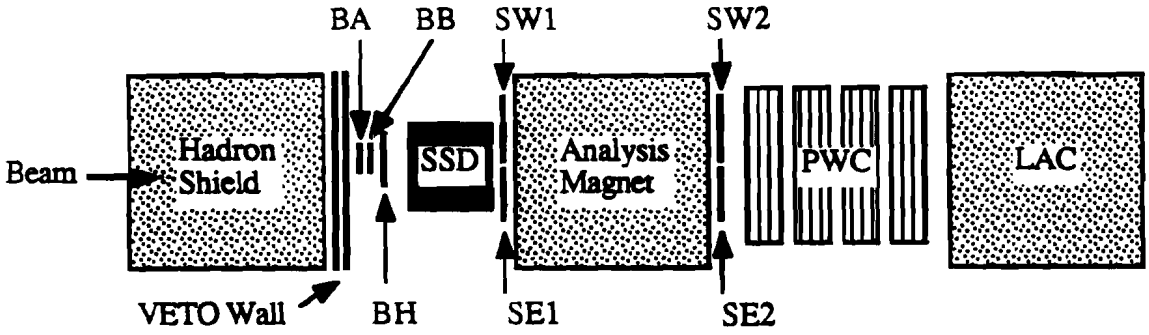

Figure 14 – Layout of the Veto Wall and Scintillation Counters. The size of the counters has been exaggerated with respect to the surrounding spectrometer components.

Preselection of an interaction

A pretrigger was defined in order to reject events which were of no interest i.e. low transverse momentum interactions. The basic idea was to trigger on events that produced a high $p_T$signal in any octant of the EMLAC. Since the detector measured the energy of an electromagnetic particle, the p_T, was defined by

$$p_T = E \times \sin(\theta)$$

where E was the amount of energy which was deposited and θ was the angle between the beamline and a line from the target to the point of deposition.

A global p_T signal was generated for each octant of the EMLAC by weighting

the energy deposited in the r-view (circular strips) of the octant according to the radial position of the showers. The octant global $p_T$was defined as the total p_T deposited in an octant. For the preselection of the event, signals from each octant were required to satisfy the following conditions:

- the p_T deposition within the innermost 96 r-strips or within the next 128 r-strips was at least $\sim$ 1.7 GeV/c and was correlated in time with the present interaction.
- the total amount of p_T deposited in the octant within the 300 ns time interval preceding the present interaction was less than $\sim$ 1.5 GeV/c. This requirement was imposed because the rise time of the LAC signals was of the order of 300 ns, and it was possible that a high global p_T signal was the sum of two low p_T depositions which occurred close to each other in time.

After the above conditions were satisfied, an octant pretrigger was generated by putting the octant global p_T in coincidence with the interaction trigger and in anticoincidence with discriminated global p_T signals present within the preceding 300 ns. The logical OR of all the octant pretriggers was put in coincidence with the interaction strobe and in anticoincidence with the two veto wall signals and SCRKILL. The veto walls planes are located just downstream of hadron shield and their function is to detect muons coming from the beam signal. These high energy muons can appear as direct photon by depositing energy in the EMLAC through bremstrahlung. The SCRKILL signal is produced by noise spikes which are due to the 400 Hz power supplies and had a width of 30 μsec.

A pretrigger signal is generated with the above configuration which qualifies

the event to be preselected. This signal was used as LOAD signal to latch the PWC/SSD and the FCAL information and also in the formation of final LAC triggers. When there are no other signals present, the beam and interaction, each prescaled and divided by a factor of 10^6, were used as both a pretrigger and final trigger. If the conditions were not satisfied , a reset signal was sent out and the experiment readied for considering the next interaction for preselection process.

Final selection of the Event

The final selection of the event was made on the signals from the LAC. Two methods were used to calculate the p_T in a given octant; the *LOCAL_PT* signal and the *GLOBAL_PT* signal. The *GLOBAL_PT* was the total p_T of the octant calculated by simply adding up all the *LOCAL_PT*. The *GLOBAL_PT* could also be generated from coherent noise (noise common to all channels) or from multiphoton events in which each photon has only a small fraction of the total p_T. The fine granularity of the EMLAC was used here to suppress above kind of triggers by imposing a *LOCAL_PT* condition. That means a substantial fraction of the global p_T in an octant had to be deposited within 16 radial strips of the calorimeter, roughly the size of a normal electromagnetic shower. Each of the two p_T signals from each octant were discriminated using different nominal thresholds, in coincidence with the pretrigger strobe. The final LAC triggers were formed using the two p_T signals and the different thresholds. The different thresholds settings are presented in the table 4.

The final LAC triggers are:

- *Local-Global-Hi* trigger was created when one or more octants in the EM-

Trigger Threshold Settings				
Logic Signal	**runs: 1811-2292**	**2293-2310**	**2311-2904**	**2905-3036**
Local p_T Low	1.2			
Local p_T high	4.2	3.6		3.0
Global p_T Low	2.5			
Global p_T High	4.0		3.6	

Table 4 – Trigger Threshold Settings by run number.

LAC had a *LOCAL_PT* signal which satisfied the lower p_T threshold and a *GLOBAL_PT* signal which satisfied the higher p_T threshold.

- *Local-Global-Lo* was similar to *Local-Global-Hi* but with a lower threshold. It was implemented to study the performance of the *Local-Global-Hi* trigger. Since most of the events were at low p_T the *Local-Global-Lo* trigger was prescaled by a factor of 10 to avoid the dominance of low p_T events.

- *Single-Local* required that a large amount of p_T had been deposited in a small region of a single octant. That means one or more octants had a *LOCAL_PT* signal which satisfied the higher local p_T threshold. This was a very efficient trigger at detecting single photons and π° decays.

- *Two-Gamma* trigger required that if an octant had a *LOCAL_PT* signal which satisfied the lower threshold then any of the remaining three octants on the opposite side also satisfied the low threshold.

Each of the four LAC triggers mentioned above, in addition, required that both the pretrigger signal as well as octant pretrigger signal have been generated. If no LAC trigger was satisfied, a reset signal was sent out to the electronics and

the system was readied for the preselection of the next event after 5 microseconds. But if a trigger was satisfied, an INTERRUPT signal was sent out to the data acquisition system to readout the data stored in different sections of the detector. When the computer finished collecting all the data, it sent a reset signal to the data acquisition system and the trigger system was again reset to process the next event.

3. Event Reconstruction

3.1 OVERVIEW

This chapter describes the offline reconstruction package used in this experiment to analyze the data taken during the run. This overall reconstruction package called, MAGIC[30], provides a framework in which various subreconstructors written for each part of the detector can be used independently if desired. The primary function of MAGIC is to read the primary data from the tape/disk, unpack it and then call the individual reconstructor subroutine for the event pattern recognition execution and finally to write the results to tape/disk. The task of error handling and controlling the number of events was also performed by MAGIC.

MAGIC is based on ZEBRA memory management package[31] and PATCHY[32], a code management package, developed at CERN. ZEBRA is a Fortran callable set of service routines which provides the facility for creating data structures and dynamic memory management. PATCHY switches allow one to turn on and turn off certain sections of the code as desired.

For the reconstruction of the data used in this analysis, MAGIC was run on DEC VAX, ACP and AMDAHL computers provided by Fermilab Computing Department. Code development was done on VAX computers and the resulting code was converted to ACP required environment for the first pass data processing. The ACP system is a parallel computing system designed to handle individual events completely by separate CPU's.

Since the work presented in this thesis requires results from the Tracking Re-

constructor and Electromagnetic–Shower Reconstructor, a description of these reconstructor along with a short description of ACP is given below.

3.2 Charged Track Reconstruction

The charged particle reconstruction was carried out by a reconstructor subroutine, called PLREC. A complete description of the algorithm employed in the reconstructor is given elsewhere (ref 24). The reconstructor or the algorithm uses Silicon Strip Planes(SSD's) for upstream tracking and vertex finding, Proportional Wire Chambers(PWC's) for the downstream tracking and an Analysis Magnet for momentum determination. The tracking was done by using two types of tracks: view tracks and space tracks. There were 4 different views (X, Y, U, V) for the PWCs and 2 views (X, Y) for SSDs.

Downstream Tracking The view tracks are formed by making a least-squared straight fits to three or four hits in each view. (A hit can be described as a coordinate of a wire in a plane which gets fired when a charged particle crossed it). These views tracks which are two-dimensional, are then matched between views to make a three-dimensional space tracks.

View tracks in each view were formed in two passes. In the first pass, the X and Y were chosen as the seed views and U and V were chosen as search views. A hit from each seed plane is taken to find slopes and intercepts of straight lines. Then the two remaining search planes for each set of seed planes are searched for the hits that would fall within ± 1.5 wire spacings of the line, as projected to that line. A four-hit track is formed if a hit is found in each search plane. If only one of the search planes has a hit then a three-hit track is formed. If no hits

are found in the search planes, then no view track is made. Least-squared fits were performed on all the candidate tracks. If the candidate track did not meet the χ^2 criterion, one of the hits from the search plane was dropped and another fit was attempted otherwise the track was stored as a view track. In the second pass, the role of the planes is switched. Seed planes were taken as search planes and search planes as seed planes and the process to find view tracks is repeated. Only those combinations which were not originally part of the four-hit track were considered. This second pass yielded in three-hit tracks with a hit missing in one of the outer planes. After making all the view tracks, the four-hit tracks were compared for the shared hits. A four-hit track with the best χ^2 sharing 3 or 4-hits was kept and the others were dropped. Three-hit tracks sharing 2 or 3-hits with four-hit tracks were also dropped.

After finding view tracks, an attempt was made to form space tracks. A similar kind of algorithm was used to find space tracks. In the first pass, the X and Y views were taken as the seed views and U and V were taken as search views. In the second pass their role is reversed. A space candidate track, formed from each seed view, was projected onto the search views tracks. The hits in each search view were compared to the projected hits of the space tracks. All hits which fall within ± 1.5 wire spacing were stored along with the hits which made the seed track. In order to consider this set of hits as a space track, the following conditions were imposed:

- There should be a minimum of two hits per each view.
- There should be a minimum of four hits from all search views.
- There should be a minimum of six hits from the seed views.

- There should be a minimum of thirteen hits in total.

Finally, a track cleanup was performed to eliminate spurious tracks. If two space tracks share 6 or more hits, the one with the lower number of hits is dropped. If they have the same number of hits, the one with the lowest χ^2 is kept and other one dropped. If a track has 9 or more hits which are shared by any other track, then it is always kept.

Upstream Tracking The algorithm employed to find SSD view tracks is almost identical to the algorithm used to form the PWC view tracks. There are four planes each with a set of two orthogonal views. For high multiplicity events, SSD strips were clustered into single strips to minimize the CPU time. As with the PWCs, a track was required to have at least three hits out of a total of four hits.

There were three beam planes with X and Y views. A three-hit track is formed using the three hits, one from each plane. Then from the remaining hits which were not used in the three hit tracks, two hit view tracks were formed. Ambiguities between more than one beam track were resolved using the vertex positions.

Magnet Linking between SSD and PWC tracks Matching or linking of the upstream and downstream tracks was done in the magnet by projecting these tracks to the center of the magnet. Since the field lines were in the XZ (bend) plane, magnet bent charged particles along the X direction. The angular difference of each pair is compared to find the best match. If this best match passes a predetermined cut, it is selected as a linked or a physics track. The charge and

momentum of the physics track is calculated from the formulae as

$$q = \frac{\theta_1 - \theta_2}{|\theta_1 - \theta_2|} \times \frac{B}{|B|} \tag{1a}$$

$$\sqrt{p_x^2 + p_z^2} = p_{xz} = \frac{q\,B\,L_o}{\sin\theta_1 - \sin\theta_2} \tag{1b}$$

$$p_x = p_z \tan\theta_x \tag{1c}$$

$$p_y = p_z \tan\theta_y \tag{1d}$$

where q is the charge sign of the track, B is the field strength, L_o is the effective length of the magnet, p_x, p_y and p_z are the three components of the momentum, $\theta_{y(x)}$ is the angle of particle trajectory relative to the z axis in the YZ (XZ) plane, and θ_1 *and* θ_2 are the angles, relative to the z axis, at the exit and entry points of the magnet region, in the XZ plane.

Vertex Finding Vertex reconstruction was done using the four hit view tracks in the SSDs that linked with PWC tracks. If no such tracks are present, then all the 3-hit tracks which linked with the PWC tracks were used for the vertex reconstruction. If there are not enough tracks satisfying the selection criteria, the vertex finding routine was aborted. The view vertex finding procedure is the same in both the X and Y views.

To find the vertex, a χ^2 minimization approach was adopted which uses slopes and intercepts of the individual tracks to locate the spatial point. Impact parameter is calculated at that point and a track with the largest impact parameter is eliminated from the next iteration. This process was continued

until either the average impact parameter of all the tracks associated with that vertex is less than 20 μm or the largest impact parameter on an individual track is less than 50 μm or only two tracks were left. The views were then matched to obtain the best vertex.

3.3 Electromagnetic–Shower Reconstruction

The reconstruction of the electromagnetic shower generated in the EMLAC is done by a program called EMREC[33]. As mentioned earlier, EMLAC is divided into two sections, front and back. There are four views (left R, right R, inner ϕ and outer ϕ in each quadrant. The reconstruction is done independently for each quadrant. Also for the reconstruction purposes, corresponding strips in the front and back are added together to form a software summed section. The reconstruction process involves four steps : (1) finding groups of channels (strips) that contain significant energy deposition (2) reconstruction of GAMMAs from energy peaks detected in each view (3) correlation of GAMMAs from different views to form the final photons and (4) obtaining photon time of arrival from the TVCs (time to voltage converters). (The GAMMAs represent an intermediate step in the final photon reconstruction.)

Before the reconstruction process starts, one has to convert the raw ADC (analog to digital converter) data from each strip to deposited energy, E_i. The conversion is done using the relation

$$E_i = A_i G_i (N_i - N_{oi}) \tag{2}$$

where A_i is the normalization factor for the EMLAC, G_i is the relative gain for the channel, N_i is the digitized value of the pulse height in the channel and N_{oi} is

the pedestal offset in the ADC counts. The normalization factor for the EMLAC was determined from the electron beam data and it was about 3.1 MeV per ADC count. A correction to the bad strips occurring due to the bad connection or dead amplifier was also applied at this time. It was done by assigning a average of the two adjacent strips to the affected strip. This helped in improving the resolution for the isolated electromagnetic showers.

Group and Peak Finding For any particular view, a group is defined as a series of consecutive strips with energy above a predefined threshold. The following conditions are necessary for a set of strips in order to pass as a group:

- There must be at least three strips above threshold in left and right views and the inner ϕ view. For the outer ϕ view, the requirement is reduced to 2 strips because of the larger width of the strips.
- The total group energy must be at least 750 MeV.
- The average energy per strip in a group must be above 150 MeV.
- The strip with the maximum energy must contain more than 300 MeV.

Once the group is defined, the search for the peaks starts. A candidate for a peak is identified when the slope of the energy distribution in the group changes from a positive to a negative value. Associated with each peak candidate are two valleys located at either side of the peak. A valley is defined as the strip with the lowest deposited energy between two peaks, or the end strip in the group. For each peak found in the summed section, the peak finding algorithm is applied to the front section also since adding energy between the front and the back section tends to lose low energy peaks. If a candidate for a peak is

found in the front section, its expected variance is calculated as

$$\sigma = \sqrt{(0.1)^2 + (0.14)^2 E} \tag{3}$$

where E is the energy of the peak-strip, σ is the estimated energy variance for E, $0.14\sqrt{E}$ gives the intrinsic energy resolution of the EMLAC due to shower sampling fluctuations (calculated using GEANT) and factor of 0.1 is the incoherent noise contribution to the total resolution. If the energy difference between the peak strip and its valleys on either side is greater than $2.5\,\sigma$, then this candidate peak is considered as a real peak as opposed to an energy fluctuation.

GAMMA Reconstruction The reconstruction of a GAMMA from a peak depends on the group it originated from. For single-peak group, this was just a matter of fitting a parametrized shower shape to the peak and using it to determine the energy. But a multiple-peak group must first be split into several one-peak groups before the positions and energies can be calculated. (The parametrization of the shower shape was determined using the GEANT based E706 Monte Carlo program.) For multiple-peak groups, the following function was minimized

$$\chi^2 = \sum_i \frac{1}{{\sigma_i}^2}(e_i - \sum_k E_k f_k^i)^2 \tag{4}$$

where f_k^i was the fraction of the energy from shower k which would be deposited in strip i, based on the parametrized shower shape. This minimization could be explicitly solved for the individual shower energies E_k (ref 33). Once the energies were found, the energy distribution for each individual shower was found by subtracting the contribution from all other showers in the group. The resulting

distribution was used to calculate a new position for the shower. Using these new positions, eq. (3) was recalculated and minimized to yield the final "GAMMA" energies. The radial position of a GAMMA was calculated as

$$R_i = (20.22 + i_r \times 0.55)\text{cm} \tag{5}$$

where R_i was the strip position and i_r was the strip number. The azimuthal position was given by

$$\phi_i = (i - 1) \times 0.0164 + (quad - 1) \times \frac{\pi}{2} \tag{6}$$

where ϕ_i was the azimuthal angle of the strip, i was the strip number and $quad$ refers to the quadrant number of the EMLAC.

Correlation into Photons The third step of the reconstruction process was to correlate the GAMMAs to form the final photons. As described in the chapter 2, G-10 boards alternate between radial (R views) and azimuthal (ϕ views) boards. Therefore a photon would deposit roughly equal amount of energy in each view. The algorithm worked out by matching GAMMAs of equivalent E_{front}/E_{total} ratio. Some requirements were imposed to make the process easier such as requiring that the inner ϕ GAMMAs only correlate with R GAMMAs that have a radius less than 40 cm and outer ϕ GAMMAs correlate with R GAMMAs with a radius greater than 40 cm. Problems arose at all boundaries of the views because the program had difficulty in cases where the energy was shared between four regions.

Photon Timing The time of arrival associated with each photon, was calculated using the information stored in the TVCs of each individual strip.

3.4 ACP

The ACP system was designed at Fermilab with a primary focus on event-oriented multiprocessing. It consists of a digital μVAX computer, which controlled many ($\approx 20-60$) dedicated microprocessor *nodes*. These nodes or CPUs are based on Motorola 68020^{TM} microprocessor chips. The high speed 32-bit ACP Branchbus connects up to 16 crates of Single Board Computer (SBC) per branch to each other and to the host computer. The SBCs are single-board computer with CPU and up to 16kbytes of memory with an option of additional extension boards available. The ACP boards include six Mbytes (initially two Mbytes) of memory and the Motorola 68882 floating-point coprocessor (FPU).

An application program destined to run on the system must be divided into two parts. One, running in the host, handles all the I/O work. The other, running in each node, does the actual event processing. The ACP provides system subroutines to communicate between the host and node programs. Routines exist to broadcast calibration constants at the beginning and to sum statistics at the end of the run. Individual events were sent, and results retrieved, asynchronously, by user-called send and get subroutines. The ZEBRA memory management package and the HBOOK histogramming package, are also implemented on ACP. Converting programs to meet the multiprocessor requirements is relatively easy, aided by a full, multiprocess simulator that runs on a VAX.

E706 made full use of the ACP system for the event processing. The μVAX read the spectrometer data from the tape and downloaded data from one event to each processor node using ACP's send routines. Each node would then perform the unpacking and reconstruction for a single event. When a node completed

its task, the results were fetched back using ACP's get routines residing at the host. It would then write the results to an output tape and load the node with another event. A block diagram of the basic system is shown in Fig. 15.

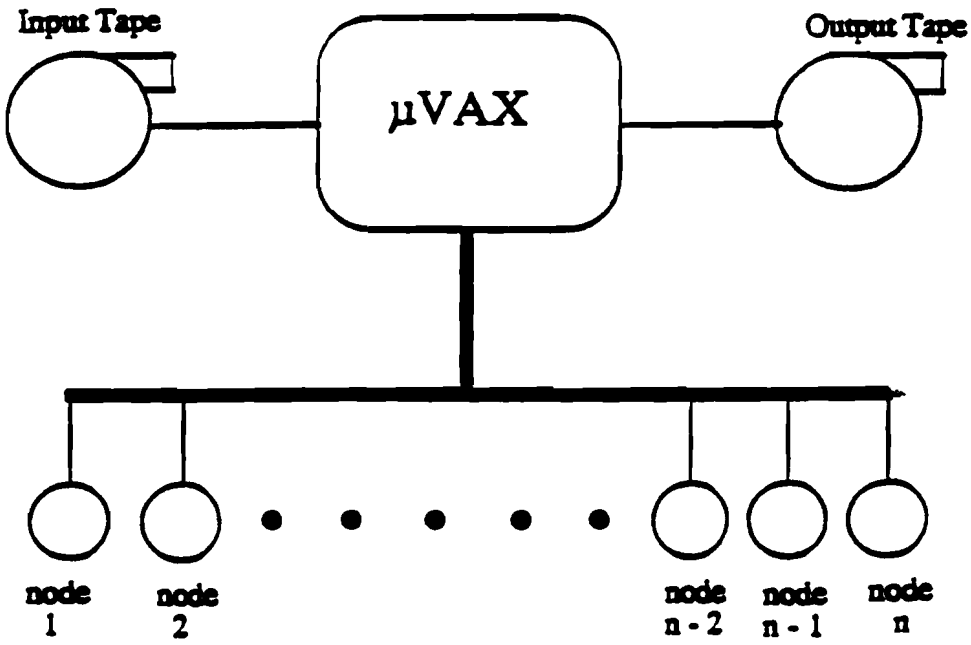

Figure 15 – Block Diagram of ACP Computing System.

4. Event Selection and Data Analysis

4.1 OVERVIEW

This chapter describes the procedure and the several cuts applied to obtain the event sample used in this work. The data sample used in the analysis was collected during the period between Jan. 4 and February 13, 1988. Five million trigger were obtained during this period. This running period was divided into several sets of runs as illustrated in table 5. The different data sets correspond to different beam polarities and different targets. Calibration runs and data taken without electromagnetic triggers are not included here. Runs later than set E as well as set B have been ignored in this analysis because some part of the tracking system was not functioning normally. Here, sets are ordered alphabetically in reverse. Table 1 also shows the total number of events considered for this analysis.

Set	Beam	Target	Run Number	Events
A	Neg	Cu+Be	2852 - 3036	786,171
C	Pos	Cu+Be	2588 - 2670	1,224,950
D	Neg	Be	2062 - 2382	1,242,178
E	Pos	Be	1728 - 2007	1,508,174

Table 5 – Data sample from 1987-88 running period used in this analysis.

The summary of the results from the primary analysis was written to Data Summary Tapes (DST). These DST's were used for the secondary analysis. The events contain all types of LAC triggers with no p_T cut applied yet.

Since the primary aim of this work was to obtain a good sample of strange particles and then to use them to study strangeness components of the jets produced in hadronic interactions with various kinds of triggers, cuts were applied in two stages. The first stage of cuts helped in establishing a selection criteria for strange particles. The criteria selected tracks which clearly originated from a secondary vertex and which combined to give a momentum consistent with a neutral particle from the primary vertex. After obtaining a good and clean sample of events containing strange particles, second set of cuts were imposed. Those events which survived the second stage of cuts were the only ones which were accepted for jet analysis (described in next chapter).

4.2 Pre-selection of Events with Strange Particles

In this pre-selection of events for Jet analysis, any event trigger which satisfied at least one of the following was considered. The conditions (defined in section 2.8) are: *Local-Global-Hi*, *Local-Global-Lo*, *Single-Local* and *Two-Gamma*. About 60% of the events recorded during the physics runs satisfied these triggers. A series of cuts were applied to the data, in order to suppress background. These requirements are listed below.

On the event level there were 4 requirements:

- There was a good beam particle definition from the beam counters.
- The next requirement was to have a reconstructed vertex confined within the experimental target region. This was done by checking the Z location of the reconstructed primary vertex. The event was rejected if the two orthogonal views did not match within 3 mm. In Fig. 16, the Z distribu-

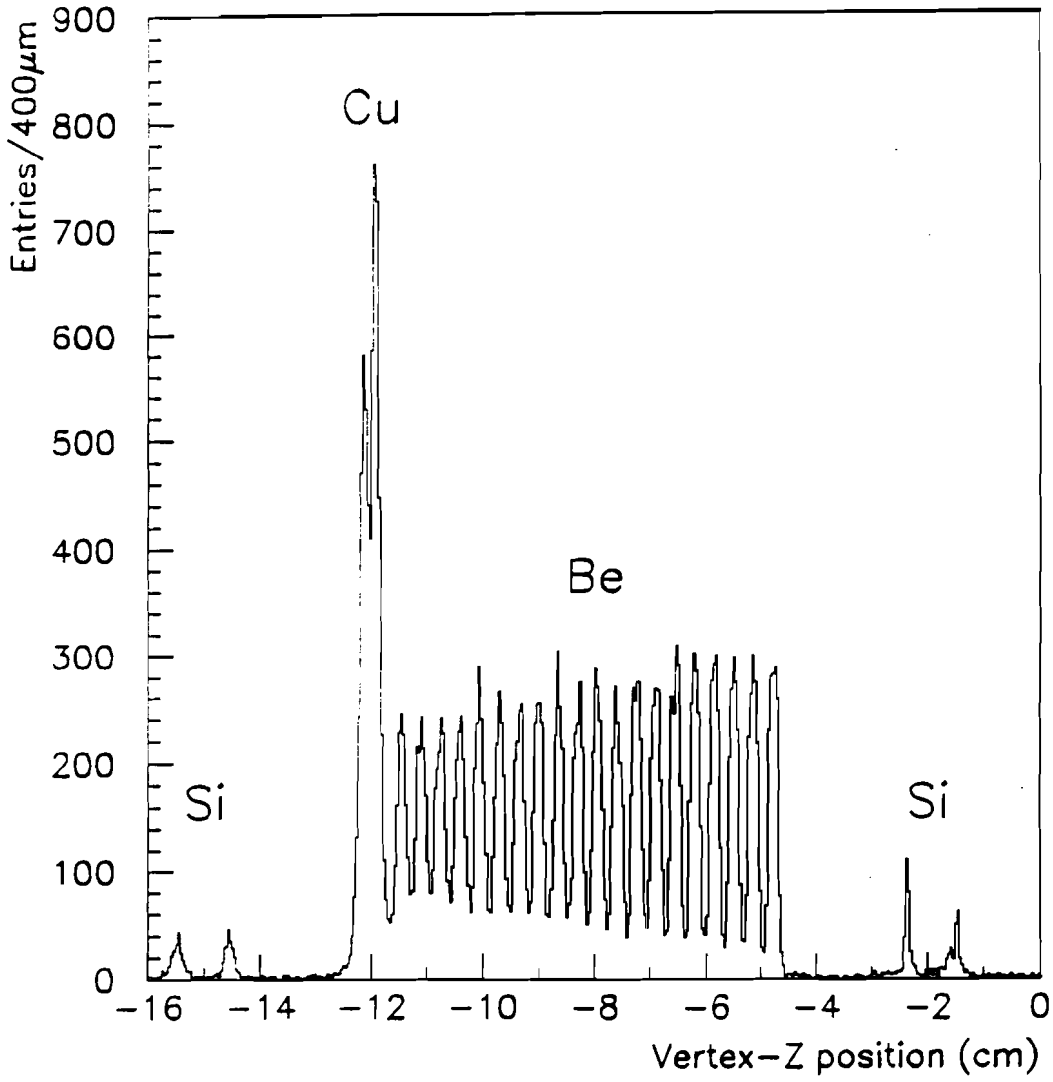

Figure 16 – Z coordinate distribution of the reconstructed vertices in the target.

tion of the reconstructed vertices in the target is shown. First two peaks correspond to the copper target and the remaining 20 correspond to the beryllium target. The vertex reconstruction efficiency was 90 %. Around 75 % of the events survived this cut.

- To avoid combinatorial background as well as when PWC planes or SSD planes were noisy, events with number of tracks more than 40 were eliminated. This requirement reduces events by ~ 1 %.

- Events with at least two well reconstructed downstream tracks were considered for this analysis. The χ^2 per degree of freedom from the fitting of the tracks must be less than 3.0. Also, tracks were required to have momentum lower than 150 GeV/c because the uncertainty in the momentum determination was too large for higher momentum tracks. When the momentum is above 150 GeV/c , the relative error in the momentum is

$$\frac{\Delta P}{P} = \frac{0.1P}{100.0} = 0.15$$

which is non-negligible. Hence any momentum measured above this value is likely to have a big error associated with it. Also they should originate from the primary vertex. This was checked by projecting the tracks to the target region. The track had to be within 1 cm of the reconstructed vertex.

4.3 Monte Carlo Studies

Simulation technique is a very important tool to interpret the experimental data. One develops huge reconstruction and analysis programs to achieve their experimental goal. These programs need to be tested before they could be applied to the real data. Monte Carlo schemes are used to do this kind of task. In the present work, a program was written to reconstruct and analyze neutral strange particles. Various software cuts were applied that favored the neutral track pairs coming from the secondary decay vertices. To decide exactly where the cuts should be applied, a monte carlo package GEANT was used.

Strange particles were produced in the monte carlo using the full E706 charged spectrometer simulation which models decay kinematics, material and

the PWC acceptance and resolution. A standard monte carlo generator called PYTHIA was used to generate simulated events. Events were produced using the same initial environment as were the real data. The simulated events were then subjected to the same flow of reconstruction code as the real data. A set of cuts was then obtained which when applied to these simulated events would maximize the signal to noise ratio. These cuts include impact parameter cut, p_T asymmetry of the decayed tracks relative to the parent particle system. A very clear and narrow invariant mass peak was obtained for the K^0_s which is shown in Fig. 17. As one can see, the background contribution to the signal is very small thus enhancing signal to noise ratio.

4.4 V° Particle Reconstruction

Various steps were taken to reconstruct the V^0(decaying neutral particle) particle which was produced at the target and decayed inside the magnet.

Candidate tracks for strange particles were required to have an impact parameter transverse to beam axis greater than 6 mm in order to remove tracks originating from the primary vertex. Fig. 18 shows the impact parameter calculated for all the downstream charged tracks (solid line) superimposed on the monte carlo data (dashed line). This was the first cut obtained from the monte carlo studies.

An oppositely charged pair was regarded as a converted photon when the difference in x slope was less than 0.0005 and difference in y slope was less than 0.0015 and the difference in y intercept was less than 0.001. These pairs, called ZMP[34] (Zero Mass Pair) tracks , were rejected.

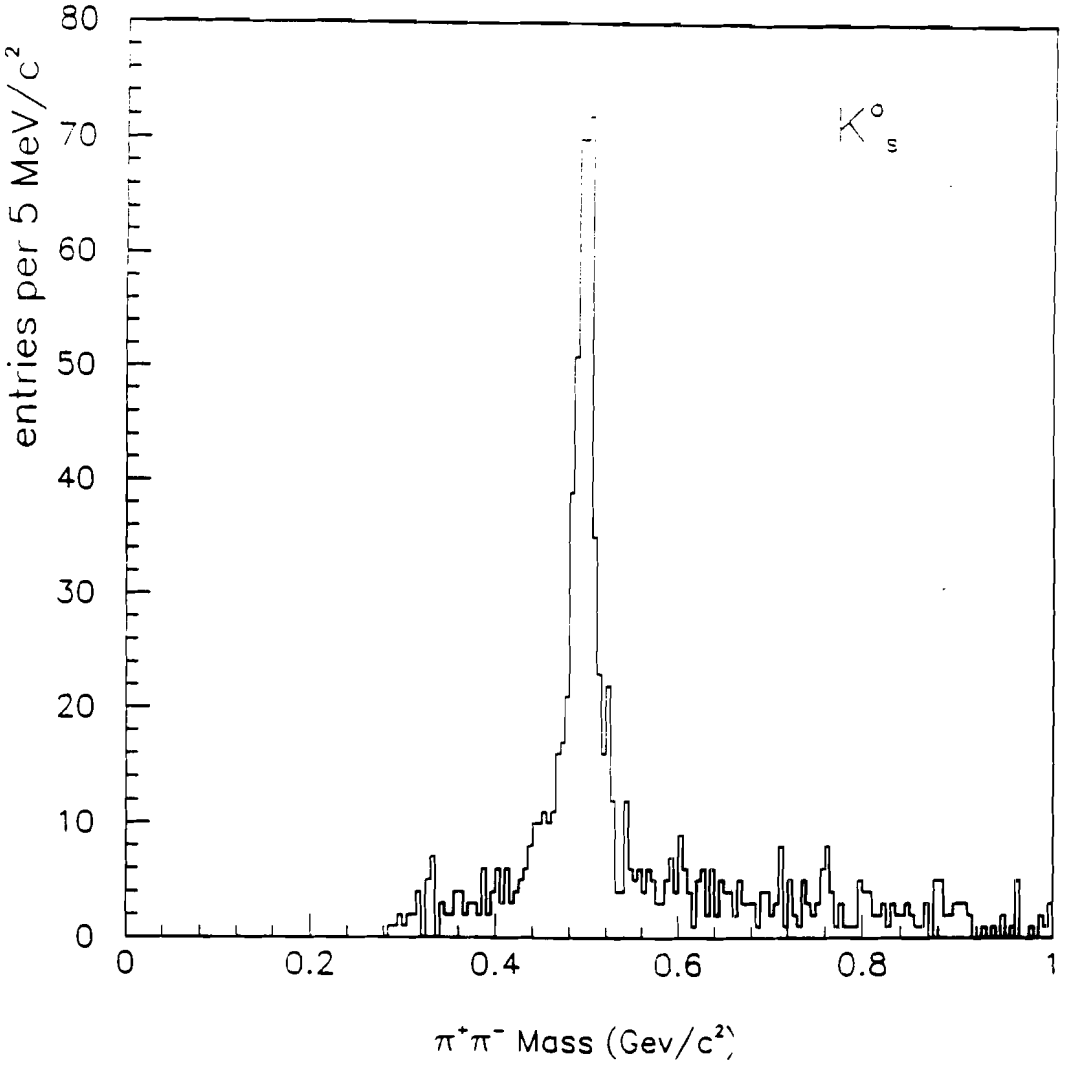

Figure 17 – Invariant mass distribution for K^0_s obtained from the Monte Carlo data.

The algorithm for finding V^0's began with a systematic pairing of all charged particle candidates. An interaction point for pairs of two tracks in the Y–Z plane was calculated using slope and intercept of the downstream tracks and chosen as assumed decay point for V^0 as shown in the Fig. 19. The pair was discarded if the decay point did not fall between the Z window, front part of the magnet. This Z window was chosen inside the magnet in order to stay away from the interactions which occurred due to various interaction counters placed in front

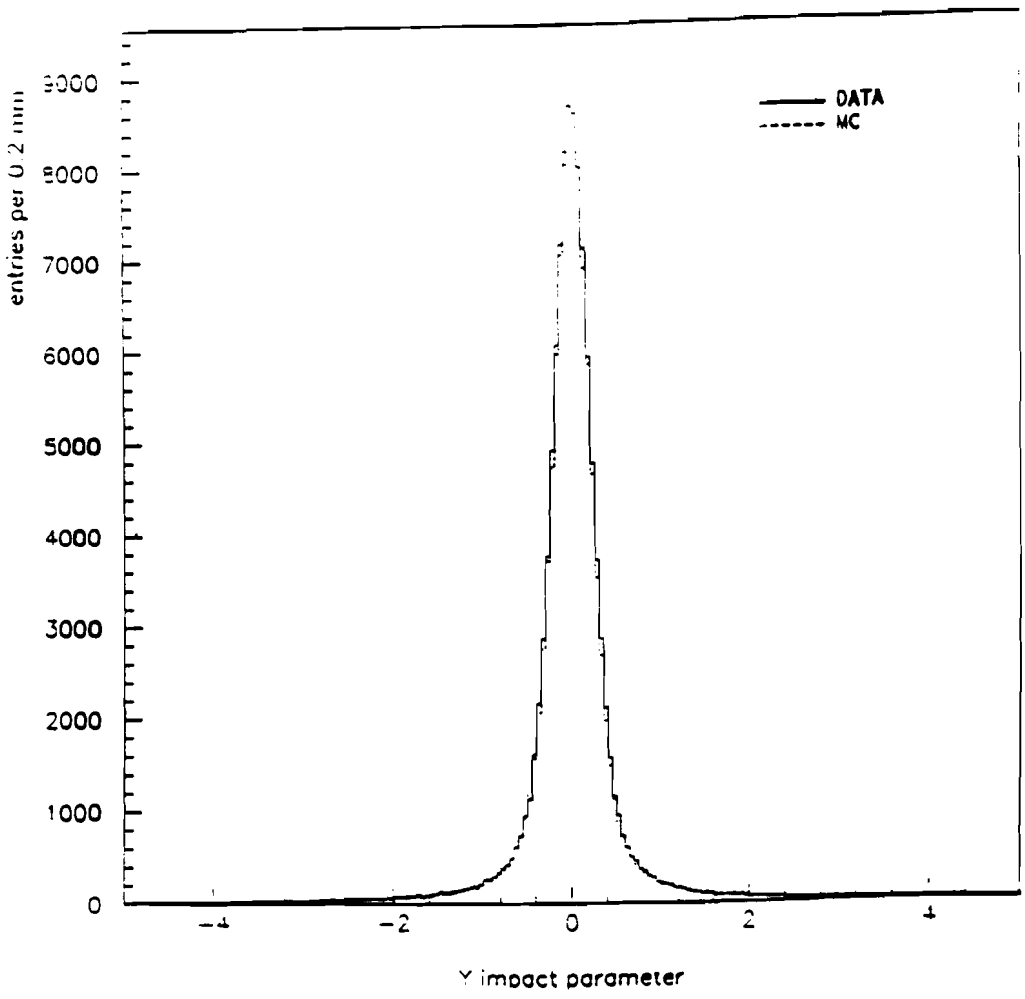

Figure 18 – Impact Parameter distribution for downstream space tracks (solid line). Superimposed is Monte Carlo data (dashed line).

of magnet, silicon panel of SSD's and the helium bag. The helium bag which was placed inside the magnet in order to avoid interactions due to air, collapsed near the end of the run and gave rise to some secondary interactions. The Z window was taken from 90 cm to 190 cm which is just before the middle of the magnet.

Using downstream slopes and intercepts of the two candidate tracks in ques-

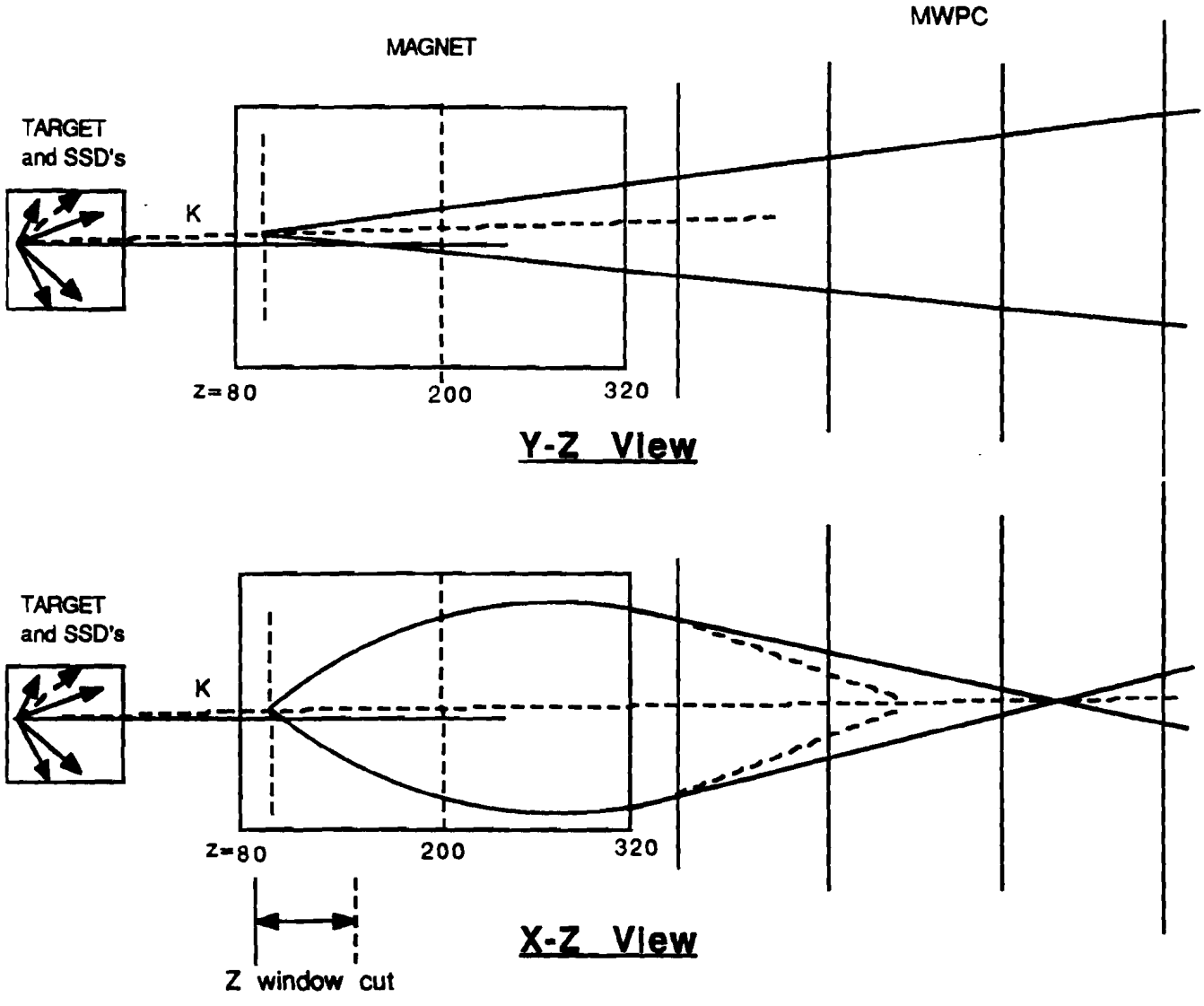

Figure 19 – Schematic diagram showing strange particle search in both the views. Production and decay point for K_s^o is also depicted in the diagram.

tion , one can easily obtain Y and Z location of the decay coordinates of neutral strange particle. Since the X location of the decay point is undetermined because magnet bends the charged particles in X–Z view only, a special momentum fit routine was written which would re-calculate the momentum and the charge of the candidate track in question. A loop over the possible value of X decay coordinate was taken which when passed through this special momentum fit routine along with other two decay coordinate, would yield new values of momentum and charge.

The formulae used to calculate momentum and the charge of the neutral strange track are the following:

Suppose a neutral strange particle decays at X_1 & Z_1 location into two opposite charged tracks which travels through the magnet under the magnetic field towards the PWC system. The charged tracks bends towards or away from the field depending on their charge. Let X_2 & Z_2 be the location of the track at the rear end of the magnet. Using the slopes and the intercepts from the PWC, one can calculate Z_1, Z_2 and X_2 location for the track. X_1 is the possible value of the track in question. Also, one can define m_{Dx} as the downstream slope of the track in X view. Then, one can write equations of circle as

$$(X_1 - X_A)^2 + (Z_1 - Z_A)^2 = {R_A}^2 \tag{1}$$

$$(X_2 - X_A)^2 + (Z_2 - Z_A)^2 = {R_A}^2 \tag{2}$$

where the unknown parameters X_A & Z_A are the location of the center of curvature and R_A is the radius of the curvature for the track. Also, using elementary

calculus according to which the product of two slopes is equal to -1, one can write

$$\frac{(X_2 - X_A)}{(Z_2 - Z_A)} \times m_{DX} = -1 \tag{3}$$

where the first term of the product is slope of the radius.

Using equations (1), (2) & (3), we can solve for X_A, Z_A & R_A and obtain the following expressions.

$$X_A = X_2 + \frac{1}{m_{DX}}(Z_2 - Z_A) \tag{4}$$

$$Z_A = Z_2 - \frac{1}{2} \times \frac{(X_1 - X_2)^2 + (Z_1 - Z_2)^2}{(X_1 - X_2)/m_{DX} - (Z_1 - Z_2)} \tag{5}$$

$$R_A = \sqrt{(1 + \frac{1}{m_{DX}{}^2})(Z2 - ZA)^2} \tag{6}$$

The upstream slope, m_{UX} of the track in the X view is given by

$$m_{UX} = \frac{(Z_A - Z_1)}{(X_1 - X_A)} \tag{7}$$

and in the Y view

$$m_{UY} = m_{DY} \tag{8}$$

where m_{DY} is the downstream slope of the track in the Y view.

If B_o is the magnitude of the effective magnetic field, then the charge, Q of the decayed particle can be obtained by

$$Q = \frac{(m_{UX} - m_{DX}) \times B_o}{|\,(m_{UX} - m_{DX}) \times B_o\,|} \tag{9}$$

The momentum in the XZ plane, P_{XZ} is given by

$$P_{XZ} = (0.3 \times Q \times B_o \times R_A) \tag{10}$$

Therefore the three components of the momentum of the decayed track is given by

$$p_z = \frac{P_{XZ}}{\sqrt{1 + {m_{DX}}^2}} \tag{11a}$$

$$p_x = p_z \times m_{DX} \tag{11b}$$

$$p_y = p_z \times m_{DY} \tag{11c}$$

And the total momentum of the track is given by

$$P = \sqrt{p_x^2 + p_y^2 + p_z^2} \tag{12}$$

In parent particle system, since p_T of the decayed tracks should ınce, therefore, for each possible X_1 location, a difference in p_T of decayed ·· cks, Δp_T is obtained which is given by the equation

$$\Delta p_T = ([(p_{1x}\cos\theta_x - p_{1z}\sin\theta_x) + (p_{2x}\cos\theta_x - p_{2x}\sin\theta_x)]^2 + [(p_{1y}\cos\theta_y - p_{1z}\sin\theta_y) + (p_{2y}\cos\theta_y - p_{2x}\sin\theta_y)]^2)^{1/2} \quad (13)$$

where the subscript 1 or 2 denotes the decayed track number and $x, y \,\&\, z$ are for the components. The $\theta_{x(y)}$ is the production angle which neutral strange particle makes in $x(y)$ view.

A best possible X_1 location for the decay location is obtained by picking up the minimum balanced Δp_T from the Δp_T's obtained from all the possible X_1 locations. Monte Carlo studies reveal that by imposing a cut of 0.6 on Δp_T of the opposite charged pair, we can reduce background substantially. In Fig. 20, relative p_T asymmetry for the pair is shown. Since V° search algorithm finds the best possible X location of the decay point, the relative p_x asymmetry distribution falls rapidly. But in y-view, the Y decay point is given by PLREC algorithm where the probability of error is more, one obtains a long tail in relative p_Y asymmetry distribution. Therefore, a cut on relative p_T asymmetry distribution rather than individual components was imposed.

Also, in order to suppress more background, it was required that candidate tracks must have momentum greater than 1 GeV/c. The reason is that when the momentum of a particle is below 1 GeV/c, it may curl up in the magnet and hence will not be detected in PWC's (ref 24).

The measured momenta allowed both the mass and momentum of the neutral particle to be calculated.

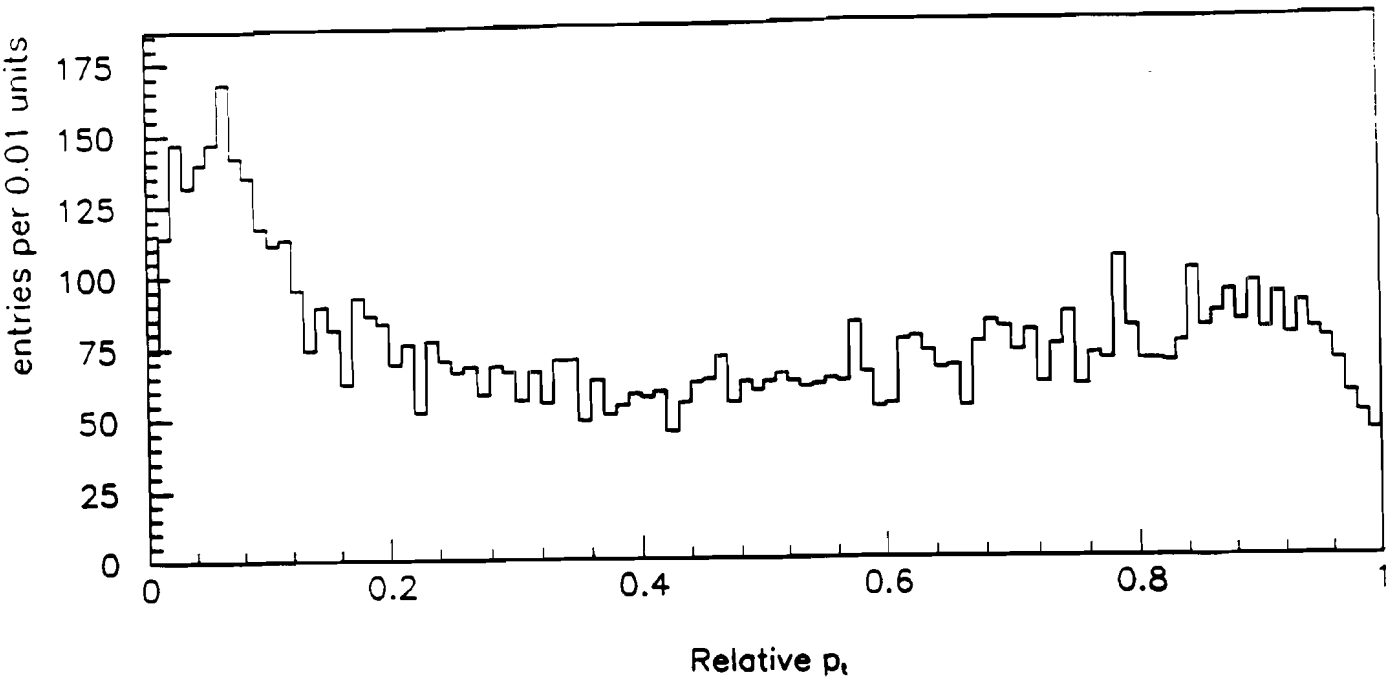

Figure 20 – Relative p_T asymmetry distribution for opposite charged pair.

4.5 V° Particle Identification

On each reconstructed V° the following kinematic fit hypotheses were tried: $K^\circ_s \rightarrow \pi^+\pi^-$, $\Lambda \rightarrow p\pi^-$, $\overline{\Lambda} \rightarrow \bar{p}\pi^+$. The identification of V° events as K°_s or Λ or $\overline{\Lambda}$ was made from the mass distribution and the $\cos\theta^*$ plot for each mass hypotheses where θ^* is the decay angle in the parent particle center of mass system.

Differences in the decay kinematics and in the lifetimes of the K's and Λ's require slightly different identification techniques for the two particles.

K°_s Identification

Neutral K°_s meson production is studied by reconstructing the K° decaying to $\pi^+\pi^-$, whose decay vertex is separated from the event vertex. Combinations

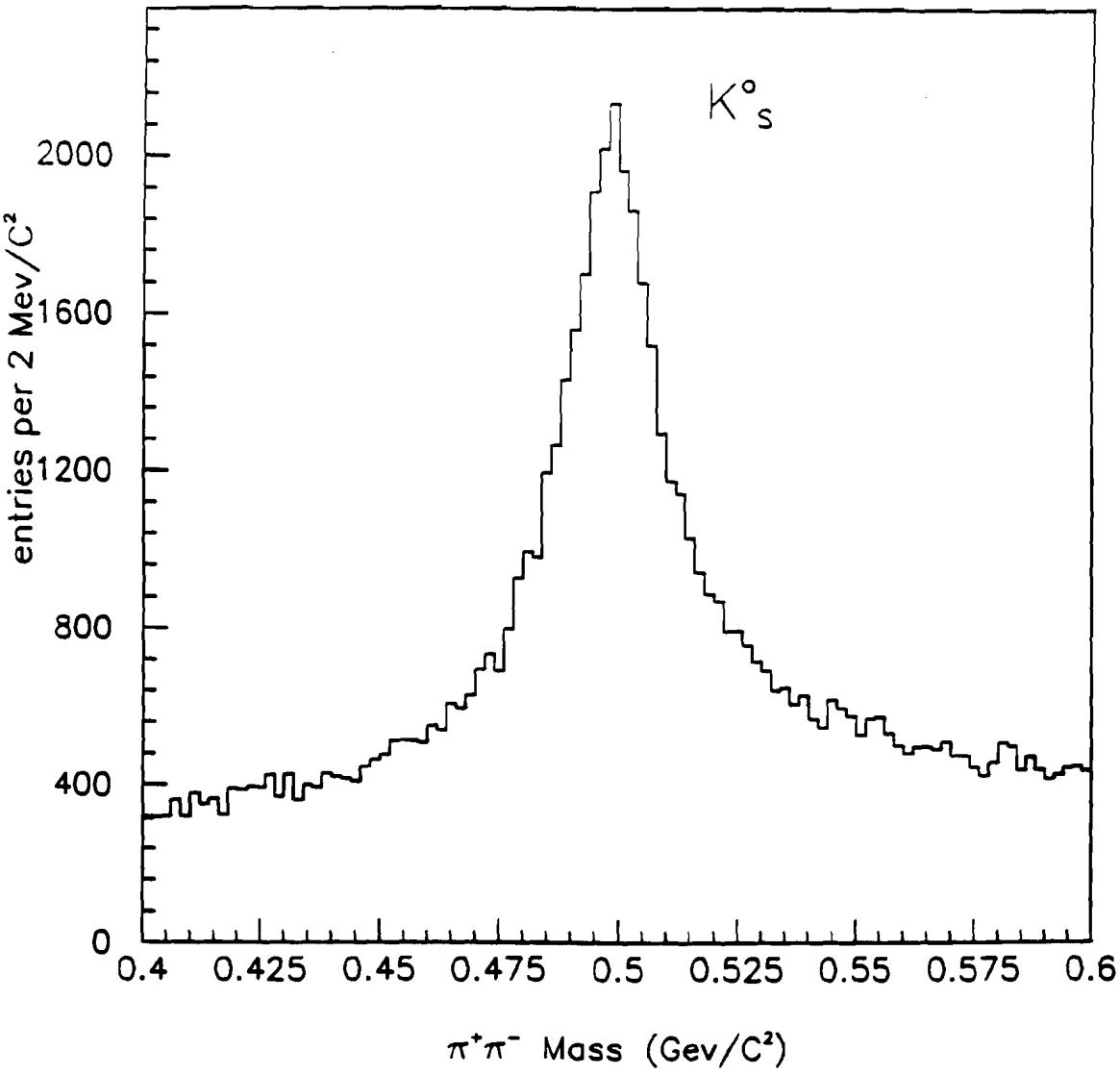

Figure 21 – Invariant mass distribution with a $\pi\pi$ mass assignment for oppositely charged track pairs passing all geometrical cuts.

are formed for opposite sign tracks. Fig. 21 shows the $\pi^+\pi^-$ invariant mass spectra of pairs in the range $0.4 < x < 0.6$ GeV/c^2 surviving these cuts where both tracks are assumed to be pions. A narrow peak is seen at the mass of the K^0_s over a small combinatorial background.

K^0_s candidates with masses within 40 MeV/c^2 of the nominal mass are defined

to lie in the signal region while those with masses between 407 and 447 MeV/c^2 or 547 and 587 MeV/c^2 are considered as sideband contribution. Pairs which lie under the sideband region are used here to estimate the contribution from this background and are subtracted from all the physics distributions. There are about 49480 K^0_s which fall under the signal region and 20628 in the sideband region and thus yielding a background subtracted signal of 28752 $\pm$ 265 K^0_s. (An attempt was made to get a lifetime distribution for kaons at this point resulting in very low lifetime which indicated that more carefully understanding of the signal is needed.) In the further careful study of strange particles, more room for suppressing background was discovered by imposing some more cuts as well as cleaning the K^0_s-signal, thus enhancing signal to background ratio. The justification for applying some more cuts is described below.

p_T cut

In Fig. 22, x_F (Feynman-x) versus p_T is plotted for all pairs of oppositely charged tracks which makes kaons. The pairs which satisfy Λ or $\overline{\Lambda}$ mass hypotheses have been removed to have a better understanding for kaons.

A clear enhancement in the forward region was observed. Since kaon production occurs predominantly in the central region[38], less concentration in the backward x_F region reflected poor acceptance of the detector in the backward region. (The experiment was not designed to study strange particles. The study of strange particles was a by-product from the experiment and it usefulness helped us in studying momentum scale in the magnet.) Also seen a. ome K^0_s produced at high p_T which is a clear evidence of strange particles prc ced at high transverse momentum, probably in jets. A big cluster of kaons as ob-

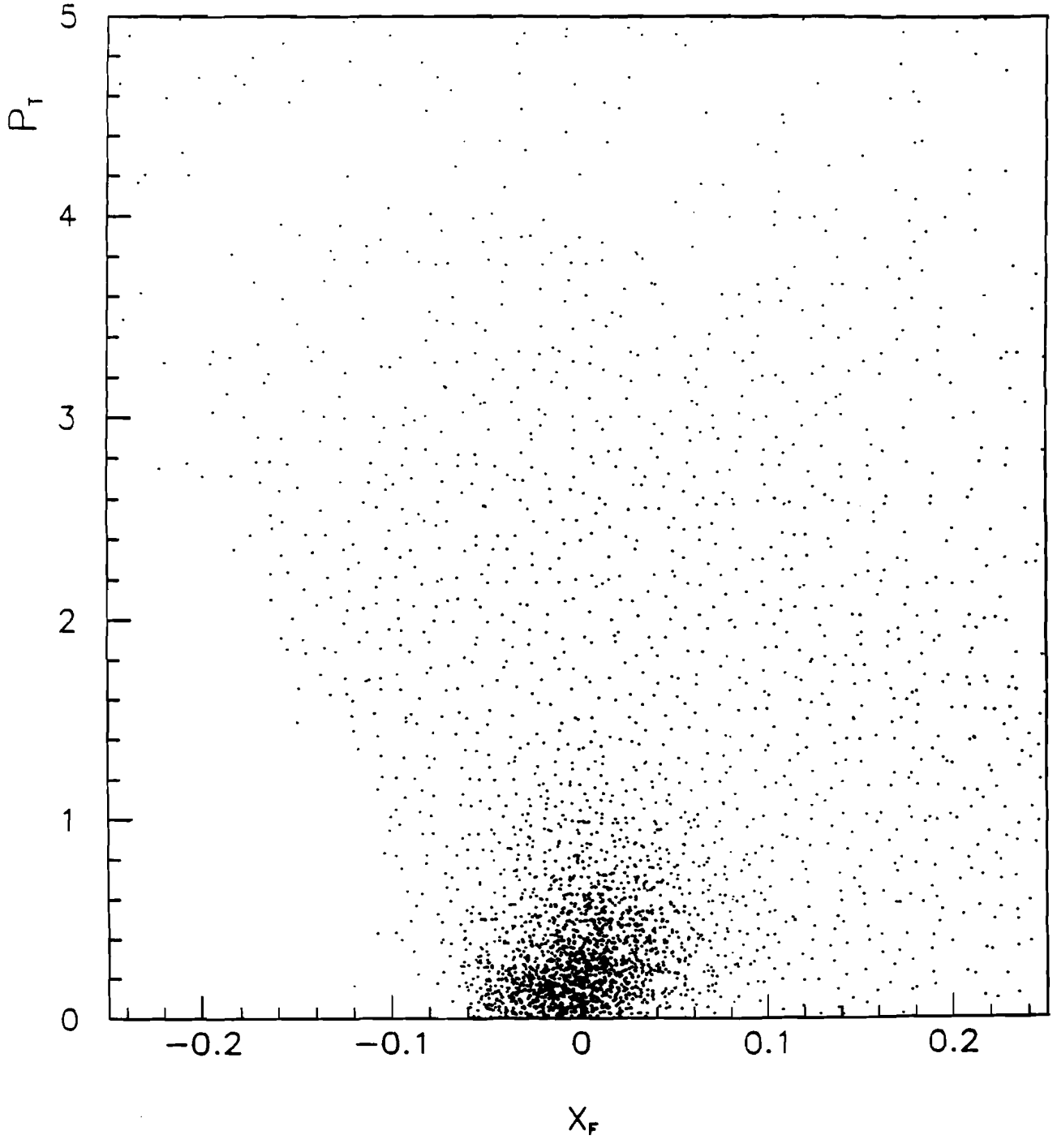

Figure 22 – p_T vs x_F distribution of K^0_s.

served in negative x_F region and at low $p_T(< 0.4\,GeV/c)$, the source of which could not be explained immediately. To understand this unusual concentration, the plot was divided into four regions: negative and positive x_F and a p_T cut of 0.4 divided momentum scale into low and high region. Invariant mass distribution for kaons was plotted for the four regions of x_F versus p_T distribution. (This p_T cut of 0.4 later turned out to be consistent with our jet algorithm described in chapter 5 which requires tracks with p_T more than 0.4 GeV/c).

In Fig. 23, invariant mass distribution for K_s^o in four regions of x_F vs p_T plot is shown. In figures (a) and (b) where high p_T region dominates, a clear and sharp peak at the K_s^o mass is seen. In Fig. (c), one can easily observe that background contribution is increasing at low p_T and in the forward x_F region. Also the peak is getting wider. In Fig. (d), the signal is completely lost due to the enormous contribution from background. Thus, by applying a lower p_T cut of 0.4 on the p_T of K_s^o , we can remove a big chunk of background from the signal.

Z-window cut

In Fig. 24, K_s^o mass versus Z decay point of K_s^o in the signal region is plotted. A strong band at nominal value of K_s^o seems to appear at low Z which gets faded as one approaches high Z decay point. Looking horizontally along this band which is at the nominal value of K_s^o mass, a careful examination reveals that this band bends towards low mass region as Z increases and approximately after Z = 120 cm, it again bends towards high mass region. After Z 140 cm, it's almost lost thus implying that it's harder to reconstruct K_s^o which are very fast forward. Since lifetime distribution falls exponentially, one is likely to

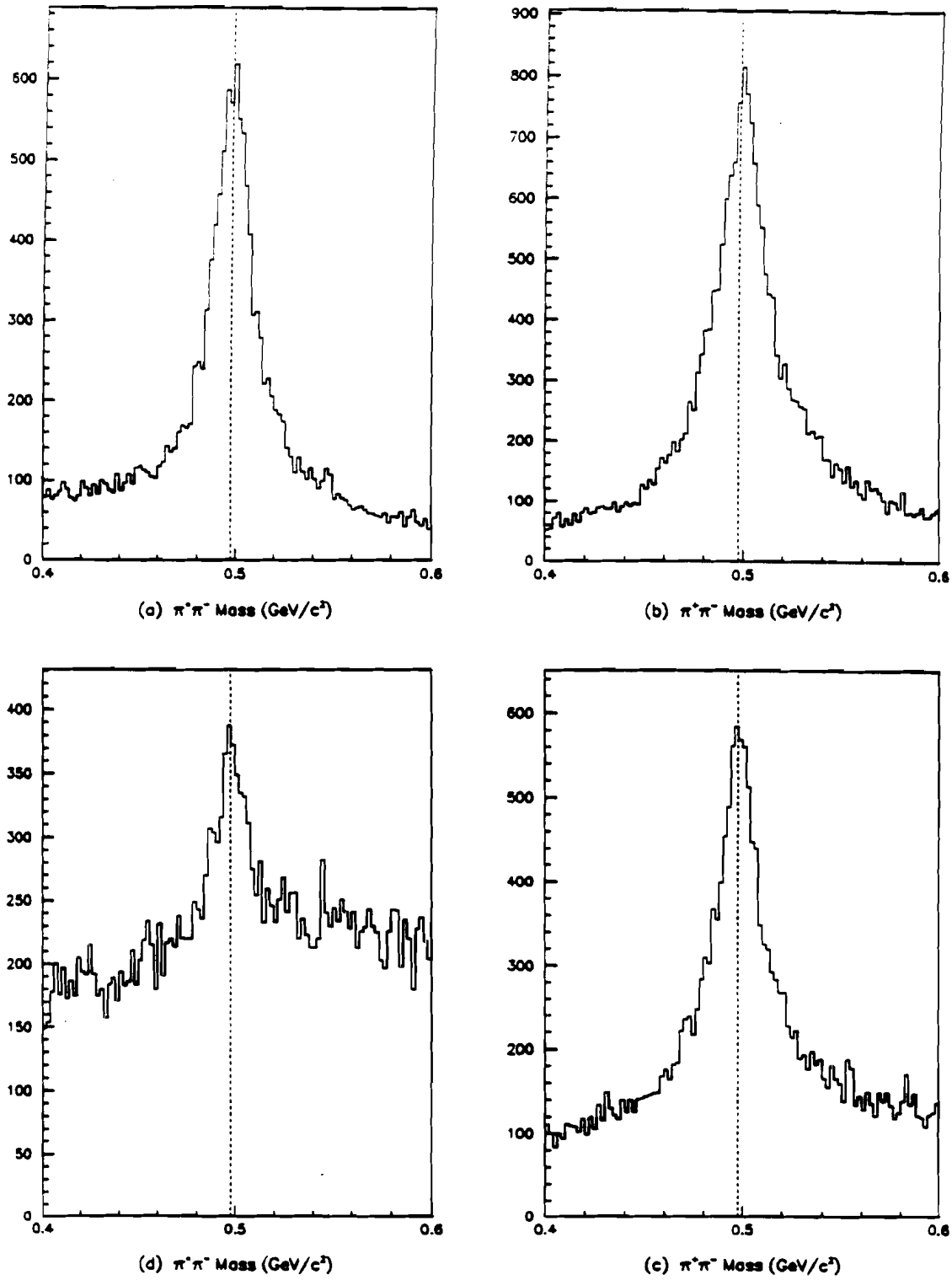

Figure 23 – Invariant mass distribution for K^0_s in four $x_F - p_T$ regions. (a) $x_F \leq 0.0$, $p_T > 0.4$, (b) $x_F > 0.0, p_T > 0.4$, (c) $x_F > 0.0$, $p_T \leq 0.4$, (d) $x_F \leq 0.0$, $p_T \leq 0.4$.

reconstruct less K_s^o as we go along distance and thereby increase the probability of making wrong combination and thus adding more fake K_s^o in the signal as well as in the background region. It becomes more obvious when we plot invariant mass distribution for the four sections of Z scale as shown in Fig. 25. It's clearly evident that mass peak becomes wider, background contributions increase and mass peak starts shifting as we move along Z scale. The drifting of the mass along Z can be explained as due to the non-linearity of the field in the magnet. The fringe effects due to the magnetic field at the boundaries of the magnet have not been included at this point.

Therefore putting a cut of Z = 140 cm on the Z-decay point of K_s^o and a lower p_T cut of 0.4 should increase signal to background ratio for K_s^o.

Cosθ^* Distribution

Once one assumes a hypothesis for the masses of the particles, it is a straightforward matter to calculate the momentum of the decaying particle and the decay angle in its rest frame, θ^*, from the observed laboratory angles of the parent and secondary tracks. One can obtain an almost clean sample of kaon and lambda decays in the following way.

In a $\Lambda/\overline{\Lambda}$ decay the $p/\overline{p}$ tends to carry off most of the laboratory momentum of the parent, and is therefore likely to be emitted at a smaller angle relative to the parent direction than is the accompanying pion. If such an asymmetric decay were interpreted as a Kaon it would yield a larger value of $|\cos\theta^*|$. Conversely, a kaon decay with $\cos\theta^*$ near zero would produce a symmetric decay in the laboratory, and such a decay could be interpreted as a $\Lambda/\overline{\Lambda}$ only by giving the $\Lambda/\overline{\Lambda}$ a small laboratory momentum.[36]

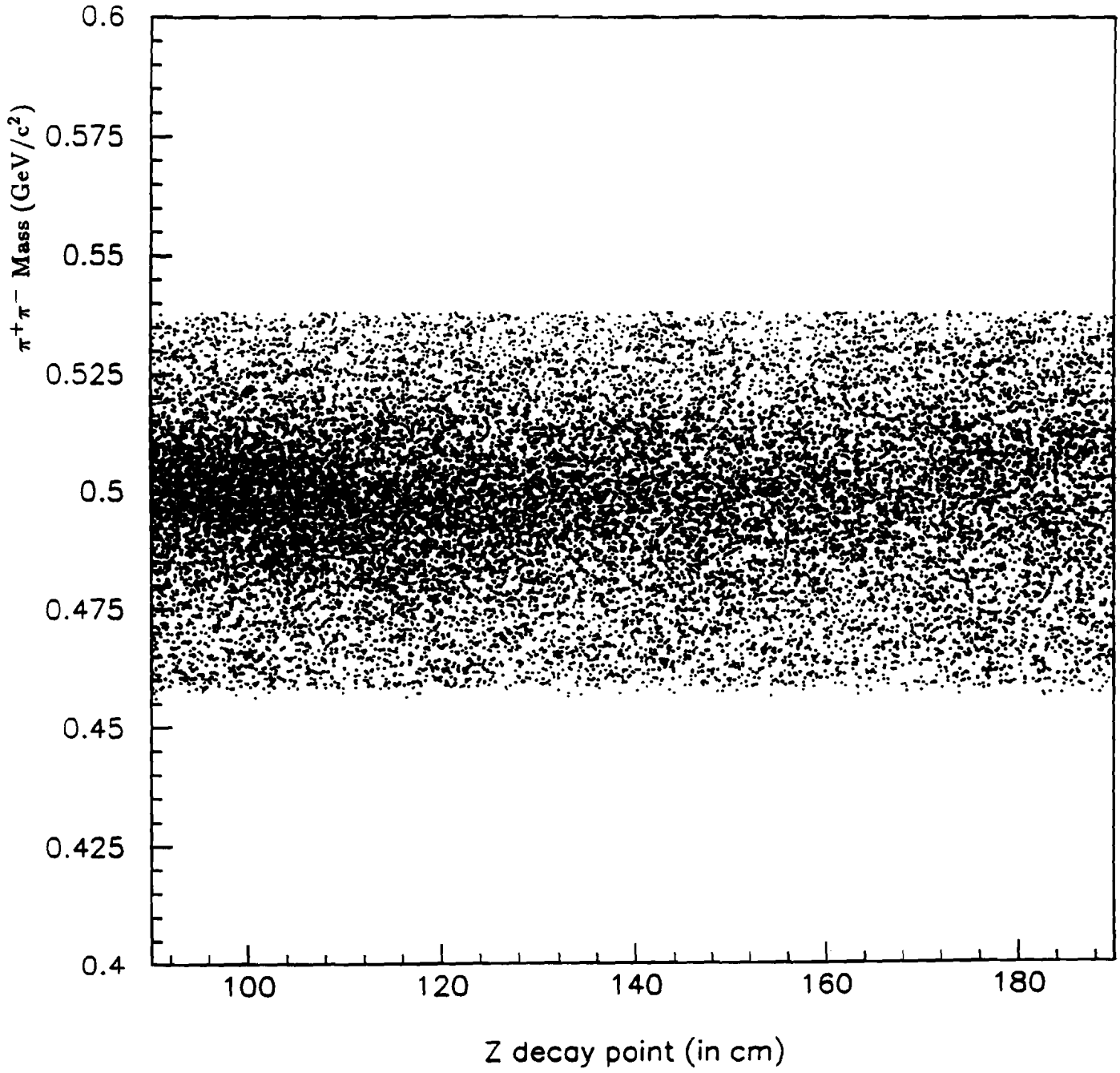

Figure 24 – K^0_s mass versus Z-decay point distribution.

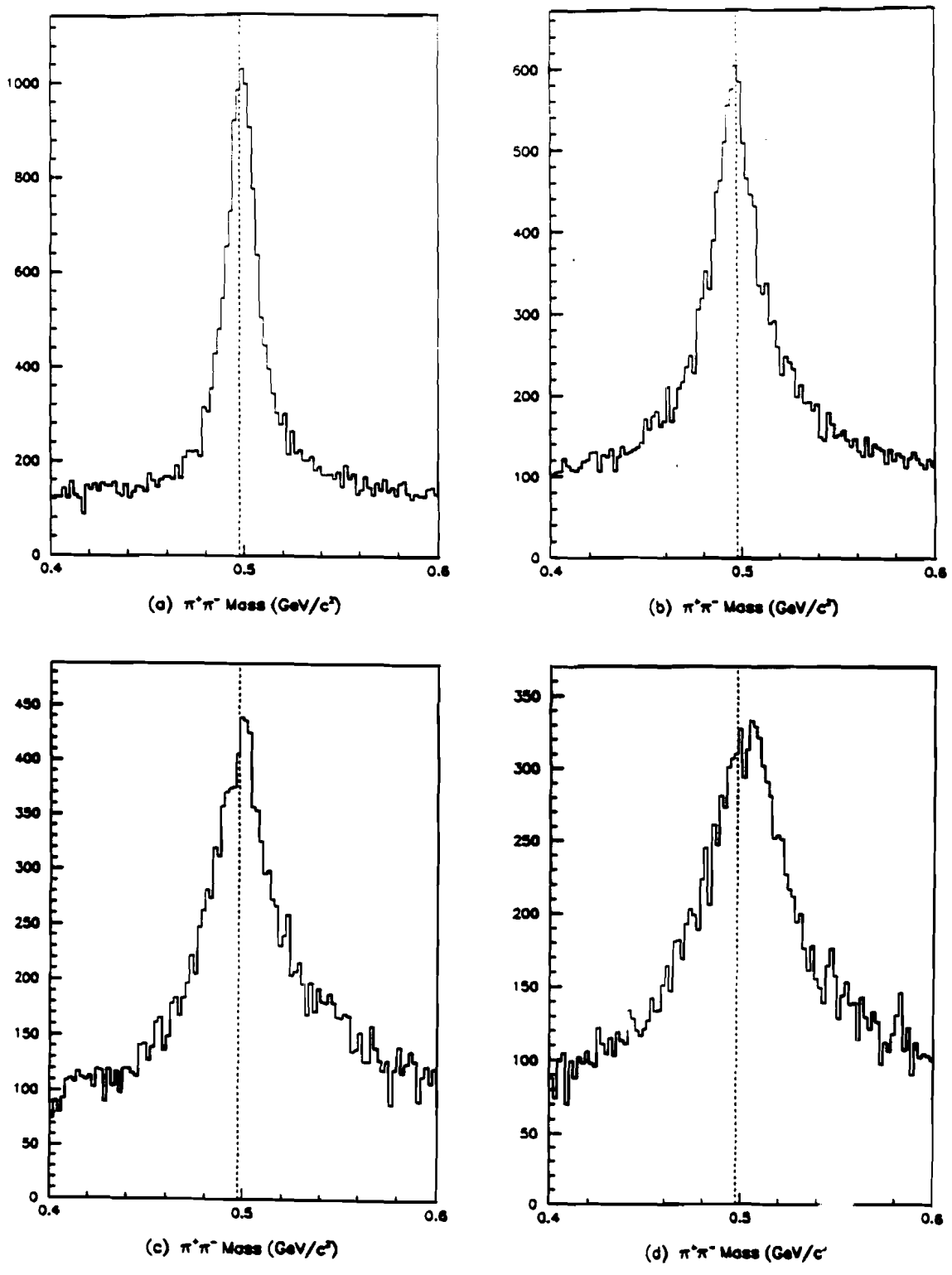

Figure 25 – Invariant mass distribution for K^0_s in four different regions of Z-decay point. (a) 90 cm $\leq$ Z $<$ 115 cm, (b) 115 cm $\leq$ Z $<$ 140 cm, (c) 140 cm $\leq$ Z $<$ 165 cm and (d) 165 cm $\leq$ Z $<$ 190 cm.

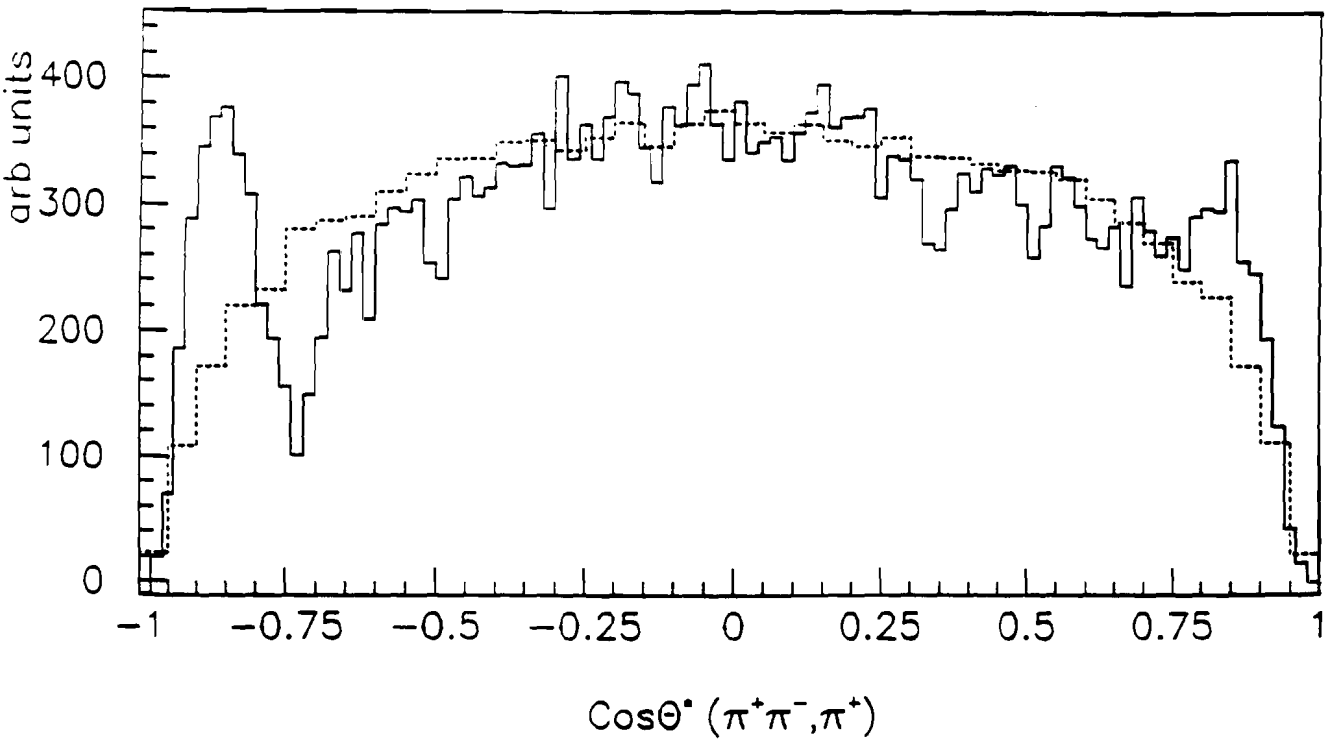

Figure 26 – $\cos\theta^*$ distribution for K^0_s decays with Λ and $\overline{\Lambda}$ peaks.

In Fig. 26, we show the sideband subtracted distributions of the cosine of the decay angle θ between the V^0 direction in the lab frame and the direction of the positive particle from the decay in the V^0 rest frame for the unambiguous K^0_s, Λ and $\overline{\Lambda}$ decays. The solid line corresponds to the distribution without the removal of track pairs satisfying Λ or $\overline{\Lambda}$ mass hypotheses and dashed line corresponds to the with the removal. It's obvious from the figure that peaks at $|\cos\theta^*_K|$ less than 0.8 belong to the Λ's, the left being associated with Λ and right one associated with $\overline{\Lambda}$.

<u>Λ's Identification</u>

Λ baryons can be easily identified from K^0 due to their longer lifetime and the unequal masses of the two particles in their decay. A clear separation of Λ

and $\overline{\Lambda}$ can be made using the charge of the higher momentum decay particle. Kinematics indicate that the proton (anti-proton) carry most of the momentum in the lab frame for a Λ ($\overline{\Lambda}$) particle greater than 300 MeV/c, allowing us to make a unique $p\pi^-(\overline{p}\pi^+)$ mass assignment to the two tracks.[37]

Figures 27(a) and (b) show the $p\pi^-$ and $\overline{p}\pi^+$ invariant mass distribution in the mass range of 1.055 and 1.175 GeV/c^2 when one daughter track was taken as proton (antiproton) and other as a pion. Both the plots show a very clear signal for Λ's under the nominal mass peak. The Λ signal was taken from the mass interval 1.0956 to 1.1356 GeV/c^2 while the background shape was calculated from the mass intervals 1.0656 to 1.0856 GeV/c^2 and 1.1456 to 1.1656 GeV/c^2. As followed in the case of kaons, pairs which lie under the sideband region are used to estimate the contribution from this background and are subtracted from all the Λ's physics distributions. There are about 10087 $p\pi^-$ pairs under the signal region and 3424 pairs under the side band region yielding a background subtracted signal of 6663 ± 132. And for $\overline{\Lambda}$, there are 3177 $\overline{p}\pi^+$ pairs in the signal region giving a background subtracted signal of 1724 ± 55 pairs with a side band of 1453 pairs.

The $\cos\theta^*$ distributions for Λ and $\overline{\Lambda}$ particles are plotted in Figures 28(a) and 13(b) respectively. The distributions are asymmetric with a dip at $\cos\theta^* \simeq 0.1$ where most of the Λ's particles are ambiguous with K^0_s mesons.

p_T and Z-window cut

As mentioned earlier, a lower p_T cut of 0.4 is consistent with our jet alg thm and therefore, we decided to apply this cut on Λ's selection also.

For Z window cut, we used the same method as in case of kaons. In g.

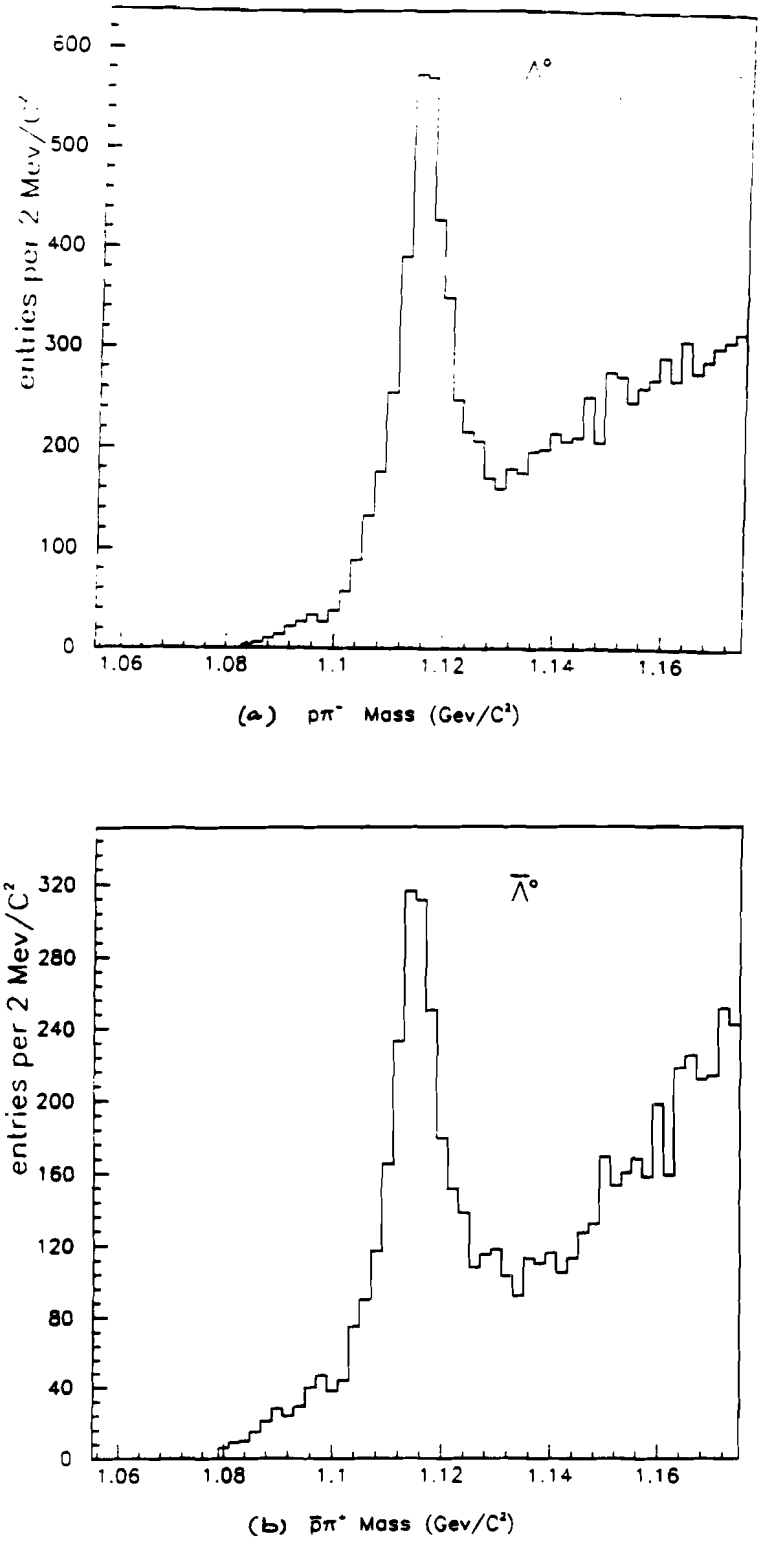

Figure 27 – Invariant mass distributions: (a) Λ and (b) $\overline{\Lambda}$.

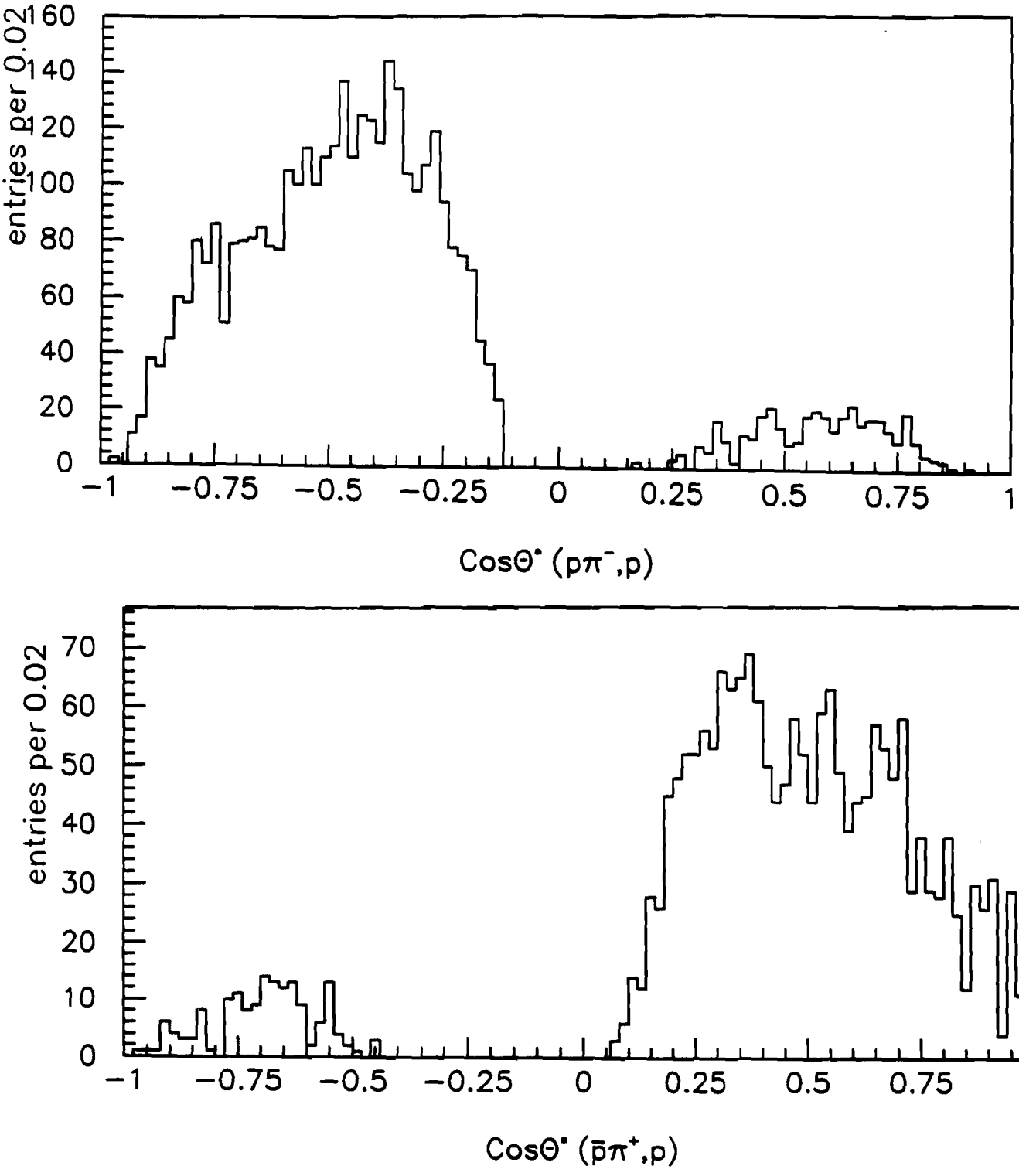

Figure 28 – $\cos\theta^*$ distributions: (a) Λ° and (b) $\overline{\Lambda^\circ}$.

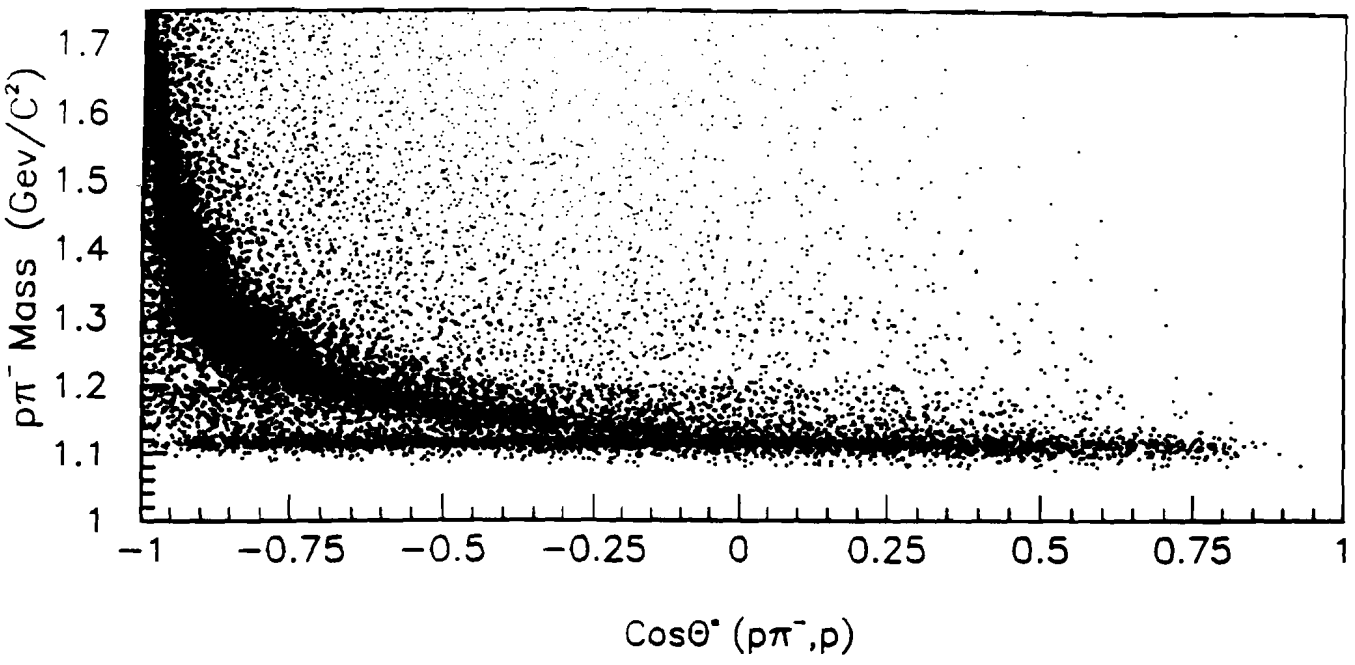

Figure 29 – Λ° mass versus Z location of the decay point distribution.

29, Λ mass is plotted against Z decay point of Λ. The Λ° were selected from the signal region, the width of whose is defined earlier. The horizontal band along the nominal mass of Λ° does not appear to be lost in the background after $Z = 140$ cm. Because of their longer lifetime, the Λ's decay further inside the magnet and are thus easier to reconstruct than kaons. Therefore we decided to keep the same Z window cut on Λs and $\overline{\Lambda}$s.

4.6 Acceptance and Reconstruction Efficiencies

Strange particles can be identified by their lifetime measurements. And to measure lifetime one needs to know acceptance as well as reconstruction efficiencies. The efficiency for finding K^0_s's is affected by the inefficiencies in the track reconstruction algorithm and the vertex finding algorithm, as well as by

subsequent selection criteria. Also, confusion due to hits from unrelated tracks may cause K°_{s} daughter tracks to be misreconstructed such that the decay vertex fit is of unacceptable quality or some cut is not passed.

Various factors contribute to the losses as discussed below. For low momenta losses are mainly due to track finding efficiency and to the cuts imposed on the decay length. For high momenta particles, some V°'s are lost because of the small opening angle, giving rise to large errors on the secondary vertex position. Further losses at high longitudinal momenta are attributed to small production angle i.e. low acceptance.

The acceptance corrections and the detection efficiencies were calculated from a complete parallel analysis similar to Monte Carlo techniques with full tracking detector simulation. This acceptance code was later compared to Monte Carlo simulation with full spectrometer. A bin by bin acceptance correction was done as a function of the x_F and p_T for the jet analysis. Fig. 30 shows the acceptance plot as a function of p_T versus x_F. The long peak indicates 100 % expected efficiency. Since lifetime is a good check on the strange particles under study and lifetime is a function of decay point also beside momentum dependence, a third parameter, Z location of the decay point, was added in the acceptance correction for lifetime calculation.

The acceptance correction for lifetime measurement is a function of x_F, p_T and Z decay point of the strange particle. Once the strange particles were identified by their lifetime measurements, the acceptance corrections were calculated for the jet physics using lifetime of the strange particles.

In this acceptance code, strange particles were produced randomly at the

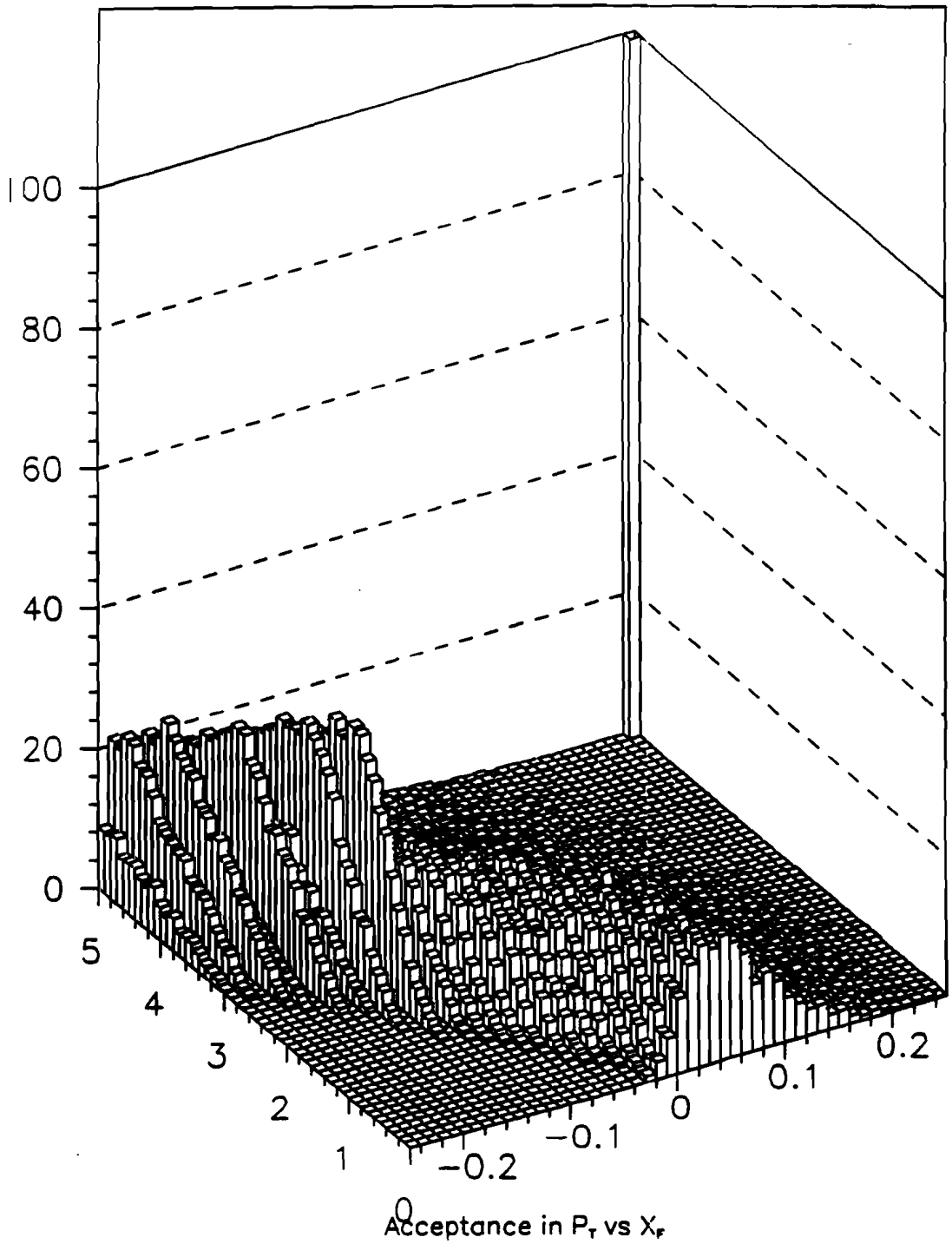

Figure 30 – Acceptance plot as a function of Feynman-x (x_F) and p_T.

target and were allowed to decay inside the Z window similar to the data. The production angular distribution for the decayed particles was assumed to be isotropic. The decayed particles from the simulated events were subjected to all reconstruction cuts which were applied to the data. The reconstruction cuts include relative p_T asymmetry cut, PWC acceptance, ZMP cut, impact parameter cut as well as Z window cut. The resulting acceptance was used to calculate the lifetime of the strange particles. After obtaining the lifetime consistent with the world average value, acceptance corrections were obtained for the jet physics using the world average lifetime value.

To check the reliability of this acceptance code, full Monte Carlo studies were done using GEANT3[36] package. It turned out that we needed around $10-15\,\%$ more corrections were needed due to other losses which could not be reproduced in the above acceptance code. The strange particle mass resolution is dominated by the resolution in the opening angle, which is mainly dominated by the accuracy in measurement of Z location of the decay point.

Around 4900 events were generated using Pythia as event generator out of which 460 events had K^0_s which decayed into $\pi^+\pi^-$ inside our Z window cut. The reconstructor was able to recover 315 K^0_s in the signal region and 51 K^0_s fell in the sideband region and the rest were lost. The momentum difference between the generated and the reconstructed momentum is plotted in Fig. 31. A peak is obtained at the zero position indicating the reliability of the reconstructor in calculating the momentum. There were some scattered entries away from the zero position where either reconstructor failed to reconstruct one of the right decayed track or lost both of the right decayed tracks and thus failed to reconstruct

the right momentum of K_s°.

Since momentum has a direct relation with the Z location of the decay point, difference in generated Z decay point and reconstructed Z decay point is plotted in Fig. 32. It is obvious from the figure that the reconstructor failed to reconstruct the right momentum causing an error on the Z-coordinate of decay position. To see this Z-smearing, we changed our Z window by 10 cm on the both side and were able to recover 13 % more K_s°. And Z location of the decay point has a direct relation with the opening angle of the decayed neutral particle. A low opening angle is more likely to cause Z-smearing than a high opening angle. This is shown in Fig. 33, where delta Z (difference in Generated Z location and Reconstructed Z location) is plotted against opening angle of the neutral particle.

4.7 Final Selection Cuts on K_s° or Λ° or $\overline{\Lambda^\circ}$

In the $\cos\theta^*$ plots of K_s° or Λ and $\overline{\Lambda}$, the pairs which satisfied more than one mass hypothesis were removed which resulted in the loss of statistics. To resolve the ambiguities between K_s°/Λ or $K_s^\circ/\overline{\Lambda}$, $\cos\theta^*$ variable was used to identify the strange particles.

K_s° selection

In Fig. 34, K_s° mass versus $\cos\theta_K^*$ for the data is plotted. The $\cos\theta^*$ variable extends from -1 to $+1$. Three clear bands are visible. The one horizontal band at the center peaks at the nominal mass of K_s°. The other two bands at the high value of $\cos\theta^*$ are due to the Λ and $\overline{\Lambda}$ which appear as fake K_s° in the plot. Therefore if we put a cut of $|\cos\theta_K^*| \leq 0.8$, we can obtain a clean sample of K_s^*

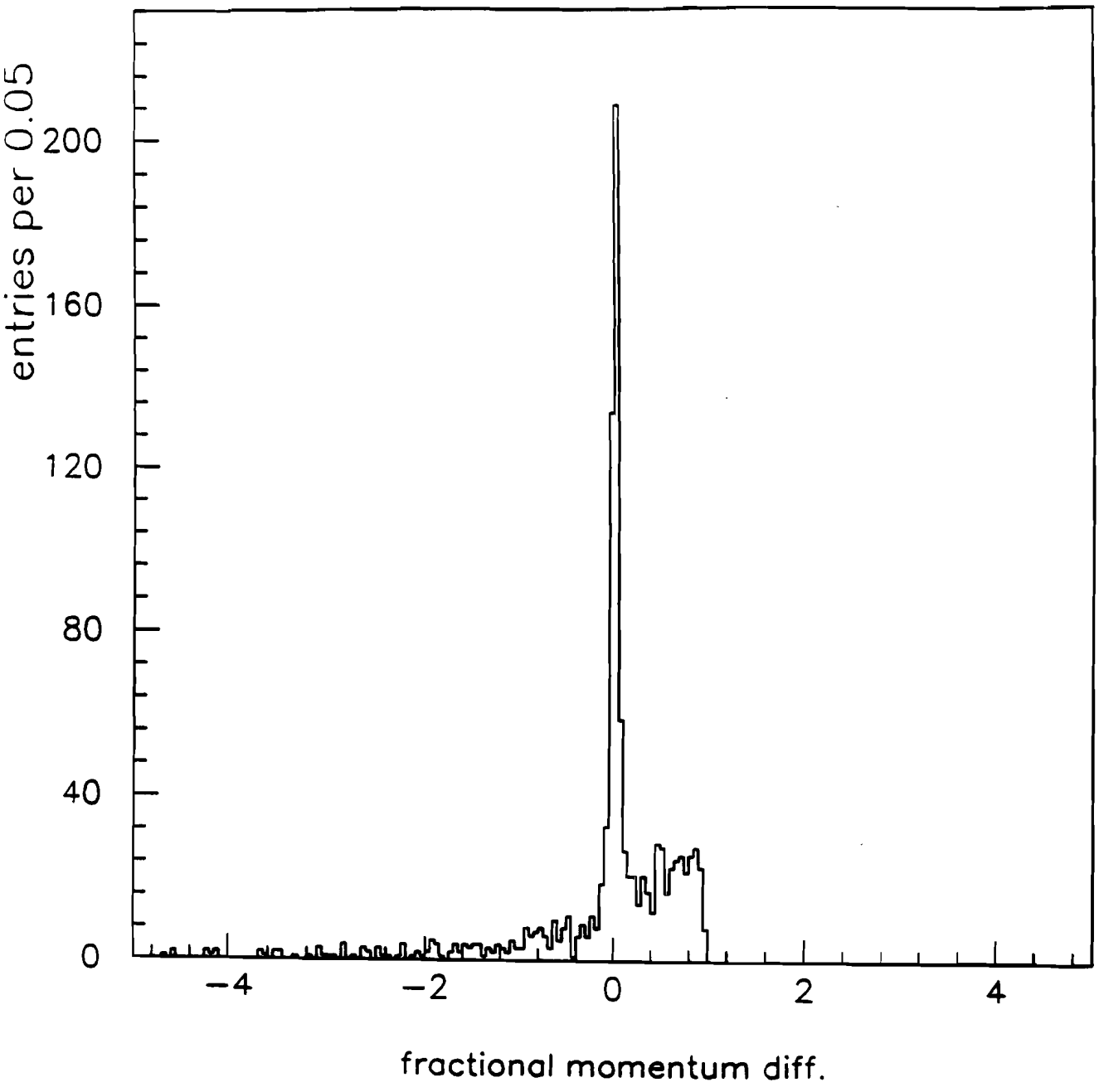

Figure 31 – Distribution of (Generated Mom. – Reconstructed Mom.)/Generated Mom.

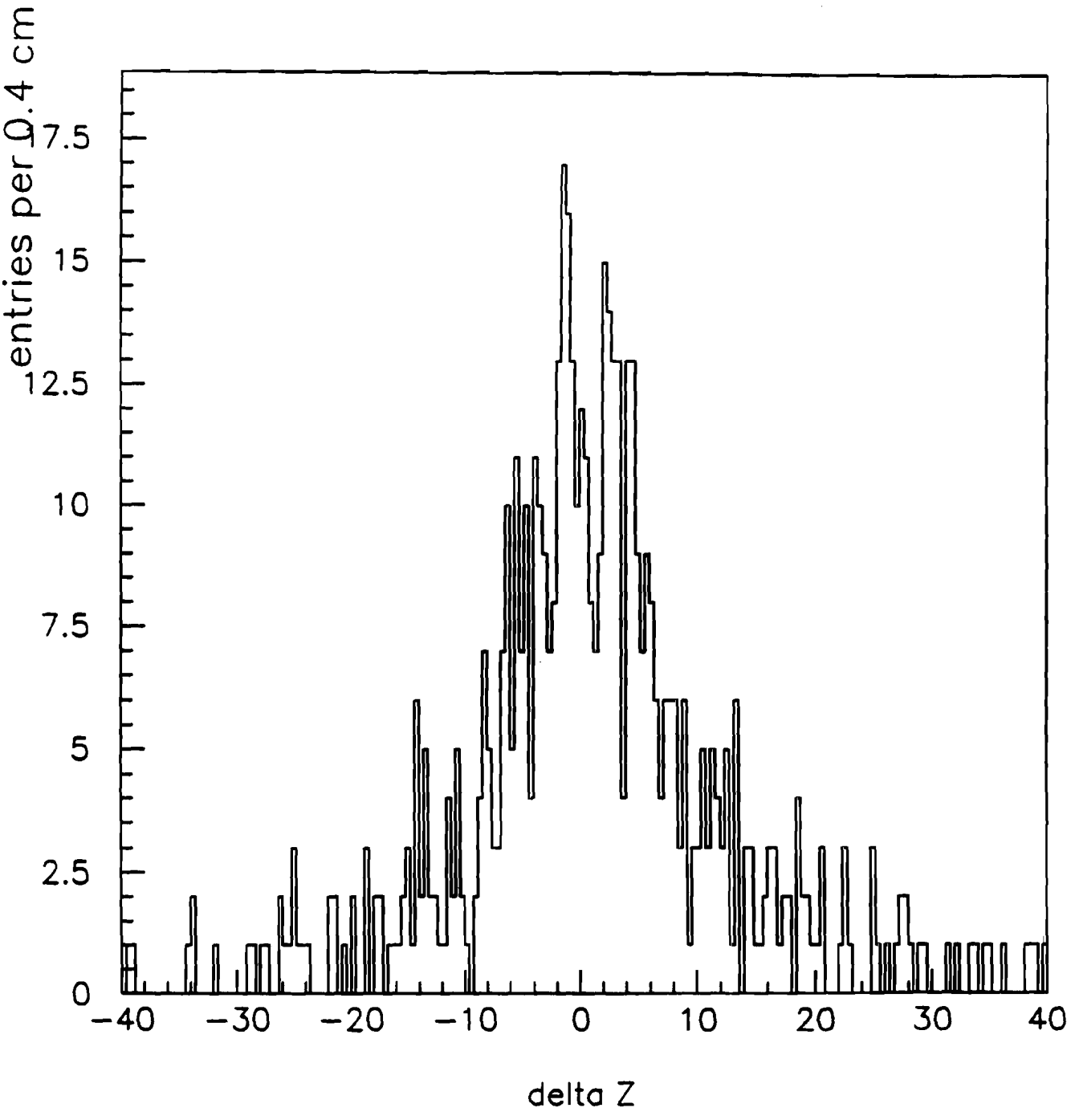

Figure 32 – Difference in Reconstructed Z decay point and Generated Z decay point.

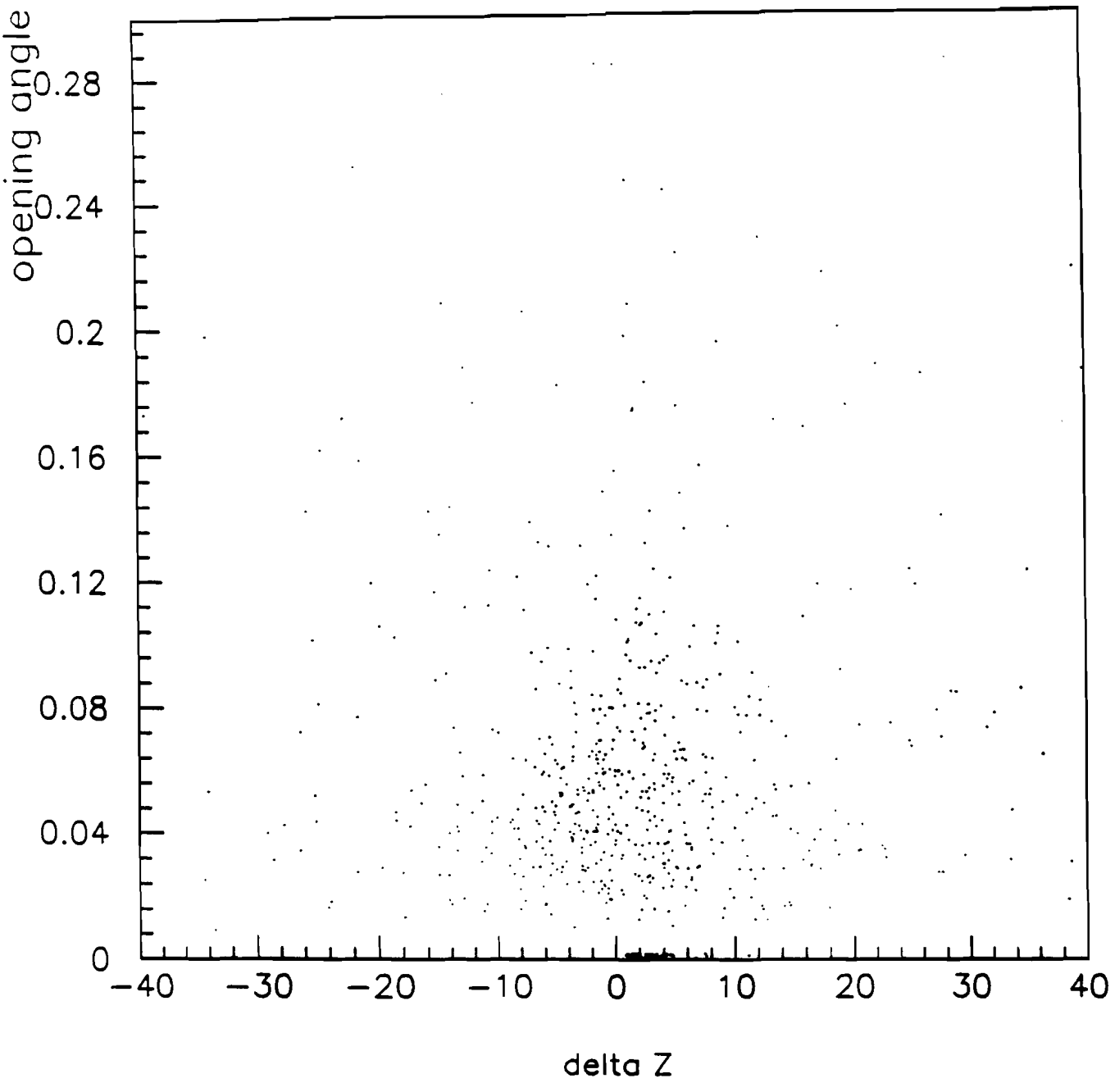

Figure 33 – Distribution of delta Z versus opening angle of the decayed tracks. Delta Z is the difference between Generated Z location and Reconstructed Z location of decay point.

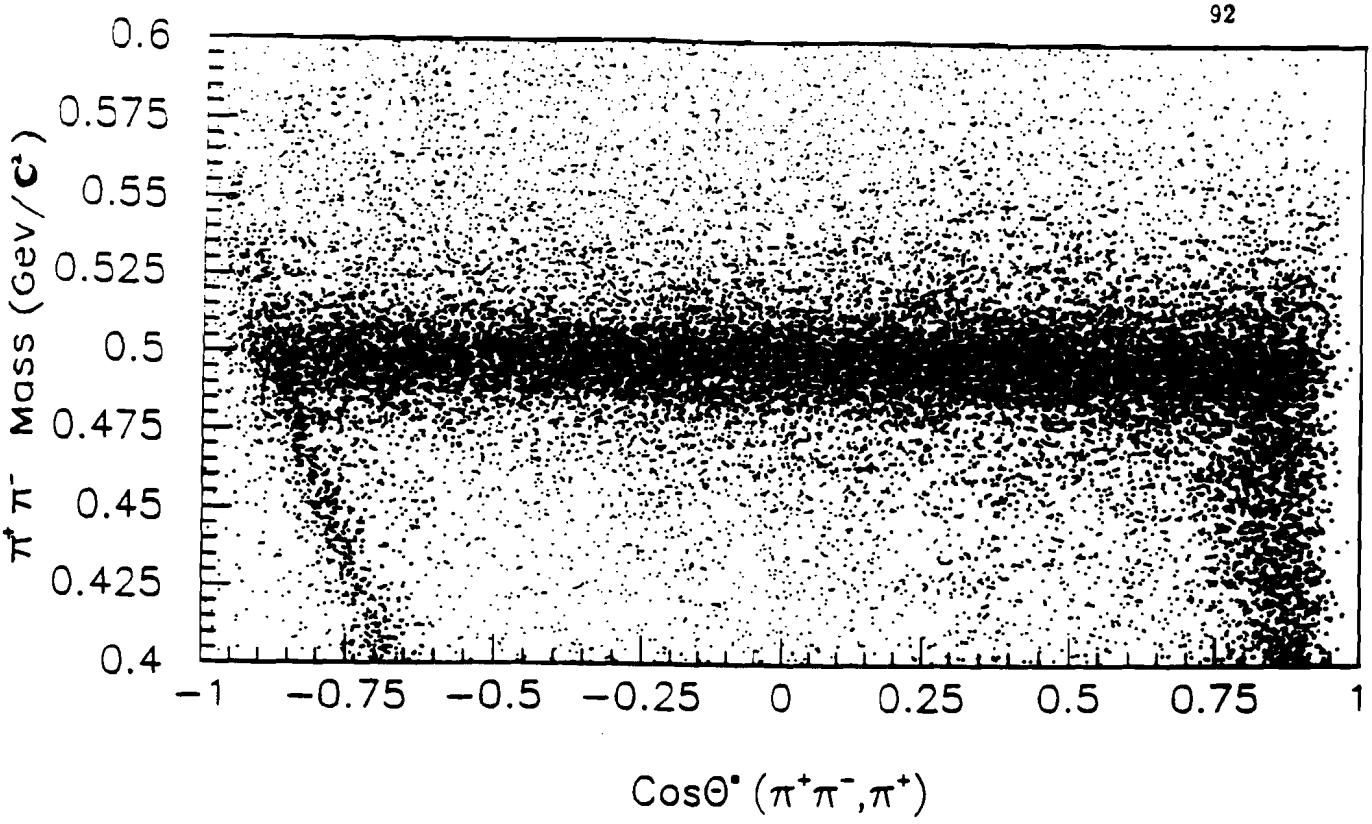

Figure 34 – K^0_s mass versus $\cos\theta^*_K$ distribution.

from the data. An invariant mass distribution of track pairs assuming $\pi^+\pi^-$ is shown in Fig. 35 after imposing a p_T cut, Z window cut on decay point and $\cos\theta^*$ cut. This sample was used in the jet physics without any more cut on the data sample.

Λ° selection

In Fig. 36, Λ mass versus $\cos\theta^*_\Lambda$ for the whole data is plotted. A lower p_T cut of 0.4 has been imposed on the pairs which satisfy Λ mass hypothesis. A horizontal band beginning from the negative side of the $\cos\theta^*$ scale and appearing at the nominal mass of Λ represents the Λ data. And the other band which begins from the high $\cos\theta^*$ value represent K° which shows up as fake Λ in the Λ data sample. These two bands appear to be beginning to merge at $\cos\theta^* =$

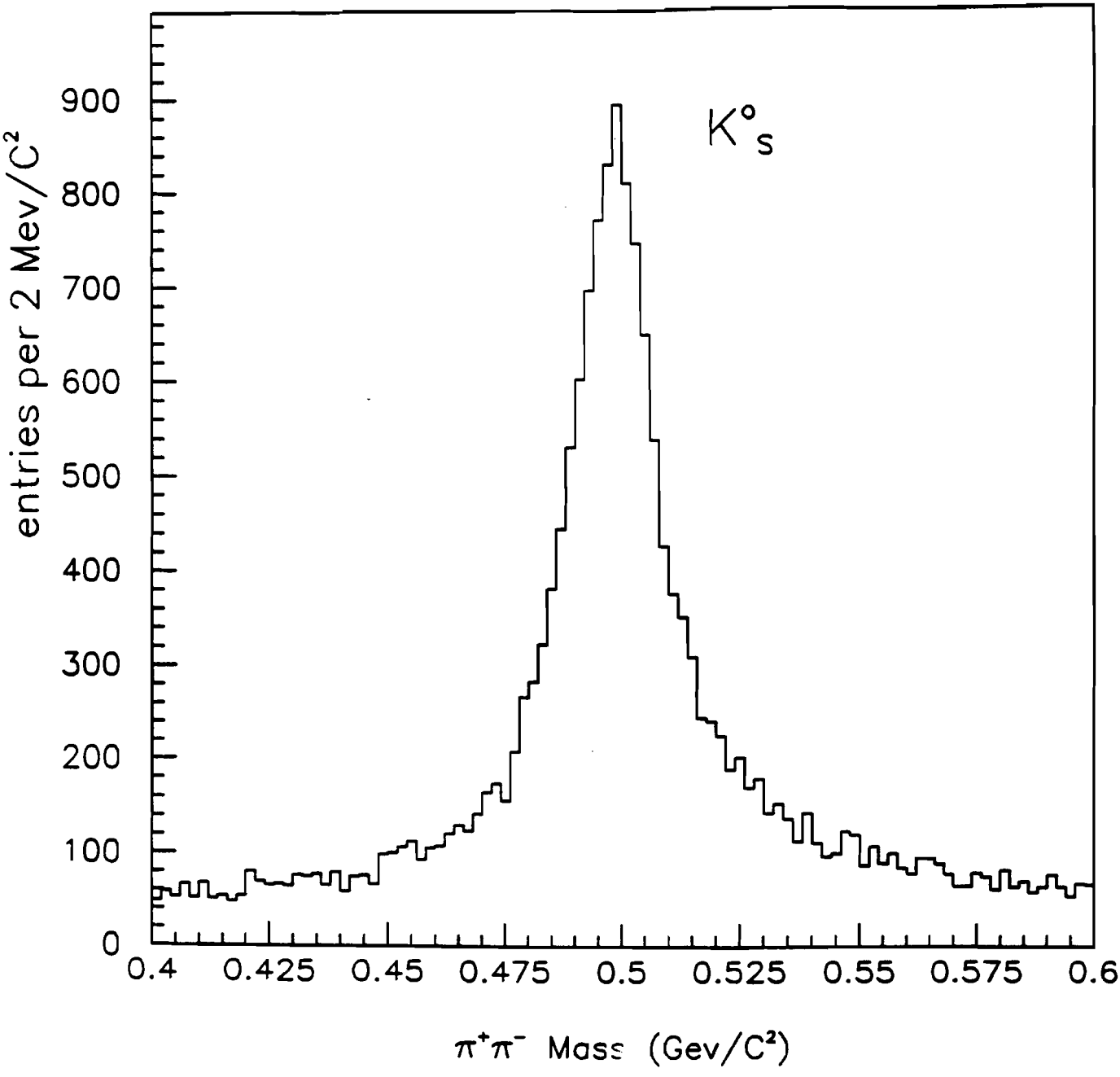

Figure 35 – Inavariant mass distribution for $\pi^+\pi^-$ after satisfying p_T, Z window and $\cos\theta^*$ cut.

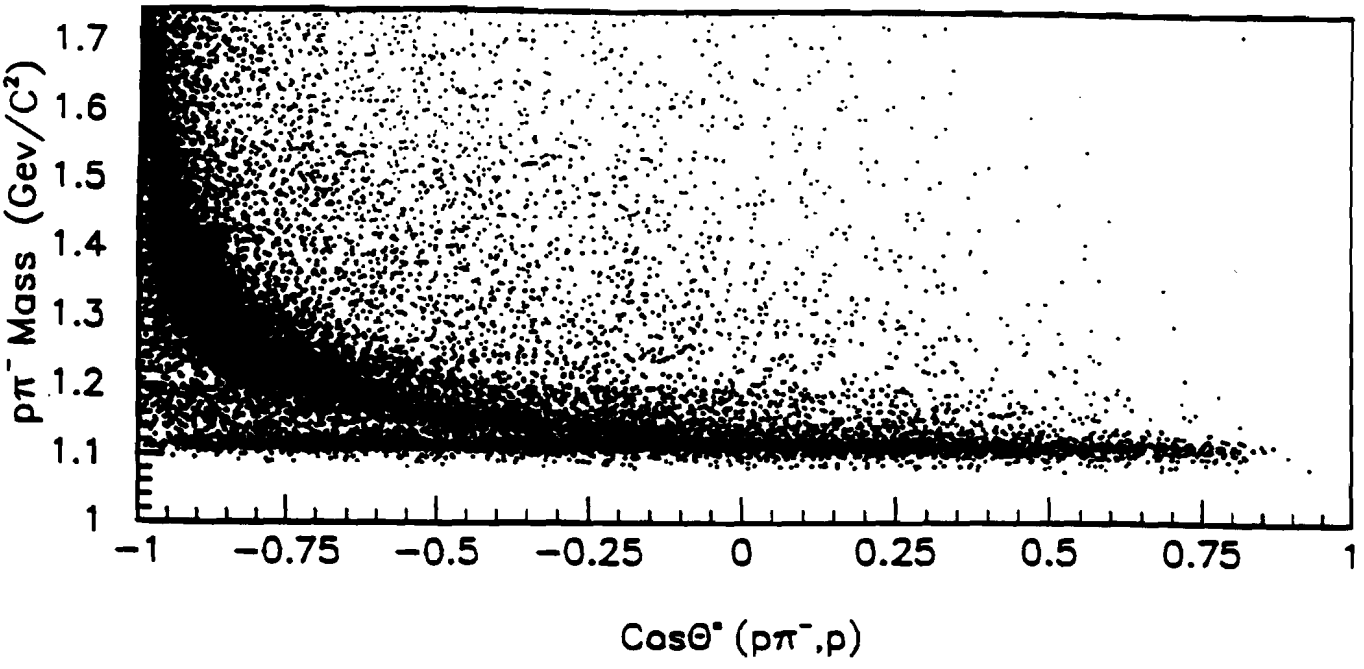

Figure 36 – Λ° mass versus $\cos\theta^*_\Lambda$ distribution.

–0.2 and becomes inseparable after –0.2 in this plot. Therefore, an upper cut of –0.2 on $\cos\theta^*_\Lambda$ should provide a clean sample of Λ. In Fig. 37, invariant mass distribution of $p\pi^-$ is plotted where a narrow peak appears at the nominal mass of Λ. The pair has been constrained to p_T (> 0.4 GeV/c) cut, $\cos\theta^*_\Lambda(\leq -0.2)$ cut and the Z decay point was taken from 90.0 to 190.0.

$\overline{\Lambda}$ selection

The same type of procedure was adopted for the $\overline{\Lambda}$ selection as in Λ selection. $\overline{\Lambda}$ mass versus $\cos\theta^*_{\overline{\Lambda}}$ for the data is plotted in the Fig. 38. Again a p_T cut of 0.4 i.e., $p_T > 0.4$ GeV/c has been imposed on the pairs which satisfy $\overline{\Lambda}$ mass hypothesis. The horizontal band which begins from the positive side of $\cos\theta^*$ due to the kinematical reasons, represent $\overline{\Lambda}$ sample. The other curved shape

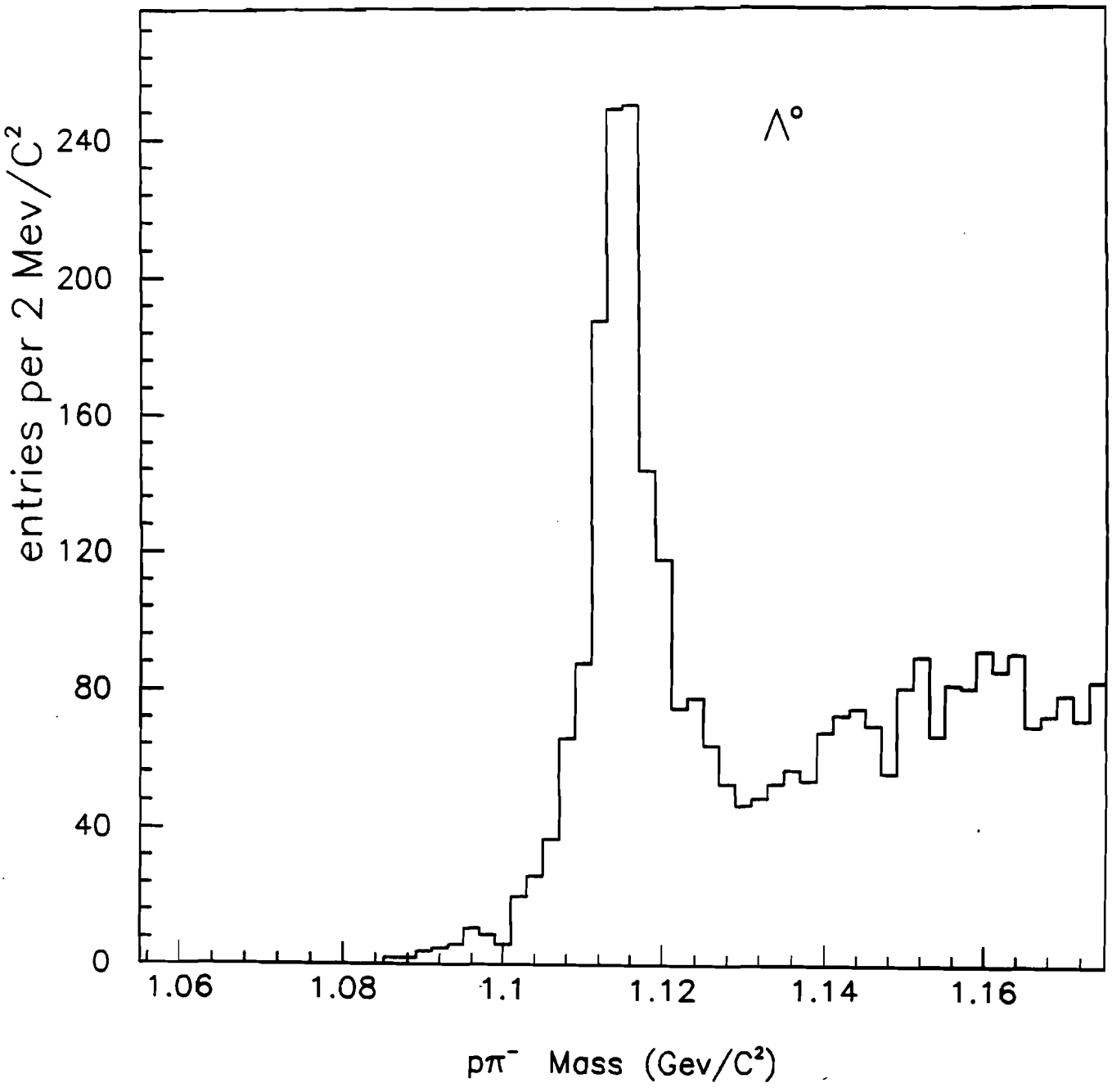

Figure 37 – Inavariant mass distribution for $p\pi^-$ after satisfying p_T, Z window and $\cos\theta^*$ cut.

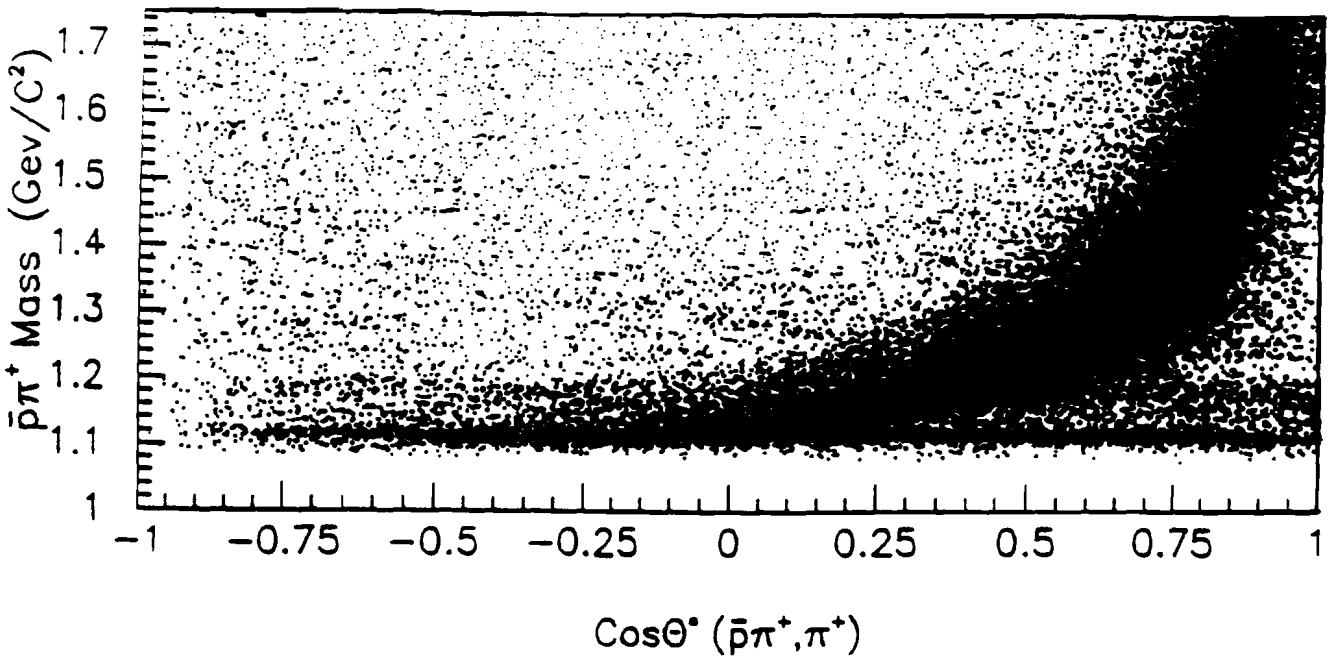

Figure 38 – $\overline{\Lambda}$ mass versus $\cos\theta^*_{\Lambda}$ distribution.

band represents K^0_s which appear as fake $\overline{\Lambda}$ in the plot. The two bands begins to merge at $\cos\theta^* = 0.2$ and become indistinguishable with decreasing $\cos\theta^*$. Therefore, if a lower cut of 0.2 on $\cos\theta^*_{\Lambda}$, unlike in Λ selection, should provide a clean sample of $\overline{\Lambda}$. Invariant mass distribution of $\bar{p}\pi^+$ is plotted in Fig. 39 where a narrow peak appears at the nominal mass of $\overline{\Lambda}$. The pair has been subjected to p_T (> 0.4) cut, $\cos\theta^*_{\Lambda}(\leq 0.2)$ cut and the Z decay point was taken from 90.0 to 190.0.

4.8 Lifetime distribution

To verify the efficiency calculations, we have plotted an acceptance - corrected - background - subtracted lifetime distribution of K^0_s and Λ in Figures 40(a) and (b) respectively. The fitted slope in Fig. 24(a) of the distribution is

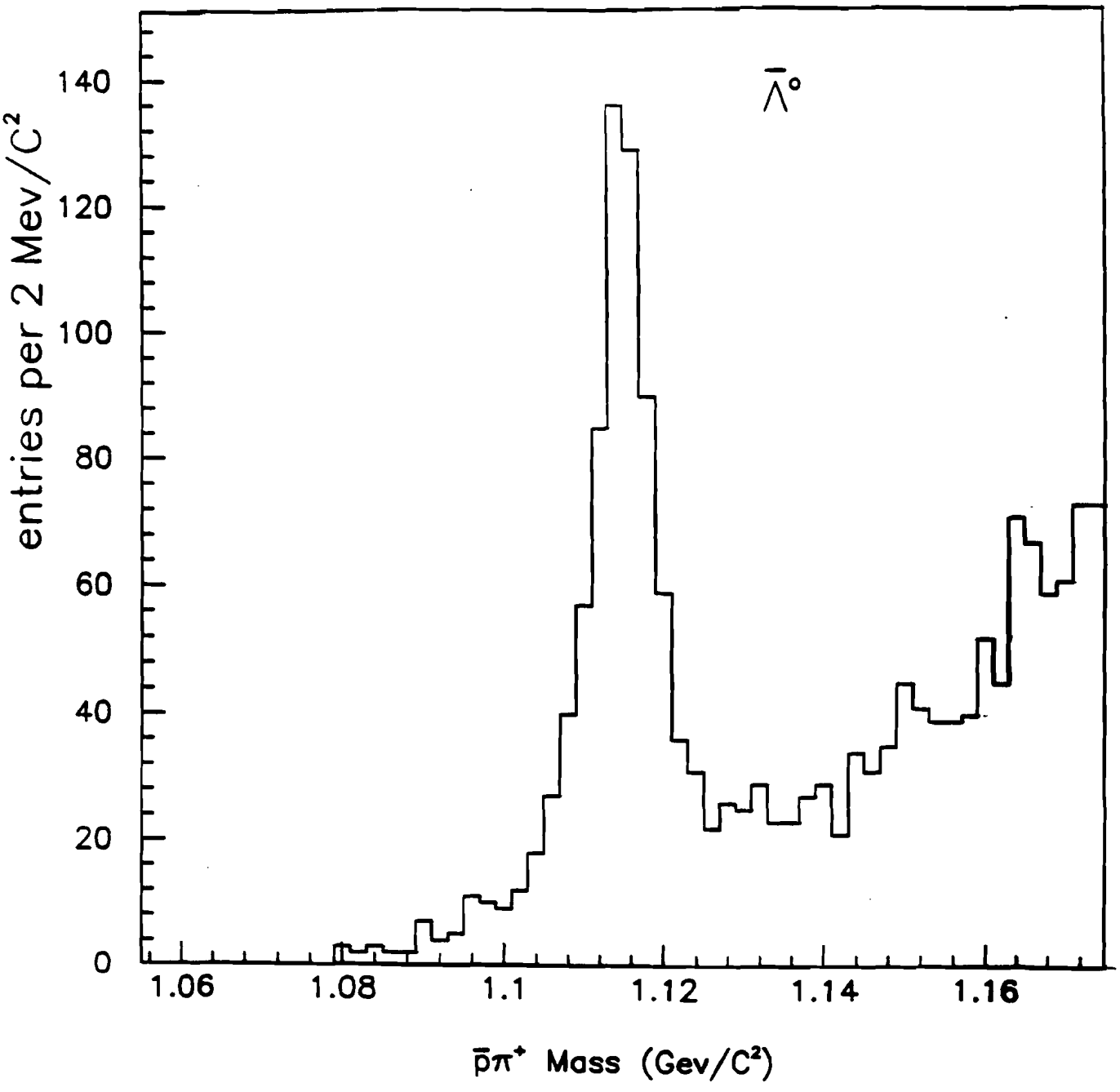

Figure 39 – Invariant mass distribution for $\bar{p}\pi^+$ after satis. ng p_T, Z window and $\cos\theta^*$ cut.

-1.09 ± 0.03, consistent with the expected value of -1. The χ^2 value is 0.855 per degree of freedom. It is clear that for $|\cos\theta^*_K| \leq 0.8$ the lifetime probability strongly favors the kaon hypothesis. Fig. 24(b) represents the lifetime distribution for combined data set of Λ and $\overline{\Lambda}$. The value of the fitted slope is -1.12 ± 0.05 against the expected value of -1 and the χ^2 value is 1.182 per degree of freedom.

Thus it is seen that the various corrections and cuts applied on the data lead to results which are consistent with the world data.

Hence, the procedure followed for selection of the events of interest for data analysis is justified.

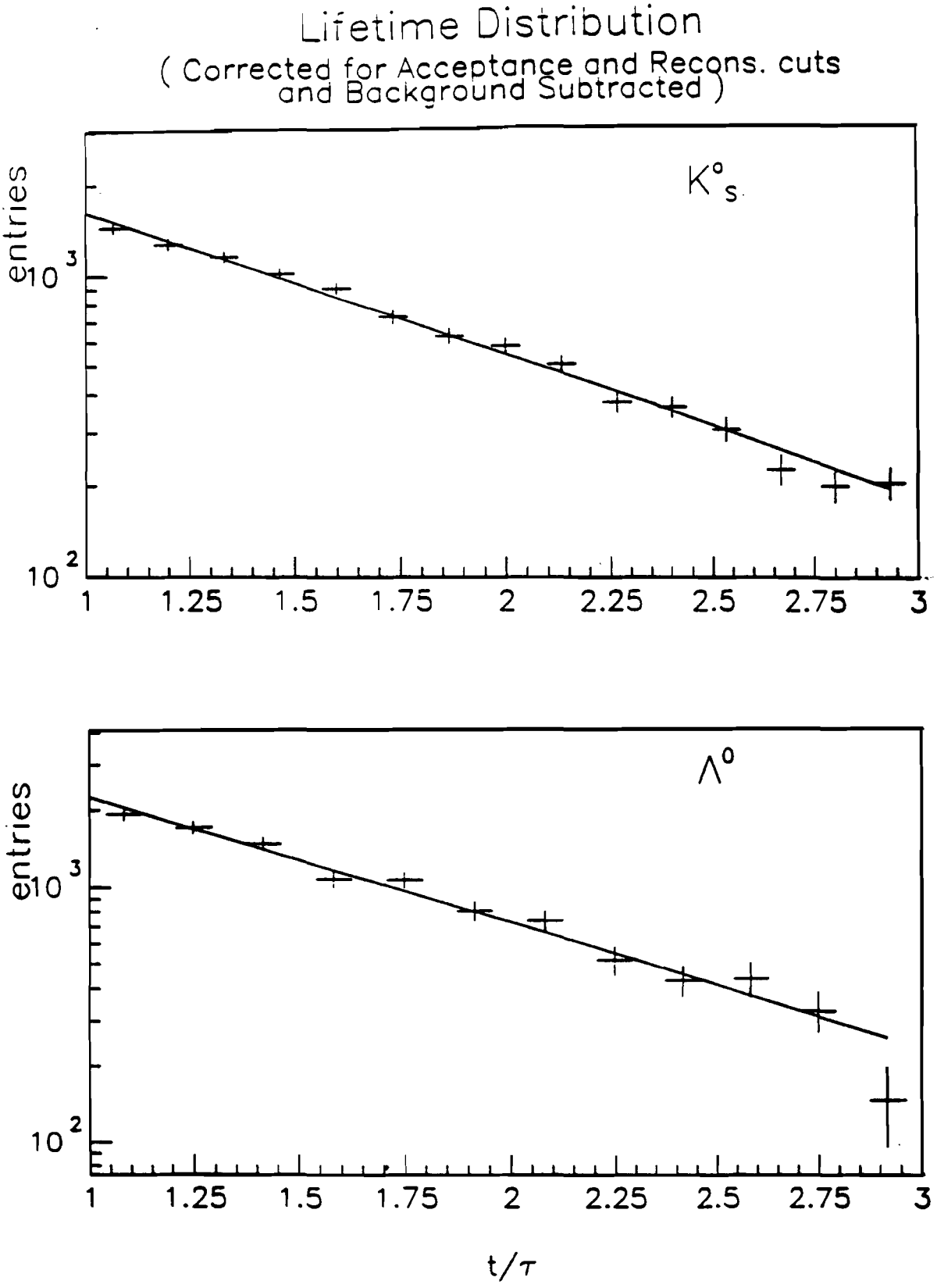

Figure 40 – Lifetime distribution corrected for Acceptance and Reconstruction cuts and background subtracted for (a) K°_s (b) $(\Lambda^\circ + \overline{\Lambda^\circ})$. τ is the proper lifetime.

5. Jet Reconstruction

This chapter describes the cuts imposed to select events which were triggered by a high p_T π° and the procedure to examine these events for jet structure on the away side. Since jets are going to play an important role in the following discussion, the concept of a jet is given here[39].

- A jet is the *hadronic debris* which is generated when a q, $\bar{q}$ or g finds itself *isolated* in momentum space and therefore tending to become isolated in configuration space.
- A jet is a collimated *spray* of hadrons.
- A jet is the "footprint" of a parton.

Experimentally, jets are defined in the following way. In a high energy collision, particles are typically produced with small transverse momenta with respect to the beam characterized by a scale of order 300 MeV/c. Therefore, one can isolate jets produced with large p_T by focussing on those particles with large p_T and by using some "jet algorithm" to reconstruct the jet from which these particles originated.

In chapter 4, a procedure was defined to select events containing strange particles from the complete data set in which the strange particles were tagged. In this chapter, another selection criteria was imposed on the events to be accepted for jet analysis. This selection criteria uses a set of cuts to determine that the triggering particle was a π°.

5.1 Event Selection

Those events which survived the following cuts were considered for the jet analysis. These cuts are designed to minimize the sources of the background to π° triggered events. The major contribution to the background under the π° signal is from beam halo muons that radiated in the LAC and photons from the decays of the η°. These showers when combined with some other shower in the LAC can accidentally reconstruct a mass in the π° region. Similarly, the direct photon events can cause misreconstruction of π° particle, albeit at a much smaller level. Cuts were imposed on showers, tracks and then on π° trigger selection.

Preselection of the events

At the higher level, for the preselection of the events to be considered for the jet analysis, events were required to meet the following conditions. These conditions were designed mainly to improve the quality of the signal.

1. Since at high p_T, signature for jet structure becomes more clear, a lower p_T cut of 3 GeV/c was imposed on the one photon shower or a diphoton shower (sum of two photon showers). The trigger threshold was varying during the course of the run and hence the efficiency at any given value of p_T should be taken into account for cross section measurements. For this study, however, no significant dependence on the trigger p was observed in the range of 3 GeV/c to 5 GeV/c. Therefore, the corr tions due to trigger efficiency have been ignored.

2. The highest p_T reconstructed photon should be in the triggeri octant.

3. In order to avoid events triggered by halo muons, events in which one or both the veto walls registered a hit overlapping with the trigger quadrant were rejected. This cut is in addition to an online veto which was imposed during data acquisition that required neither of the veto walls to fire within ± 60 nsec of the interaction. Further cuts to reject muon induced showers will be discussed later.

Shower Selection

One needs to isolate direct photon showers from the showers due to photons from the π° decays. In order to accomplish that, direct photon must be reconstructed and then make sure that they do not belong to π° decay. The following cuts were made to satisfy the condition that these photons were coming from the vertex region.

1. The detection efficiency of π°'s was significantly lower around the edges of the calorimeter. Therefore a fiducial cut was imposed on the showers to contain them within the fiducial region of the calorimeter.

2. Another source of background is due to stable hadrons that shower inside the LAC. In order to avoid this, showers were required not to match a track within a radius of 1 cm at the face of the calorimeter. In addition, it was required that the ratio of the energy in the front section of the calorimeter to the sum of the energies in the front and the back sections be greater than 0.2.

3. A useful method of removing showers due to halo muons is the directionality cut. Directionality, which is a measure of the photon's trajectory in

the EMLAC, is defined as (ref 33)

$$\delta_r = R_{front} - \frac{Z_{front}}{Z_{back}} R_{back}$$

where:

R_{front} = reconstructed R position of the shower in the front section of the EMLAC

R_{back} = reconstructed R position of the shower in the back section of the EMLAC

Z_{front} = Z coordinate of the shower at the front face of the EMLAC from the target

Z_{back} = Z coordinate of the shower at the back face of the EMLAC from the target

Particles coming from the target will have zero directionality. But if particles come parallel to the beam, they will have non-zero directionality. Therefore in order to remove particles not coming from the target, a requirement of directionality less than 0.4 was imposed on the showers. Fig. 41 illustrates the concept of the directionality (ref 33) where a muon enters the EMLAC parallel to the beam line, and when a photon originates from the target.

π° event selection

As mentioned earlier, the experiment was designed to trigger on high transverse momentum direct photon or diphoton candidate. But for this analysis, only events triggered by a π° candidate with $p_T > 3.0$ GeV/c are used. The data sample was searched for π°'s and a strong signal was obtained. All of

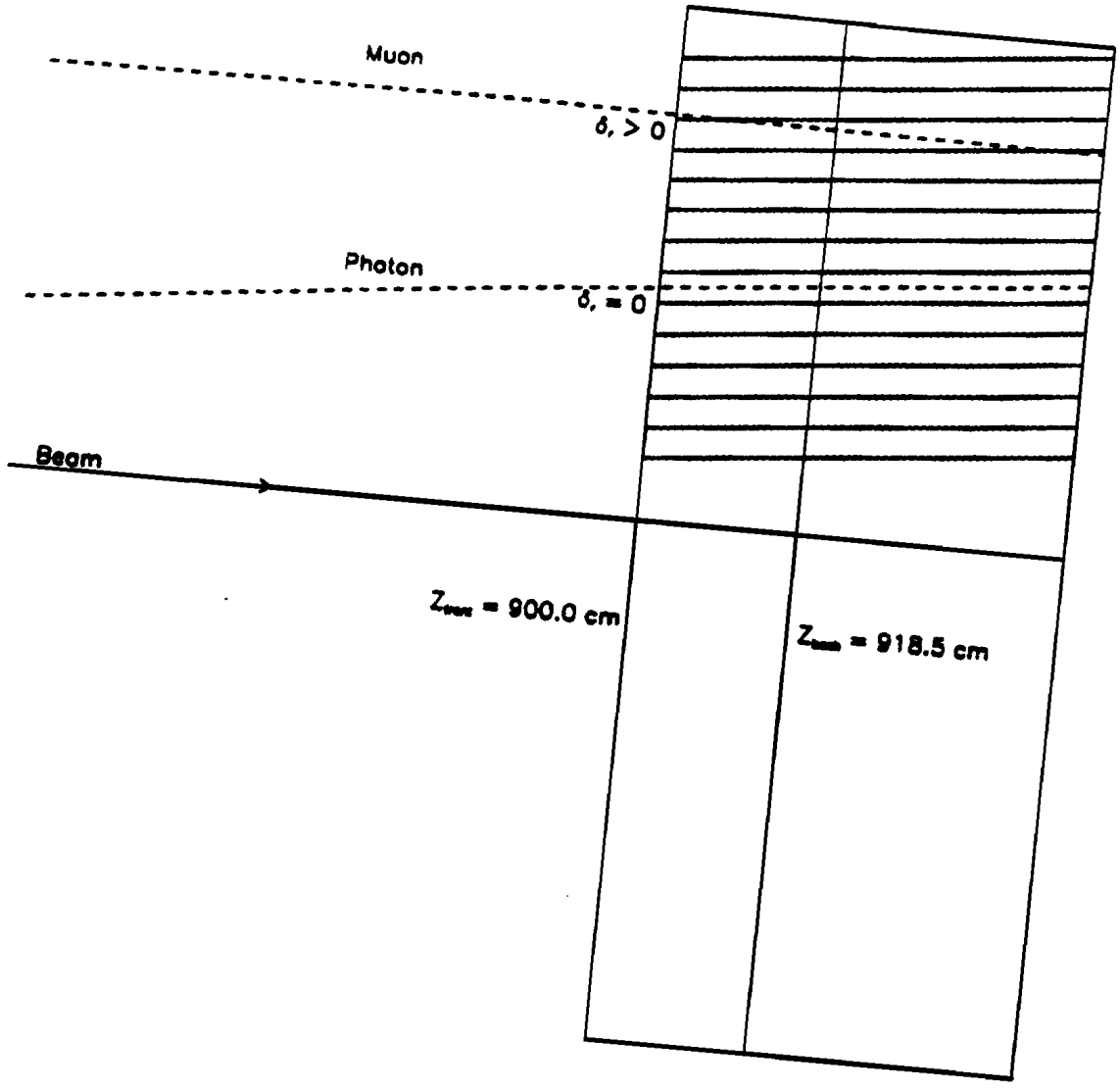

Figure 41 – Illustration of Directionality concept

the pairs of showers from the electromagnetic calorimeter were considered for the π° reconstruction. By measuring the origin of the π° production and the energy and positions of the photons in the EMLAC, the invariant mass for the two photons was obtained. Fig. 42 shows the invariant mass of diphotons with $p_T > 3.0$ GeV/c. If the invariant mass of these pairs falls between 100 and 170 MeV/c^2, it was considered as a π° and if it was between 500 and 600 MeV/c^2, then it was considered as an η°. A detailed description about π° reconstruction and analysis work can be found elsewhere (ref 33). For the jet analysis, π°s had to satisfy the following requirements to be considered as a good π° event.

1. A good π° event requires both the showers to pass the shower selection criteria.

2. The π° had to have a p_T of at least 3.0 GeV/c and it should be the highest p_T neutral object in the event.

3. The other requirement is that the highest p_T π° should be reconstructed from the highest p_T photon in the event.

4. The background to π°'s arises from the combinations of high p_T photon and low p_T photon or misreconstruction of a photon. Therefore, in order to improve the signal to background ratio, an energy asymmetry cut was imposed on the π° sample.

   π°, being a scalar particle, decays with a flat distribution in $|\cos\theta^*|$, where θ^* is the angle between one of the decay photons and the π° direction, in the π° rest frame. For massless decay particles, this definition in the lab

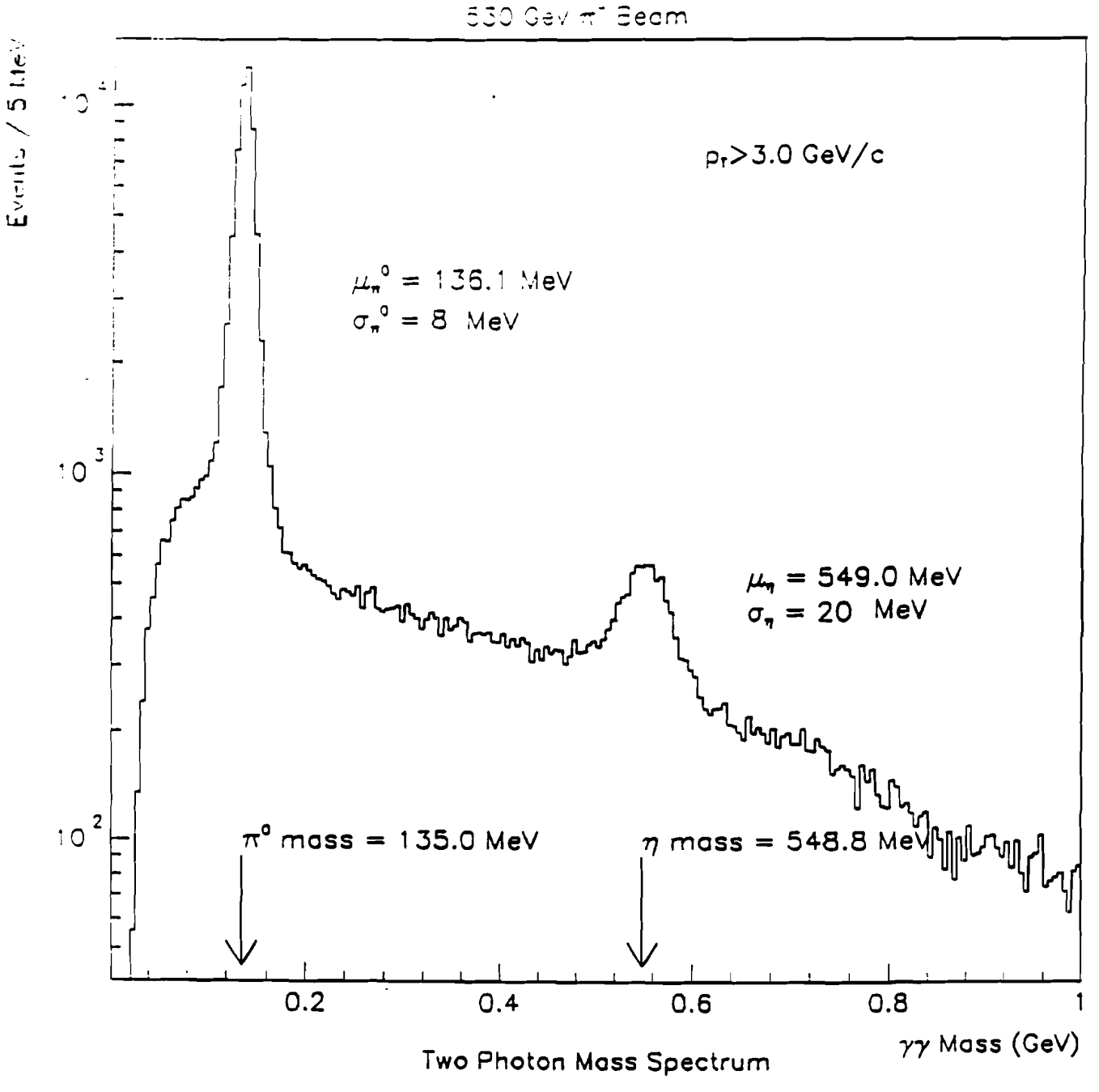

Figure 42 – The invariant mass of di-photons with $p_T > 3.0$ GeV/c.

system is equal to asymmetry A, defined by

$$A = \frac{|E_1 - E_2|}{E_1 + E_2}$$

where E_1 and E_2 are the energies of the decay photons which satisfy the π° mass cut. Fig. 43 shows the asymmetry distribution for the π°s. If a π° decays symmetrically, its asymmetry, A would be zero. In general, one photon from π° decay is occasionally produced with a very low energy and at a large angle relative to the π° direction. By combining this photon with a non-decayed photon would yield a wrong combination. Therefore, the π° events were required a have a higher asymmetry cut of 0.75. The dashed line in the Fig. 44 shows the $\gamma\gamma$ mass distribution with the asymmetry required to be less than 0.75. It is clear that by imposing this cut, the π° mass distribution becomes sharper.

5. A rapidity cut was imposed due to the limitations on the acceptance of the highest p_T shower. Highest p_T π°s with a rapidity range of -0.7 to 0.7 were considered for jet reconstruction.

5.2 Jet Reconstruction Algorithm

The evidence for the jet structure in high p_T interactions has been clearly demonstrated at the highest energy colliders. In fixed target experiments like this one, an additional problem of separating jets arises due to the tendencies of the recoil and beam or target jets to overlap. Also, because these jets have smaller multiplicities, experimental losses can seriously effect the efficiency for finding jets.

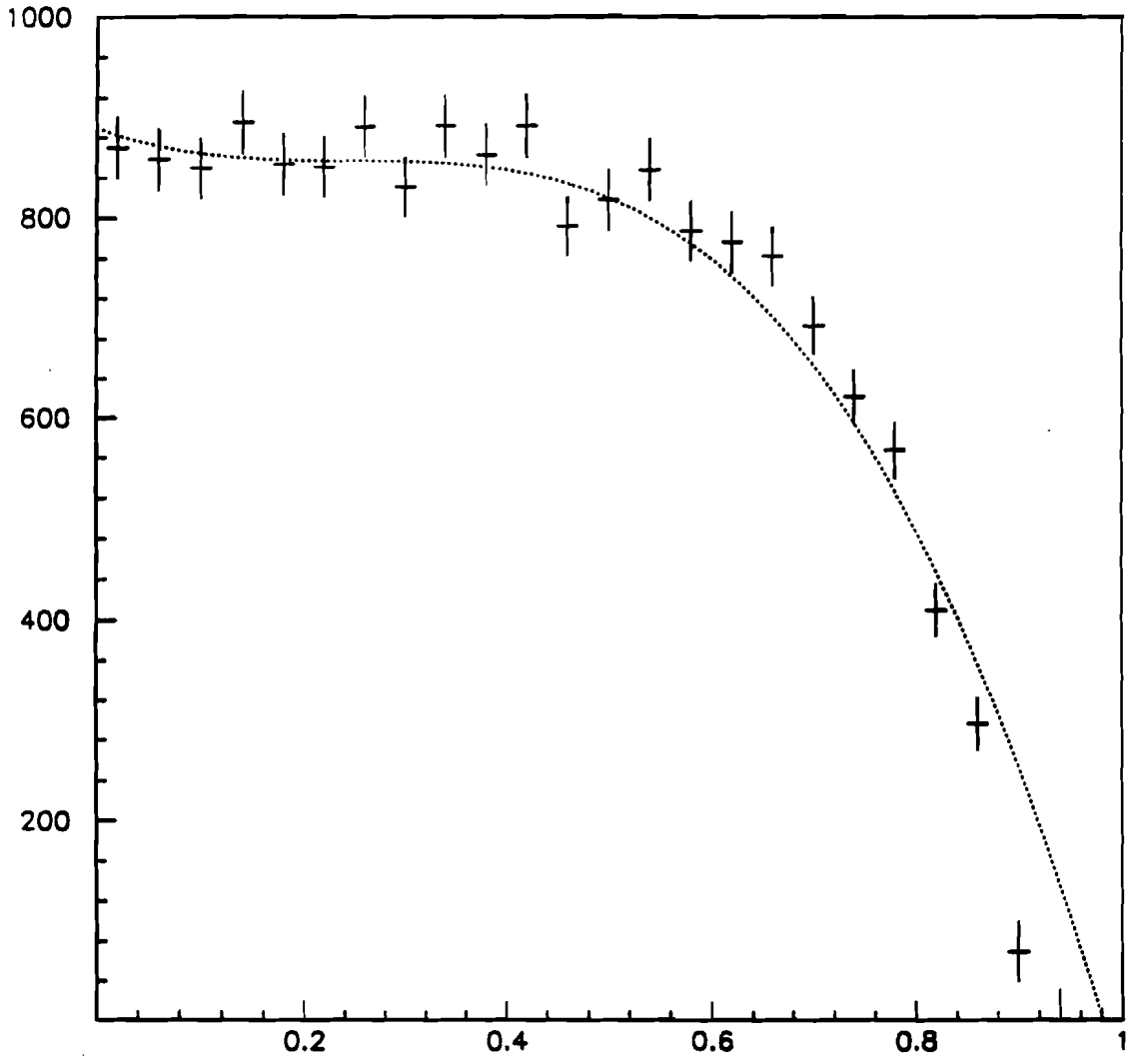

Figure 43 – Asymmetry distribution of π^0s.

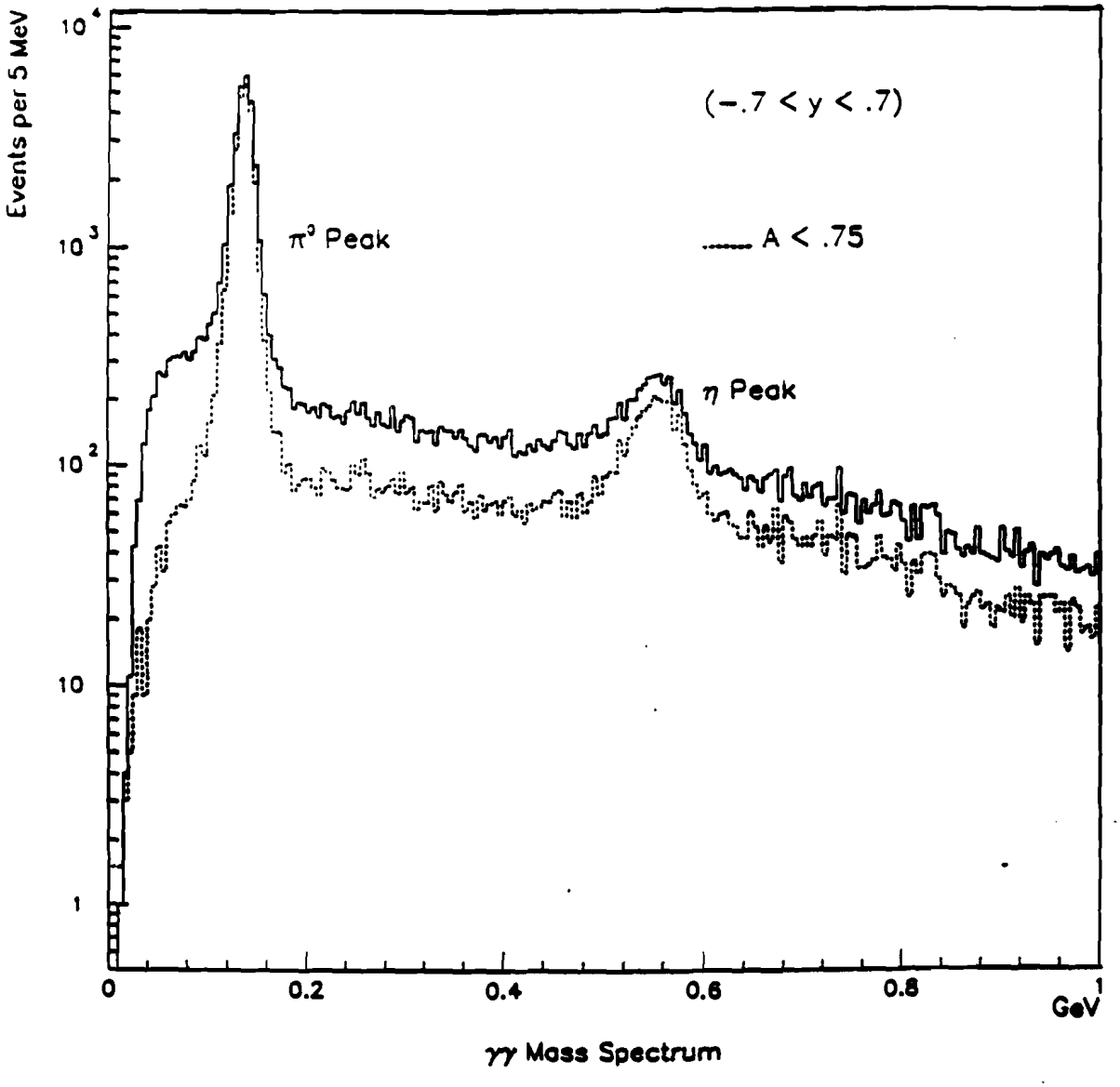

Figure 44 – The invariant mass of di-photons with $p_T > 3.0$ Ge c. The dotted line represents the di-photon mass distr ou-tion with an energy asymmetry cut of 0.75.

The algorithm for the recoil jet reconstruction was motivated by a procedure employed by the WA70 collaboration[40]. This algorithm makes use of the fact that incident beam direction is known and that the fragments of the beam and target jets should have a limited transverse momentum with respect to the beam direction whereas the trigger (or recoil) jet fragments should have limited transverse momentum with respect to the trigger (or recoil) jet axis which will be at a large angle to the beam direction.

The algorithm makes some early assumptions. The first assumption is that all the charged tracks are assumed to be pions. The other one is that all the calorimeter showers which are not linked to tracks are assumed to be photons. These assumptions for particle masses are essential for boosting the particles to the centre-of-mass frame. In the ensuing discussion, all variables will be defined in this frame.

The algorithm defines three axes, namely, the beam/target jet axis (axis 1), the recoil jet axis (axis 2) and the trigger jet axis (axis 3). In the first step, beam direction is chosen as axis 1, direction of the leading particle as axis 2 and direction of the trigger particle as axis 3. The leading particle is defined as the highest p_T particle opposite to the trigger direction in azimuth (i.e. ϕ angle) in a sector of $\phi > 120°$. It is also required to have a p_T greater than 500 MeV/c.

Each particle is assigned a weight with respect to all the three axes given by w_1, w_2 and w_3 respectively. A weight is defined with respect to a chosen axis as

$$w = \frac{p_{\parallel}}{p} exp(-5.0 p_T) \qquad (1)$$

where:

$p_{\parallel}$ = component of the momentum of the particle in the direction of an axis

p_T = component of the momentum of the particle perpendicular to the direction of an axis, and

p = total momentum of the particle

Then the probability of the particle belonging to a certain jet along axis i is given by,

$$P_i = \frac{w_i}{w_1 + w_2 + w_3} \tag{2}$$

Each particle is assigned to the axis for which it has the largest probability. One can calculate the jet direction by summing the vectors of all particles with $P > 0.34$. A second iteration is then performed using the calculated jet direction as input. The final association is achieved by ordering all particles according to their P values.

It is observed that the particles assigned to a jet satisfy the following criterion in the space of pseudorapidity and azimuthal angle,

$$\sqrt{(\eta_{jet} - \eta_{track})^2 + (\phi_{jet} - \phi_{track})^2} \leq 1$$

Some cuts were imposed then to ensure the validity of the recoil jet.

- There must be at least one particle in the jet.
- Only particles with p_T greater than 250 MeV/c can belong to the recoil jet.
- The transverse momentum of the jet must be greater than 20% of the transverse momentum of the trigger.

- The jet direction must be roughly opposite to the trigger direction in azimuth in a sector of $\phi > 120°$.
- The rapidity of the trigger jet must be between -0.8 and 0.8 and for recoil jet between -1.0 and 1.0. This is done in order to avoid those events where the trigger or recoil jet overlaps with the beam or target jet.

Once the particles are assigned to a jet, the momentum of a jet can be found by summing the momenta of all particles in a jet. In the c.m. system, since the momenta of jets are equal and opposite, the momenta of the recoil jet is scaled such that the trigger and recoil jets have the same transverse momentum with respect to the beam direction. The scaling of the momenta helps in ignoring the transverse motion of the partons, k_T and also overcomes the losses due to the reconstruction. The events which exhibited jet structure with respect to the π° in the trigger jet were further considered for the study of strange particle production in the recoil jets.

5.3 MONTE CARLO STUDIES

For the interpretation and comparison of the data as well as to check the efficiency of the jet reconstruction code, a monte carlo study was performed on the simulated events generated by QCD-based ISAJET Monte Carlo program[41].

ISAJET generates high-p_T jets from partons, which scatter according to lowest-order perturbative QCD. The scattered partons are evolved into a cascade of quarks and gluons which finally fragment independently following the Feynman-Field model[42]. Events were generated with jets recoiling against high p_T neutral particles such as direct photon and π°. These events were used as

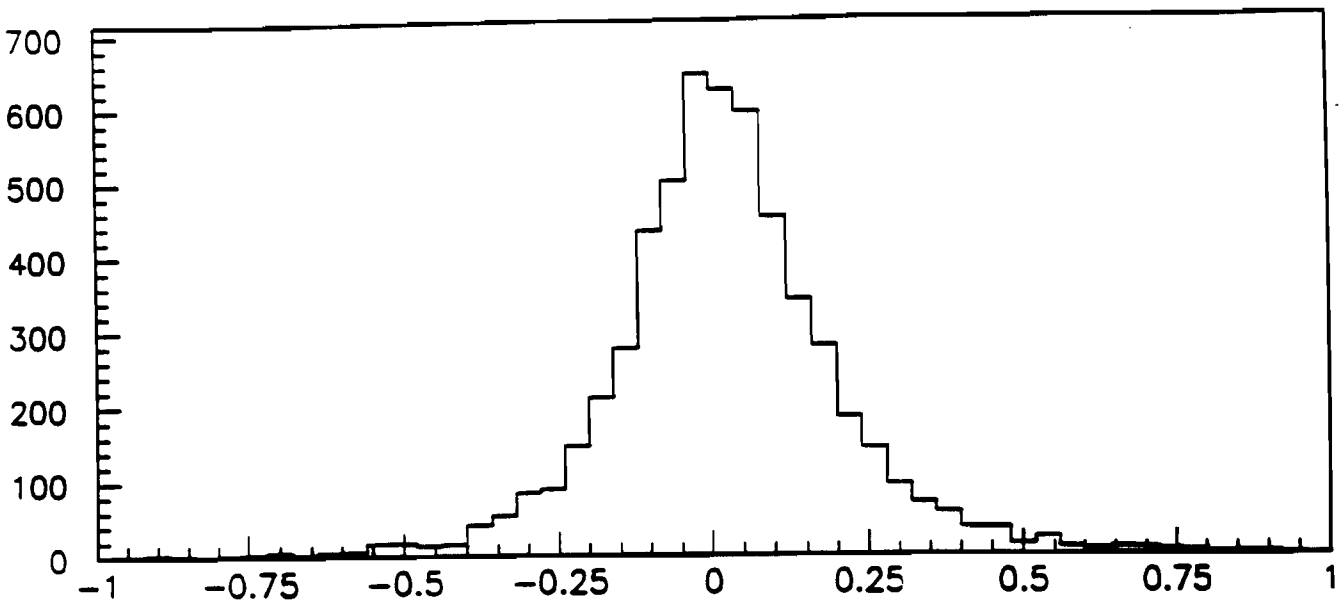

Figure 45 – Rapidity Difference between Reconstructed Recoil Jet and Generated Recoil Jet.

input to the jet reconstruction code for the analysis of the jets.

In Fig. 45, the difference between the rapidity of the reconstructed recoil jet and generated recoil jet is plotted. In Fig. 46, the difference between the ϕ of the reconstructed recoil jet and generated recoil jet is shown. These plots demonstrate the reliability of the jet reconstruction code with the shown resolutions. The efficiency of the jet reconstruction algorithm is defined as the ratio of the number of reconstructed jet events to the number of events selected for the jet reconstruction. In Fig. 47, the efficiency of the jet reconstruction algorithm is plotted against p_T of the trigger and the pseudorapidity, η. The jet efficiency is fairly constant with respect to rapidity of the jet.

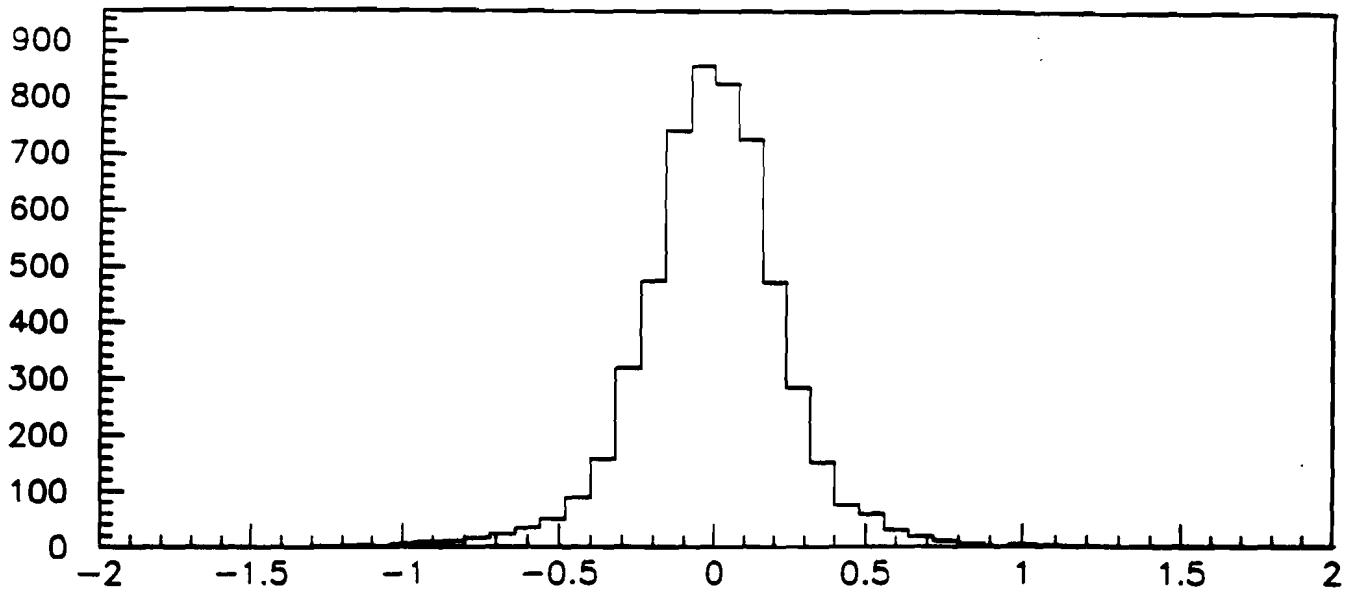

Figure 46 – Azimuthal angle, ϕ, difference between Reconstructed Recoil Jet and Generated Recoil Jet.

5.4 Results of Jet Reconstruction

The investigation of the fragmentation properties of jets allows several QCD assumptions to be tested, such as the universality of quark-gluon fragmentation independent of the initial state (parton-parton or e^+e^-), Q^2-dependent scale-breaking effects, no flavor correlation between away and toward jets[43].

Longitudinal Jet Structure The longitudinal fragmentation function for a quark of type q to produce a hadron is defined as the hadron density per unit of z:

$$D(z) = \frac{dn(z)}{dz}$$

where $n(z) = \frac{N_{ch}(z)}{N_{jet}}$ is the fractional number of particles per jet as a function of z and z is the fractional jet momentum carried by the particle in a jet defined

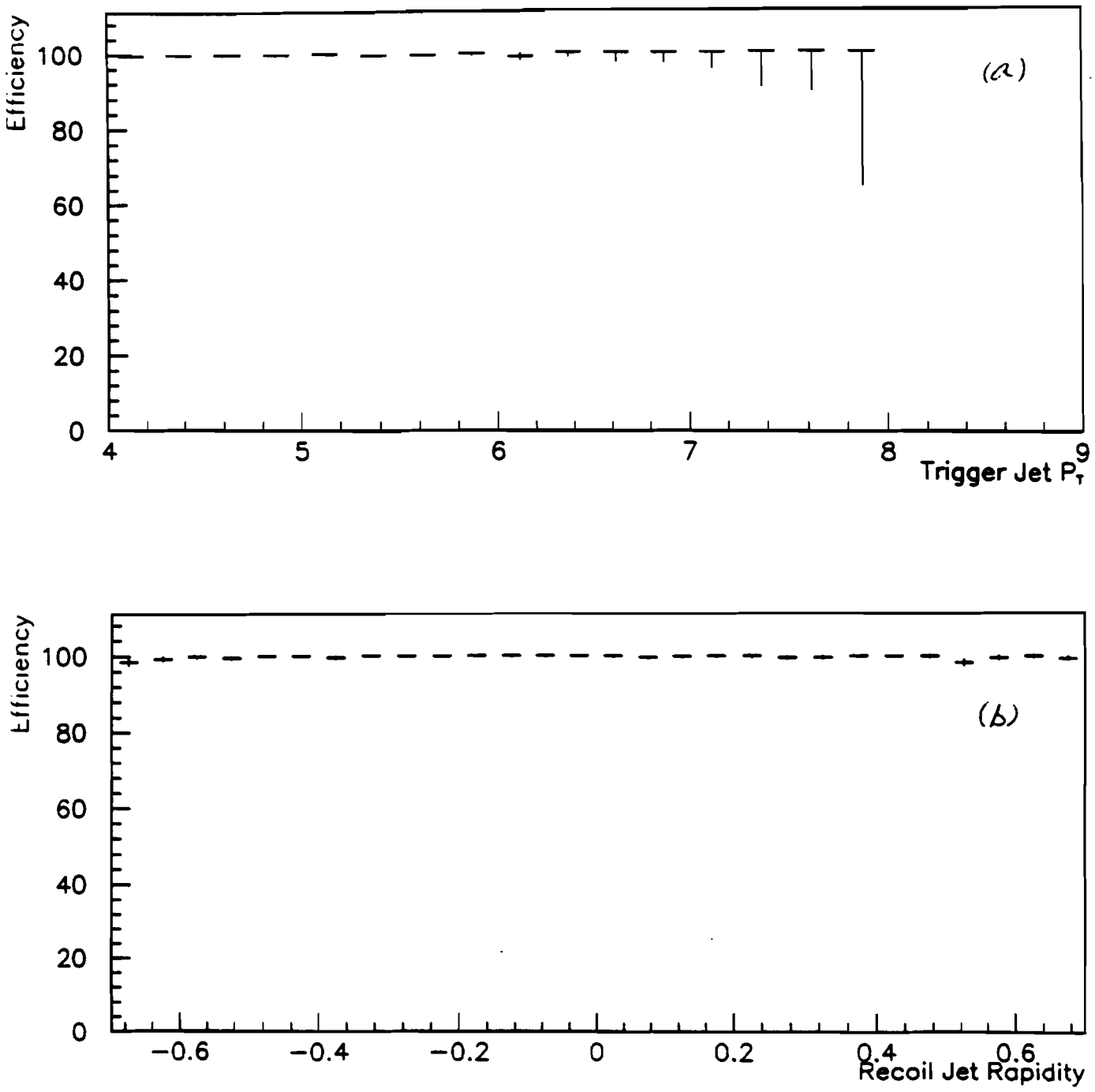

Figure 47 – Jet Reconstruction algorithm efficiency versus (a) p_T of the Recoil jet and (b) pseudorapidity of the Recoil jet.

as

$$z = \frac{\overline{P}_{track} \cdot \overline{P}_{jet}}{|\overline{P}_{jet}|^2}$$

This z assumes a perfect balance between the jet and the trigger particle to avoid the painful estimate of the jet momentum.

In Fig. 48 and Fig. 49 the fragmentation function for charged particles is plotted as a function of z for various types of beam on a Be target. Superimposed on the p-Be data is the ISAJET prediction which is available for positive data only. The data seems to agree with the monte carlo predictions both in magnitude and slope at high z. The shape of the fragmentation functions at very low z represent soft particles where it is extremely difficult to understand all the losses. Also the fragmentation function determined from π^--Be is no different from that obtained from p-Be.

Transverse Jet Structure The observed transverse momentum squared distributions (q_t^2) of charged particles are displayed in Fig. 50 and Fig. 51 as a function of ${q_t}^2$, which is measured relative to the jet axis. After a sharp exponential fall up to ${q_t}^2 \approx 1\mathrm{GeV}^2/\mathrm{c}^2$, there is a tail which shows a rising trend. The limited acceptance of the jets in the detector precludes a good measurement of the tails of the q_t^2 distribution. The monte carlo results obtained from ISAJET superimposed on the positive beam data, seem to be consistent with the observed distribution.

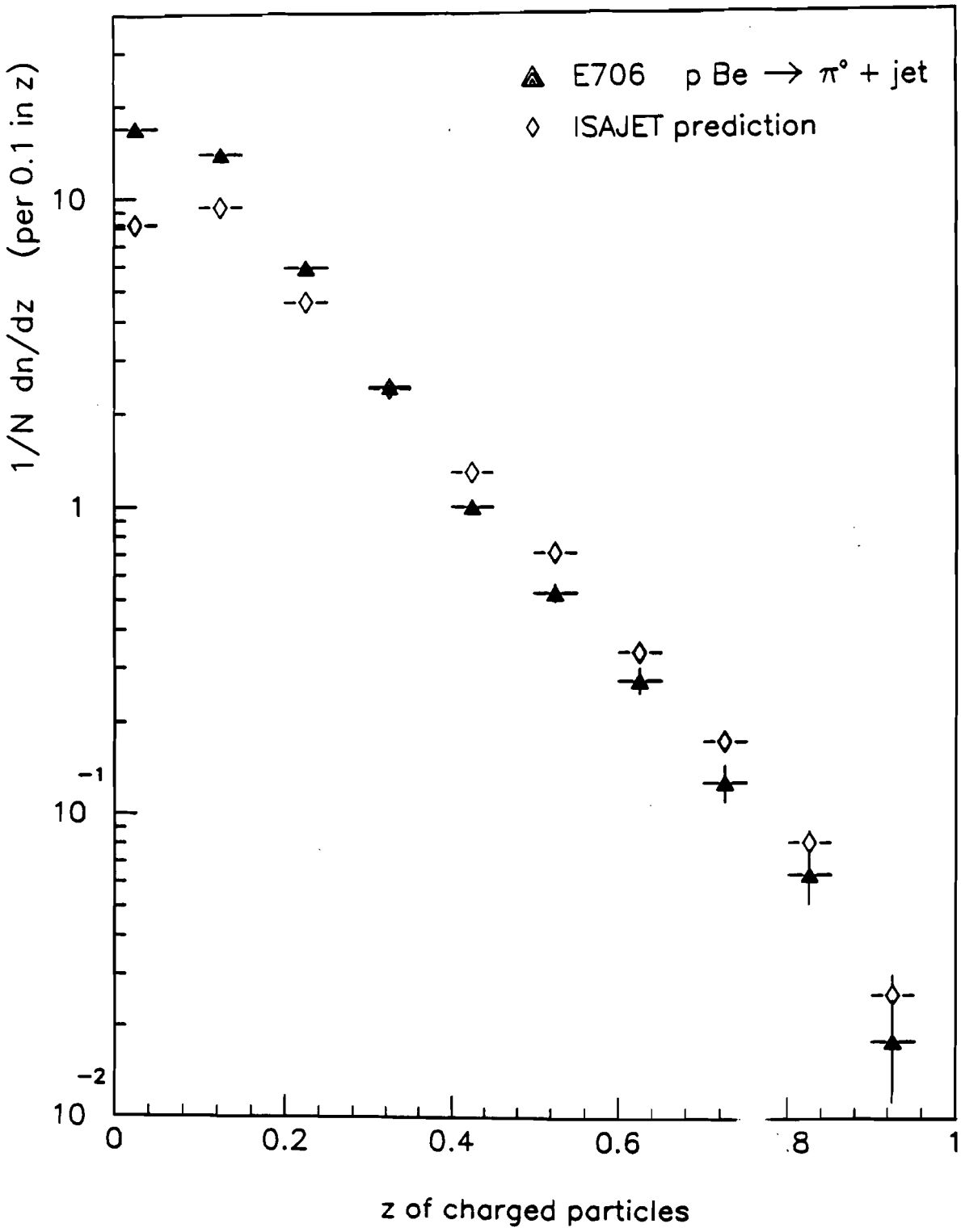

Figure 48 – Fragmentation function for all charged particles for positive beam.

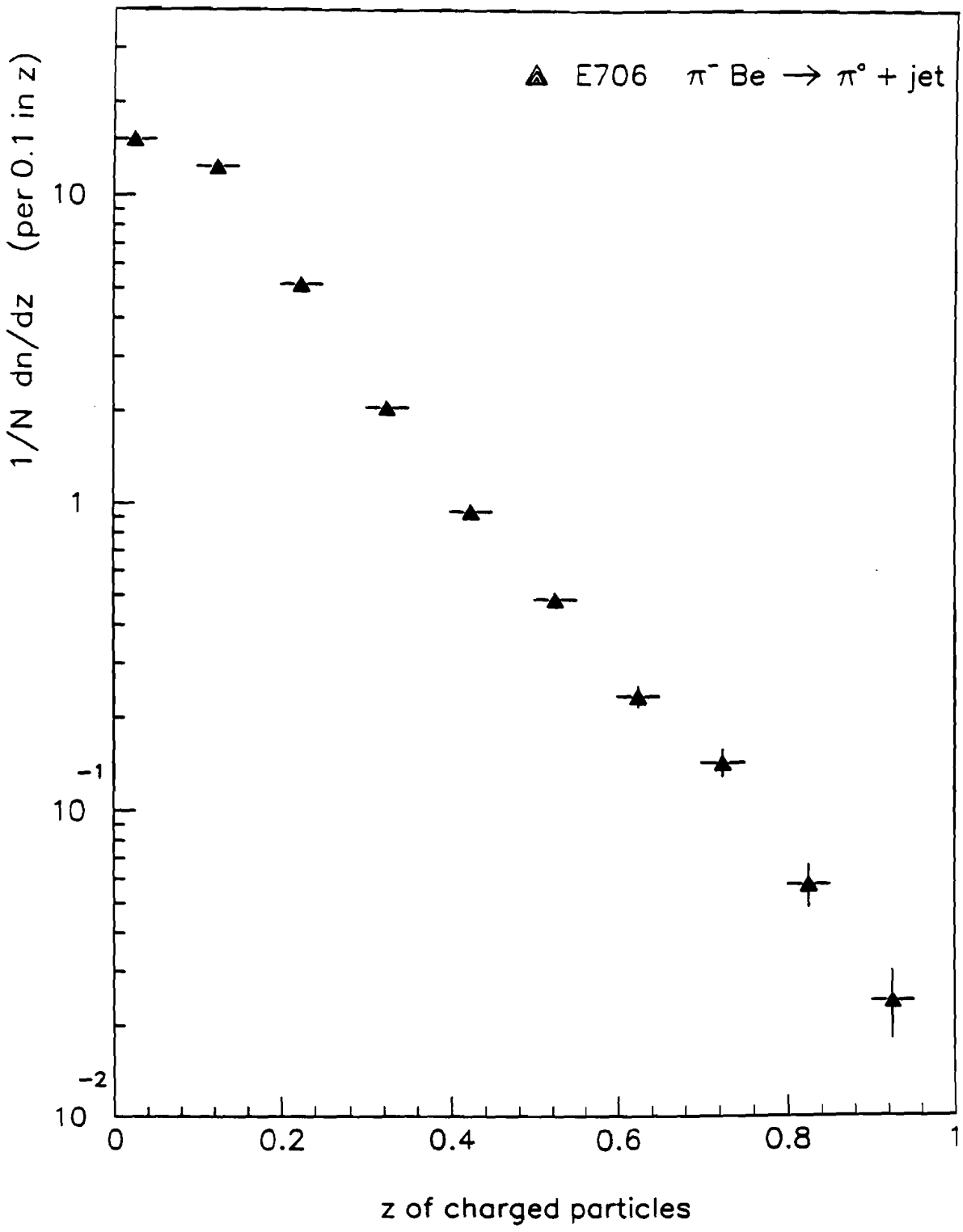

Figure 49 – Fragmentation function for all charged particles for negative beam.

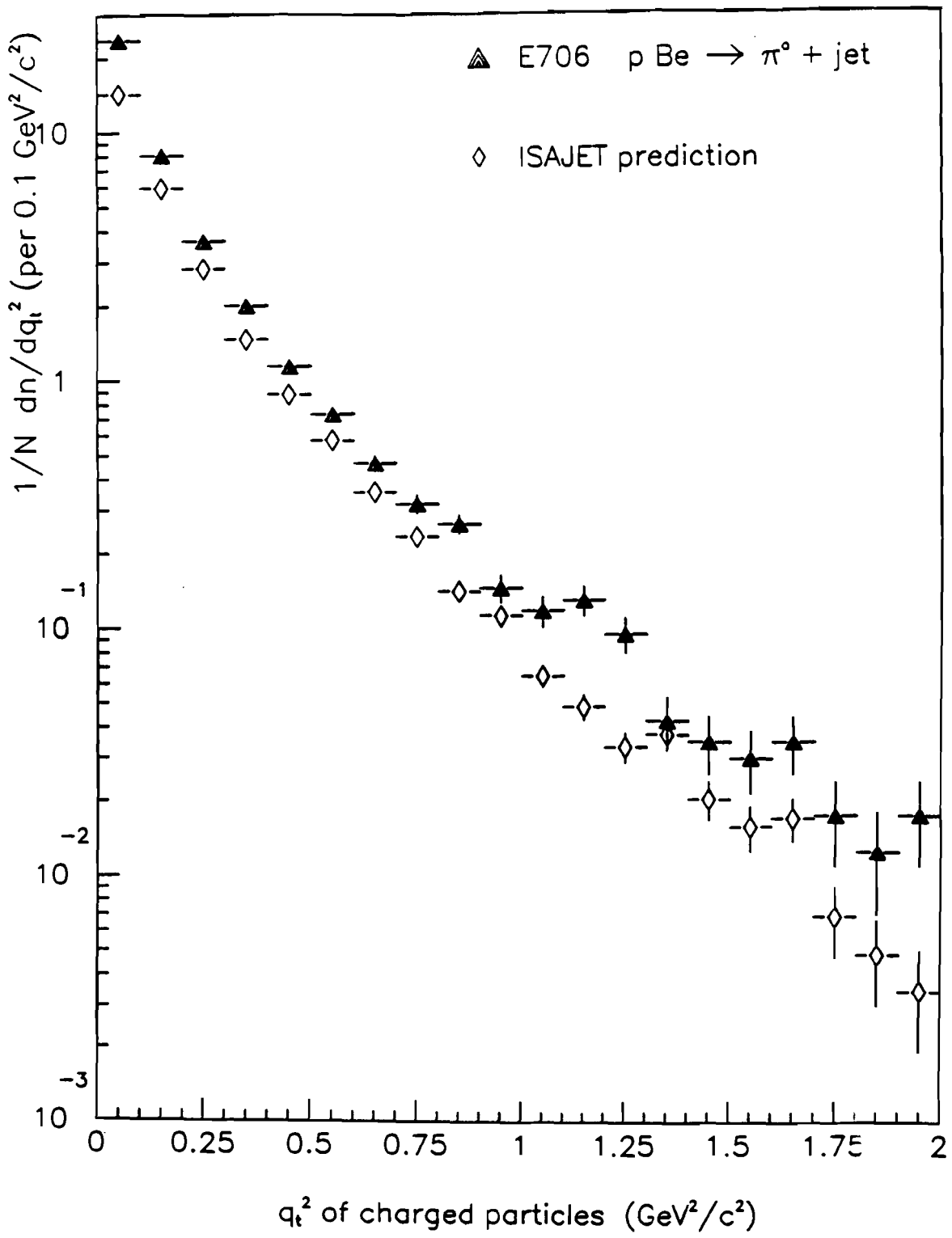

Figure 50 – Transverse momentum squared (q_t^2) distribution of all charged particles for positive beam.

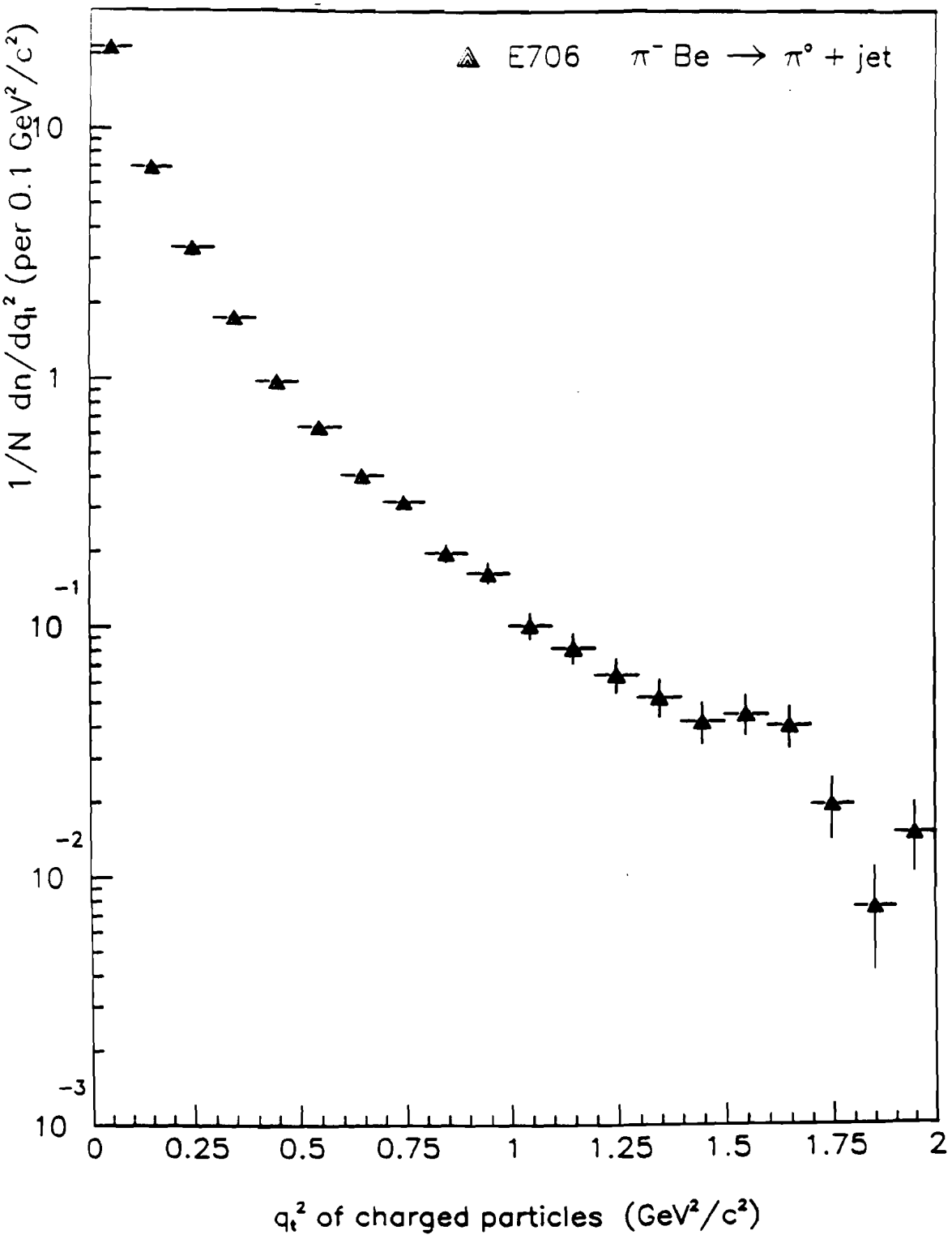

Figure 51 – Transverse momentum squared (q_t^2) distribution of all charged particles for negative beam.

5.5 Conclusion

It is seen from figures 42 and 44 that by imposing an asymmetry cut of $A < 0.75$, the $\gamma\gamma$ mass spectra becomes sharper. From figures 45 and 46 it is clear that the difference of rapidity and azimuthal angle between reconstructed and monte carlo generated recoil jets respectively shows a peak at ~ 0. The efficiency of jet reconstruction algorithm is found to be high (fig. 47). The fragmentation function for p-Be interactions is in beautiful agreement with monte carlo predictions (fig. 48). Similar conclusions can be arrived at from transverse momentum squared distribution of charged particles in p-Be interactions (fig. 50). The fragmentation function (fig. 49) and transverse momentum squared distribution (fig. 51) for π^--Be interactions show a similar distribution as that for p-Be interactions.

The above results amply demonstrate the justifications of the methodology followed here for jet reconstruction.

6. Results

As mentioned in Chapter 1, a good understanding of the fragmentation is necessary to extract dynamical features of parton processes. Knowledge of the strangeness component in the parton fragmentation was extracted from the observed jets of colorless hadrons. This Chapter describes the results on the strangeness observed in high p_T jets in terms of fragmentation functions. Various ratios of fragmentation functions for the strange particles with those for charged pions have been calculated.

Also, ratios between strange baryons and strange mesons are presented. Wherever possible, an attempt has been made to compare with monte carlo predictions.

For the production of strangeness in the recoil jets of high p_T (> 3 GeV/c), the following reactions were studied for the K^0_s, Λ and $\overline{\Lambda}$ observed in the jets.

For K^0_s

$$\pi^- Be \rightarrow \pi^0 + K^0_s + X \qquad (1)$$

$$p\, Be \rightarrow \pi^0 + K^0_s + X \qquad (2)$$

For Λ

$$\pi^- Be \rightarrow \pi^0 + \Lambda + X \qquad (3)$$

$$p\, Be \rightarrow \pi^0 + \Lambda + X \qquad (4)$$

For $\overline{\Lambda}$

$$\pi^- Be \rightarrow \pi^\circ + \overline{\Lambda} + X \tag{5}$$

$$p\, Be \rightarrow \pi^\circ + \overline{\Lambda} + X \tag{6}$$

6.1 Jet Reconstruction with Strange Particles

The algorithm for reconstructing a high p_T jet has been described in section 5.2. The same algorithm was used for studying production of strange particles in the jets. Charged tracks identified as decayed tracks of K_s° were removed from the charged track sample and a neutral track (K_s° track) was added to the event. If this neutral track passes all the cuts similar to charged track cuts, it was kept and considered for the jet calculation otherwise it was flagged for dropping from the jet calculation. The same procedure was performed for the Λ and $\overline{\Lambda}$ particles. A neutral particle such as K_s°, Λ or $\overline{\Lambda}$ was assigned to the away side jet if the particle satisfied all the aforementioned criteria for being a jet fragment.

As described in Section 2.1, a differential gas cerenkov counter was used to tag on K^- particles present in the negative beam. In the positive beam, however, the K^+ particles were not tagged as they make up only a small fraction of the beam (1.5 %) and hence they present a small background (8 %) in the π^+ sample. Statistics of the events were obtained with and without K particles in the beam from which the contribution to the jets from tagged K was calculated.

In order to not deplete statistics, events with more than one K_s° were kept as they make only a small fraction, namely 5% of the total K_s° sample. Also,

if an event contains more than one type of strange particle, no correction was applied to the jet because the contribution from such type of events was very low. (It was observed that only a small fraction 0.014 of the events containing K_s^o and Λ appears in K_s^o sample.)

All the distributions presented here have been normalized with respect to the number of events. Also, the horizontal error bars shown here indicate the bin size and the vertical error bars show the uncertainty on the data in that bin.

Monte Carlo for Strange Results The Monte Carlo scheme as described in Section 5.3 was used in order to compare the results obtained for strange particles. Again the events were generated using the ISAJET Monte Carlo program. In this model, one has the advantage of changing s/u quark ratio, thus changing the production composition of different parton flavors. The s/u suppression factor can be understood as the relative probability of exciting a quark and anti-quark pair from the vacuum within the framework of Field-Feynman fragmentation. This s/u composition was varied in MC until a good comparison with the data was obtained. Since the production mechanism for charged kaons and the neutral kaon is the same, charged kaons were generated instead of neutral kaons.

Jets containing strange particles, baryons and mesons were generated, recoiling against a high p_T π^o trigger. Two binary streams were obtained, one for all events and the other for events with strange particles only. The Jet algorithm was applied on both the stream and the fragmentations distributions were obtained for strange particles and the charged particles.

Summary of Events

Table 6 gives the summary of the raw events obtained for various types of

strange particles. As one observes, the various cuts have the similar kind of effect on the different strange particles observed. The away side jet cut has the largest effect on the data: only 25 % of the events survived. The rest of them go to either beam jet or trigger jet.

Cuts applied	K°	Λ	$\overline{\Lambda}$
Number of π° + jet events	92020	92020	92020
Strange Particle cut	5249	1135	852
Trigger cut	4511	982	742
Cerenkov cut	3938	866	667
Away-side jet cut	1045	212	152
Z-window cut	611	212	152
$\cos\theta^*$ cut	488	102	69
Side Band subtraction	249	31	17

Table 6 – Summary of the strange particles results. The table entries are those number of events surviving the listed cut.

The number of strange particles presented above are without any acceptance correction. The acceptance corrections as mentioned in Section 4.6 were applied on the jet events for the results that follow.

6.2 Fragmentation Results for K°_s

Fragmentation results for K°_s produced in the away side jets were obtained using the jet algorithm where π°s with p_T greater than 3.0 GeV/c were used as trigger particle. The fragmentation distributions were studied as a function

of the kinematical variables z and q_t^2, as defined in Chapter 5 for the charged particles.

In Fig. 52 and Fig. 53, fragmentation distribution function for the process of equation (1) and (2) respectively is shown as a function of z. Both distributions seem to have a peak which is shifted away from zero. It has been suggested[44] that these particles may, in fact, reflect the characteristics of the soft partons – a kind of parton-hadron duality. The kinematic threshold requires that the data turn over at the appropriate mass values, but the low z region is also depleted by the coherence of the low energy gluon radiation, which leads to a destructive interference. Therefore, kaon and higher masses particles should peak higher because of larger masses.

Fig. 54 and Fig. 55 show the transverse momentum squared distribution for K_s° in negative and positive beam respectively. The distributions seem to fall off exponentially. Again one should expect a wider distribution for heavier particles. TPC group[45] reported mean p_T^2 values of 0.30 ± 0.02 GeV/c^2 for $\pi^\pm$ and 0.51 ± 0.20 GeV/c^2 for K°.

Beam Comparisons In Figures 56 (a) and (b), negative to positive beam ratio as a function of z and q_t^2 for K_s° is shown. Ratio seems to be consistent with one within error bars implying that there is no difference in production mechanism for K° in π^- or p beam. Table 7 gives the summary of the results obtained for K_s° from different beams types.

Production of K_s° in K^- beam as compared to π^- beam shows the enhancement. The number of events can be read in the Table 8. The ratio turns out to be 1.4 ± 0.22. This shows that the strange valence quark is participating in the

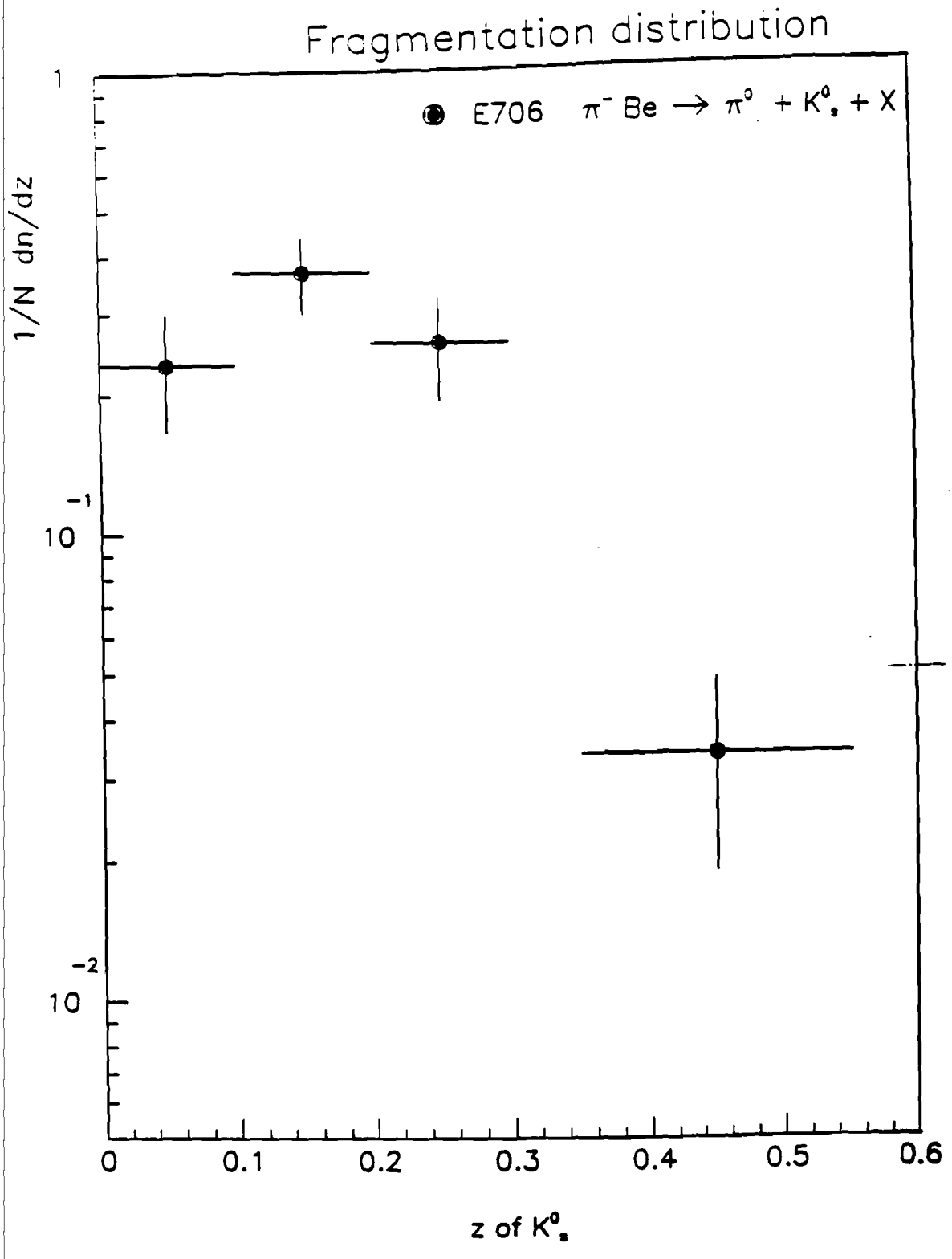

Figure 52 – Fragmentation function (z) for K^0_s particles for negative beam.

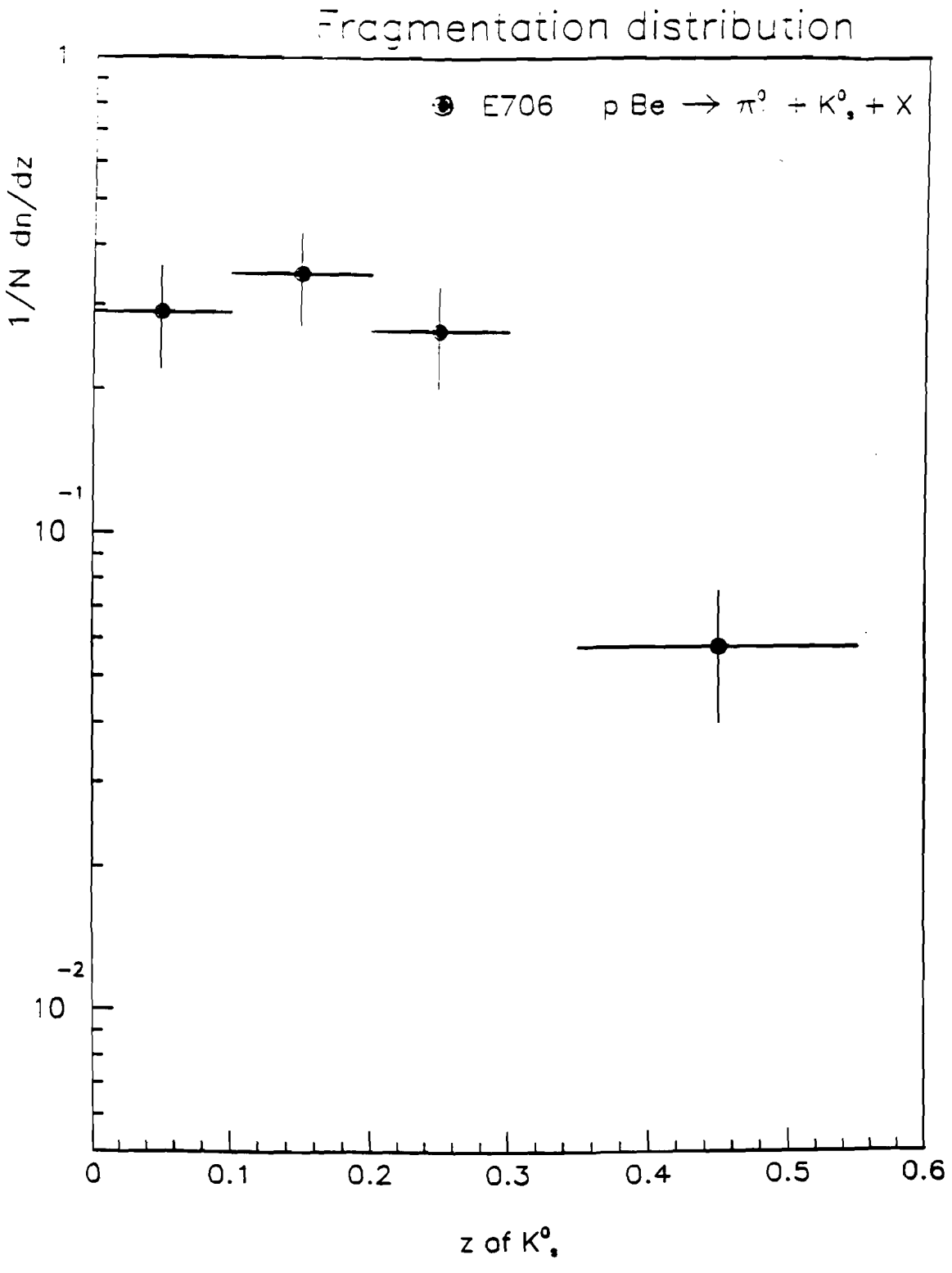

Figure 53 – Fragmentation function (z) for K^0_s particles for positive beam.

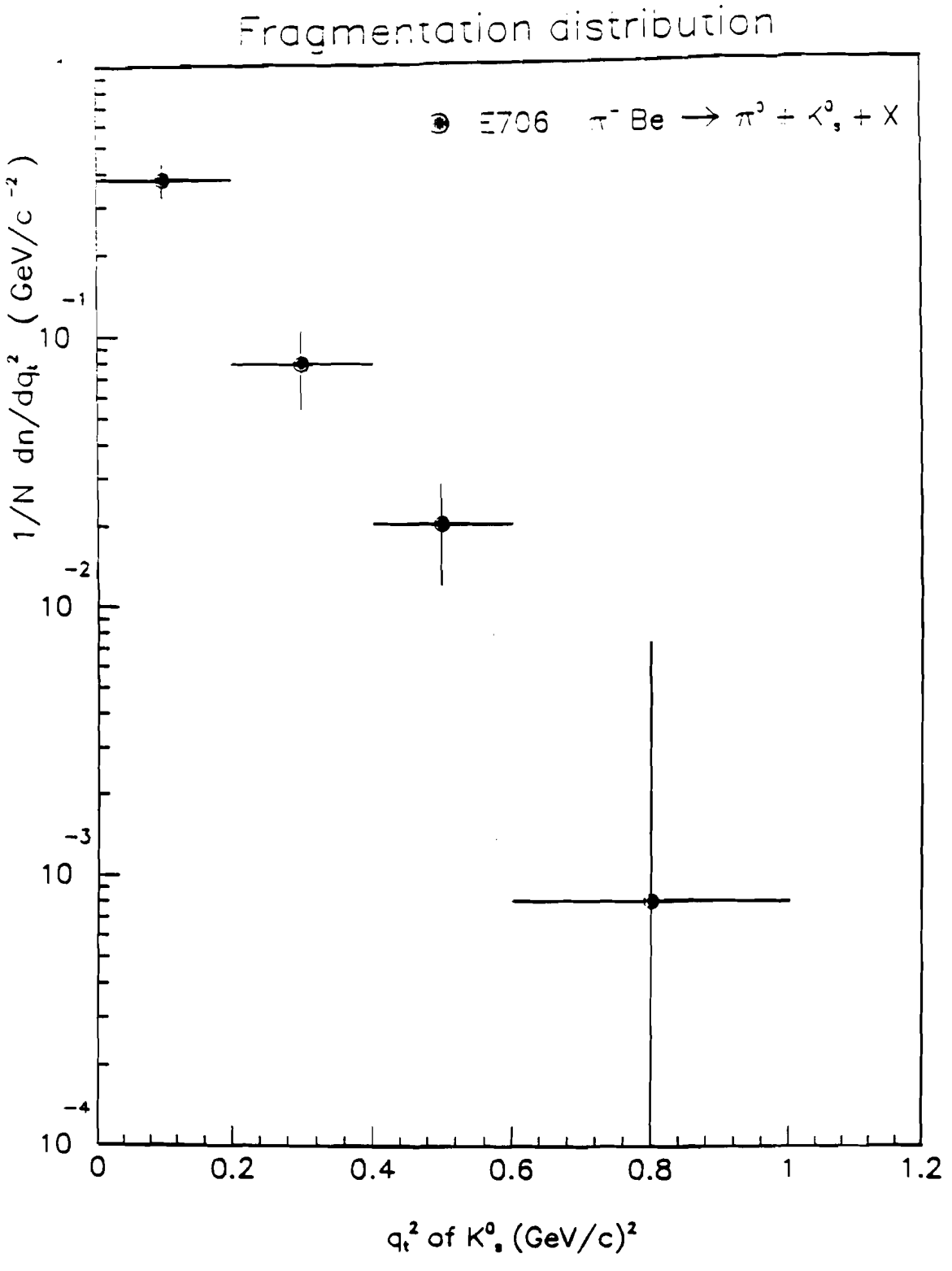

Figure 54 – Transverse momentum squared (q_t^2) distribution for K^o_s particles for negative beam.

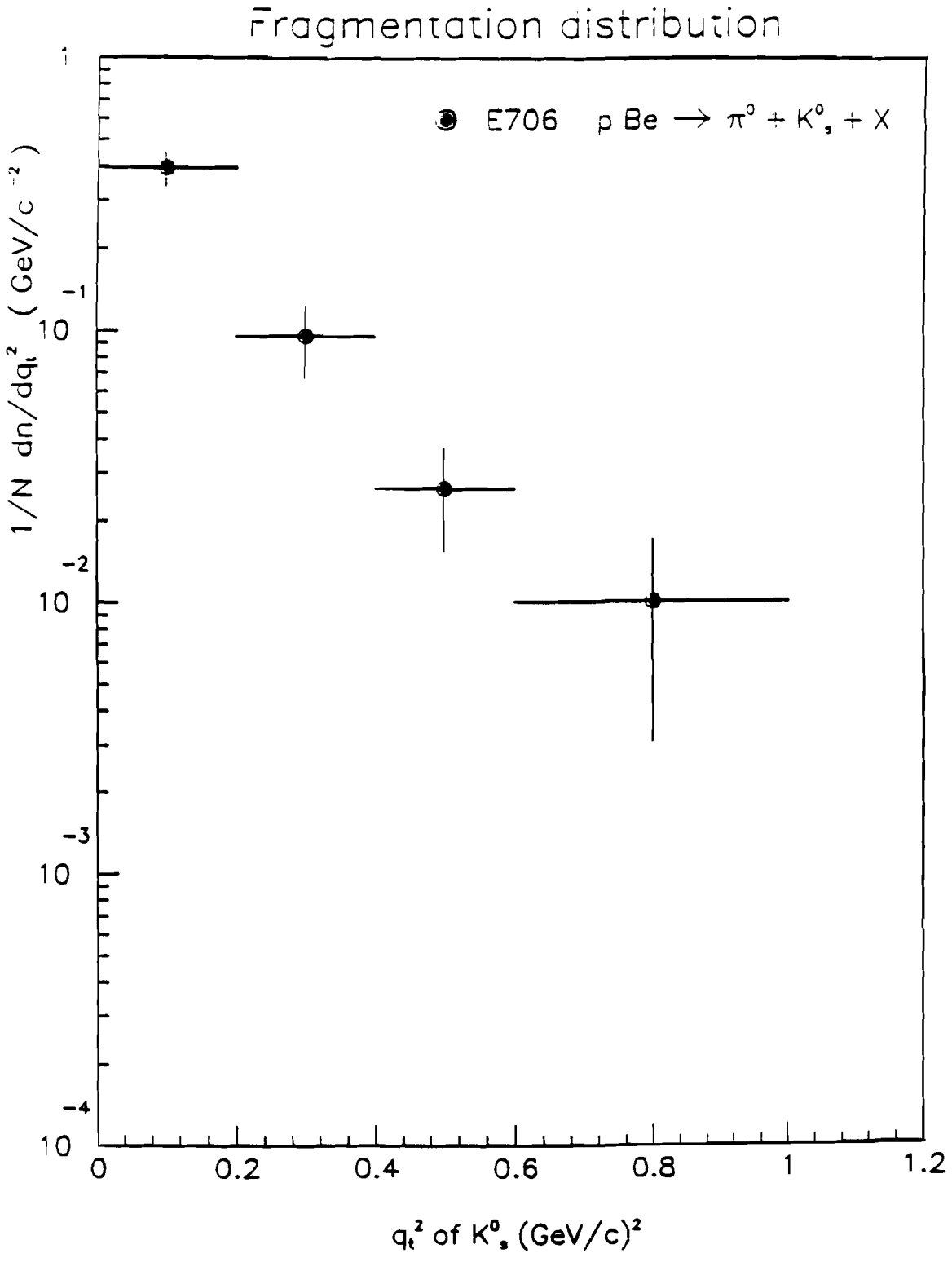

Figure 55 – Transverse momentum squared (q_t^2) distribution for K_s^o particles for positive beam.

Cuts applied	+ve Beam	-ve Beam
Number of π° + jet events	43120	48900
K° cut	2435	2814
Trigger cut	2095	2416
Cerenkov cut	1823	2115
Away-side jet cut	476	569
Z-window cut	286	325
$\cos\theta^*$ cut	226	262
Side Band subtraction	119	130

Table 7 – Summary of the K° production results in different beams. The table entries are those number of events surviving the listed cut.

production of excess K° mesons.

$$R = \frac{(K^-Be \rightarrow \pi^\circ + K^\circ + X)/(K^-Be \rightarrow \pi^\circ + X)}{(\pi^-Be \rightarrow \pi^\circ + K^\circ + X)/(\pi^-Be \rightarrow \pi^\circ + X)} = 1.4 \pm 0.22$$

K° Production in π° triggered events.			
Comments	K^- Beam	π^- Beam	p beam
Signal Region	64	185	163
Side-Band Region	13	55	44

Table 8 – Summary of the total events in different beam types.

Though the result is very significant but it's hard to make any concrete statement due to the limited available statistics.

Fig. 57 and Fig. 58 represents the fragmentation distribution results for K°_{s} for the combined statistics.

K/π Ratio Fig. 59 shows the K/π ratio as a function of z, assuming all charged particles as pions. Also superimposed on the data are various MC predictions. These MC predictions were obtained by varying s/u ratio. Since the spectrometer has very low acceptance ($\sim$ 50 %) for double K° events, MC predictions were divided by a factor of two in order to simulate the loss of those events. All the MC predictions seem to flatten out around 0.4 where the distribution lacks data. The K/π ratio as a function of q_t^2 is shown in Fig. 60 along with two MC predictions. All the data points lie between the MC curves which correspond to the K/π ratio between 0.04 and 0.06. The s/u ratio for the two curves is 0.17 and 0.22 as shown in the figure. It is not a surprise that there is not a good agreement in the shape of the z distribution because the fragmentation model of Field-Feynman employed by ISAJET does not have any dynamical differences for the production of strange quarks. We do expect the mass of the strange quark to play a role in fragmentation process, as evidenced in the data.

6.3 Fragmentation Results for Λ

Fragmentation results for Λ produced in the away side jets of high p_T interactions were obtained using the same jet algorithm which was applied to K°_{s}. Due to the limited statistics, Λ particles obtained in negative beam as well as positive beam were combined.

Fragmentation distribution results for Λ as a function of z are presented in Fig. 61. The peak has shifted further away due to the heavier mass of the Λ

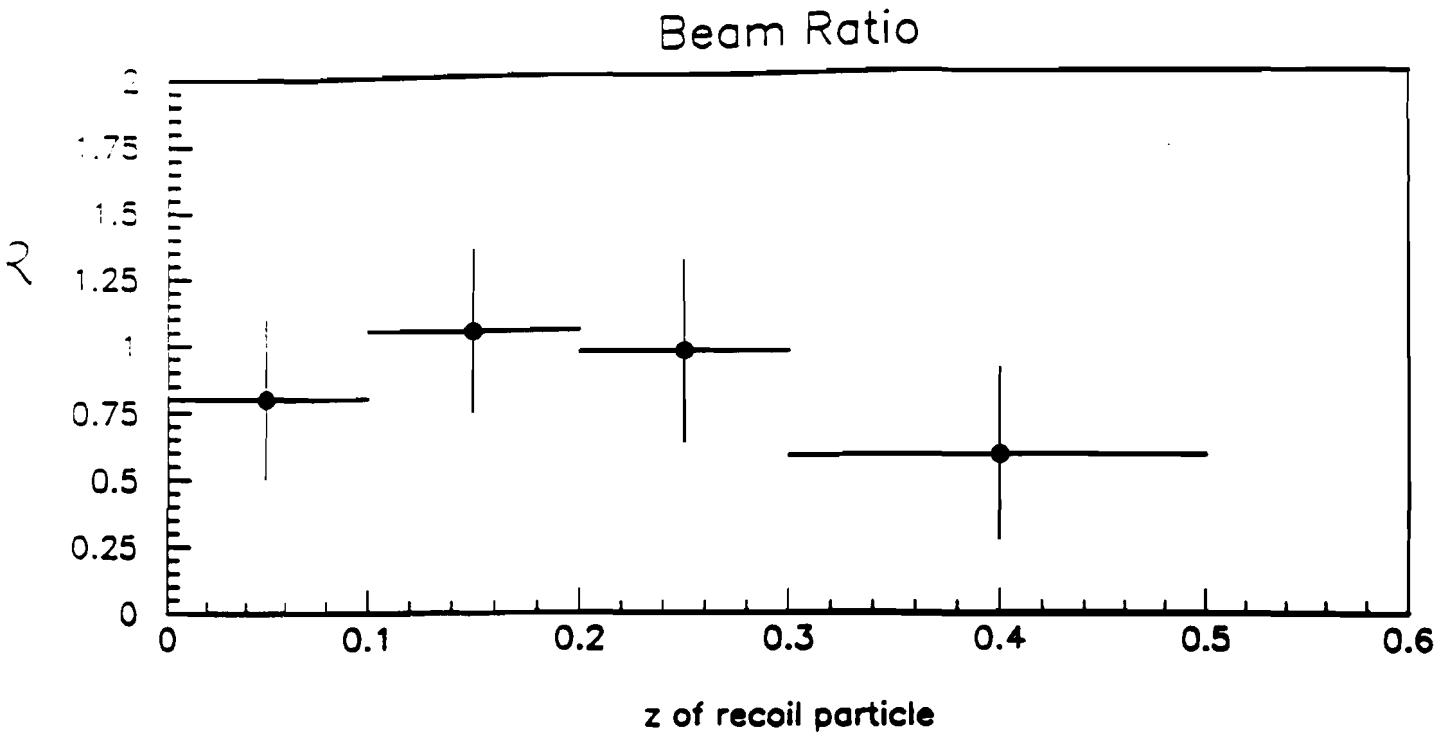

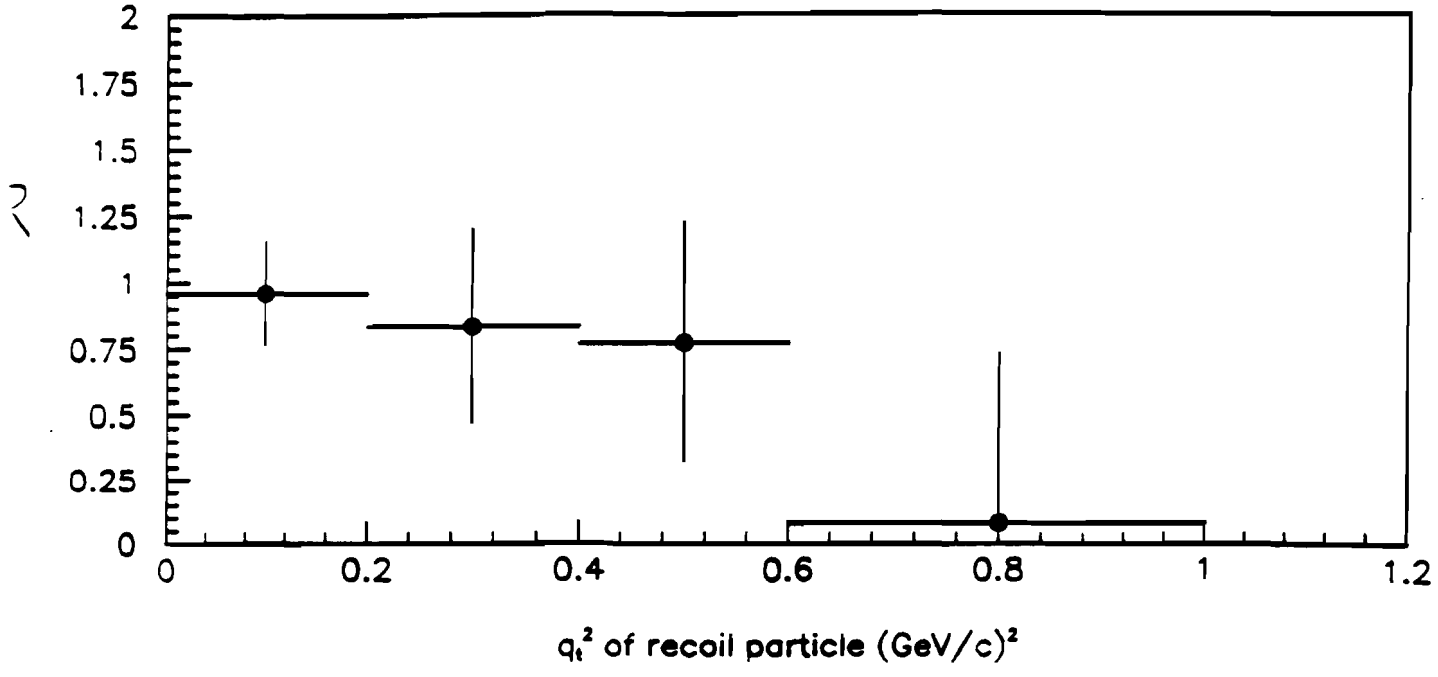

Figure 56 – Negative to Positive beam ratio for K° as a function of (a) z and (b) q_t^2.

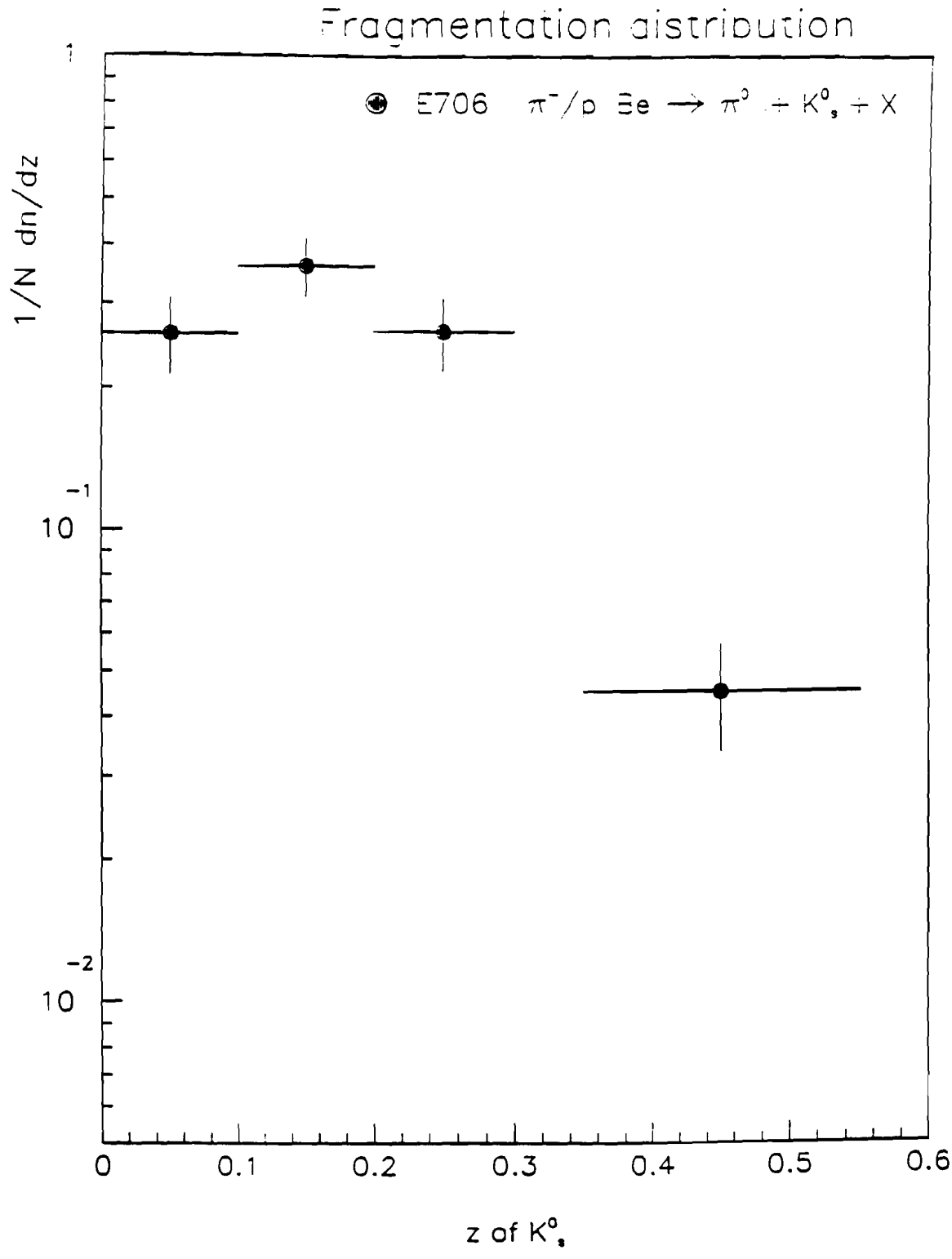

Figure 57 – Fragmentation function (z) for K^0_s particles for combined statistics.

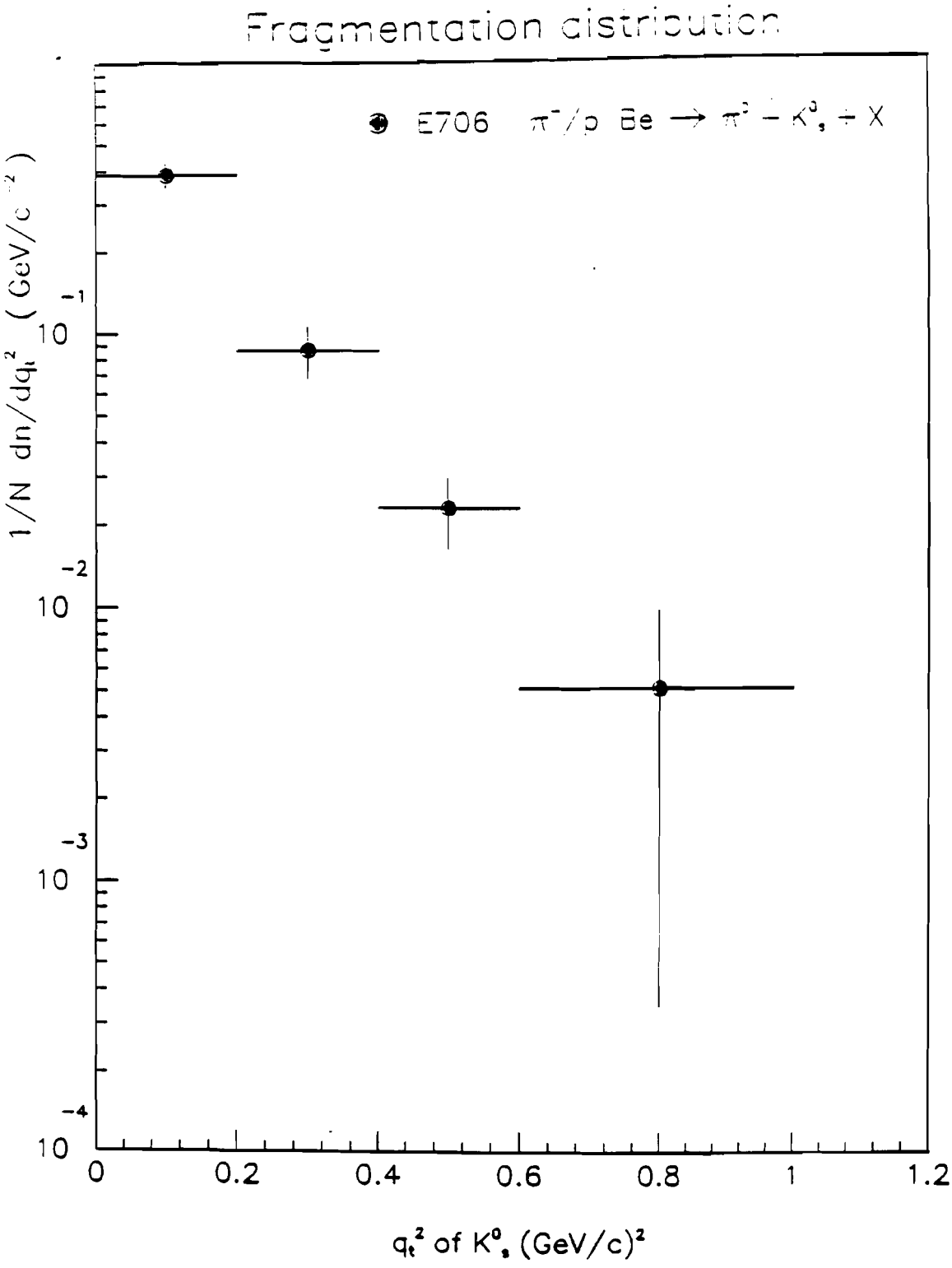

Figure 58 – Transverse momentum squared (q_t^2) distribution for K^0_s particles for combined statistics.

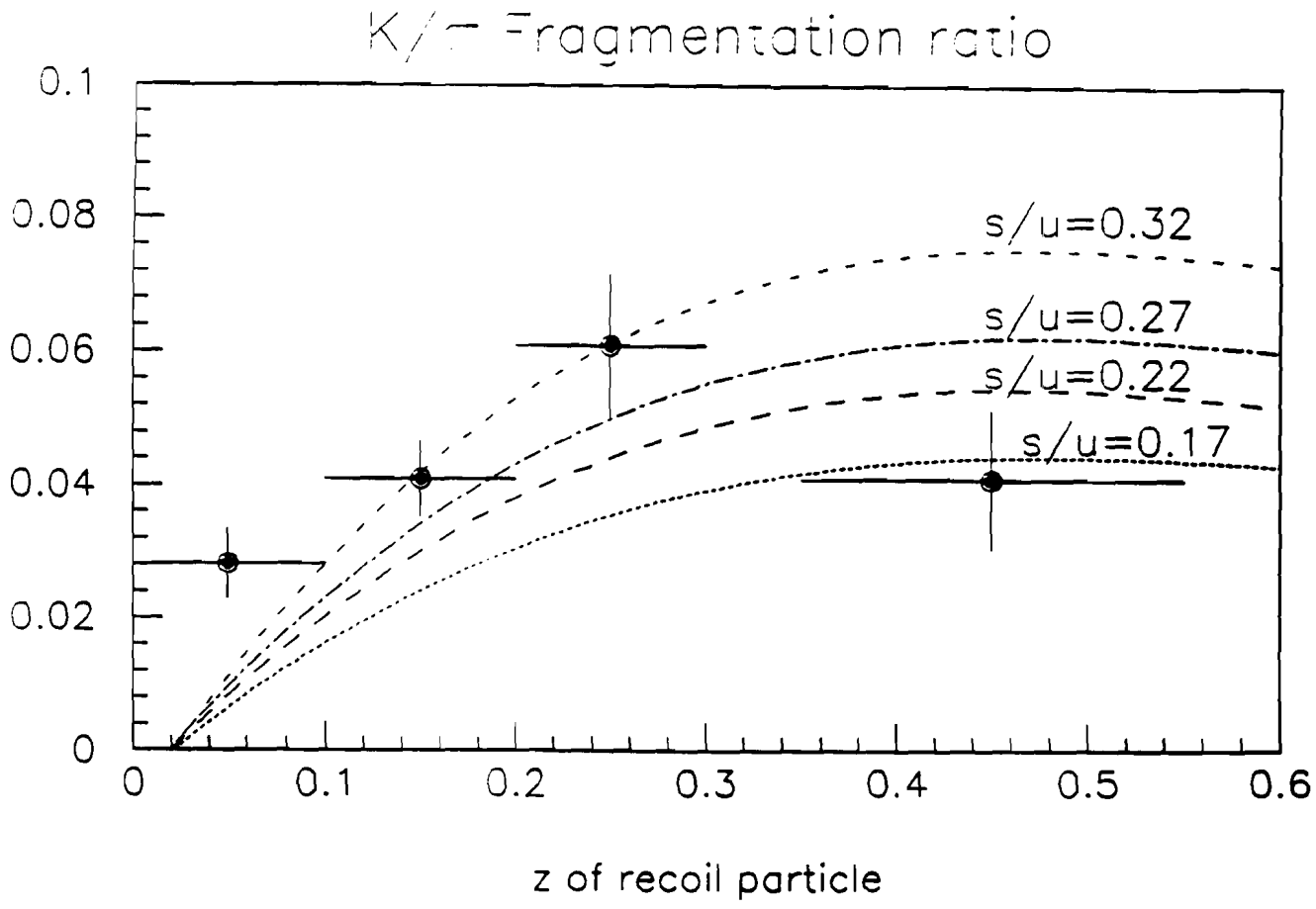

Figure 59 – K/π ratio as function of z.

particle than K°.

Fig. 62 represents the transverse momentum squared distribution for Λ as a function of q_t^2. The distribution falls less rapidly than for K_s^o indicating that the baryons are produced with more p_T with respect to the jet axis.

<u>Λ to K ratio</u> Figures 63 (a) and (b) show the ratio of Λ to K production in away side jets in high transverse momentum interactions as a function of z and q_t^2, respectively. The ratio shows a rising trend at low values in z but it's difficult to say for the q_t^2 plot due to limited statistics. The baryons to mesons ratio was

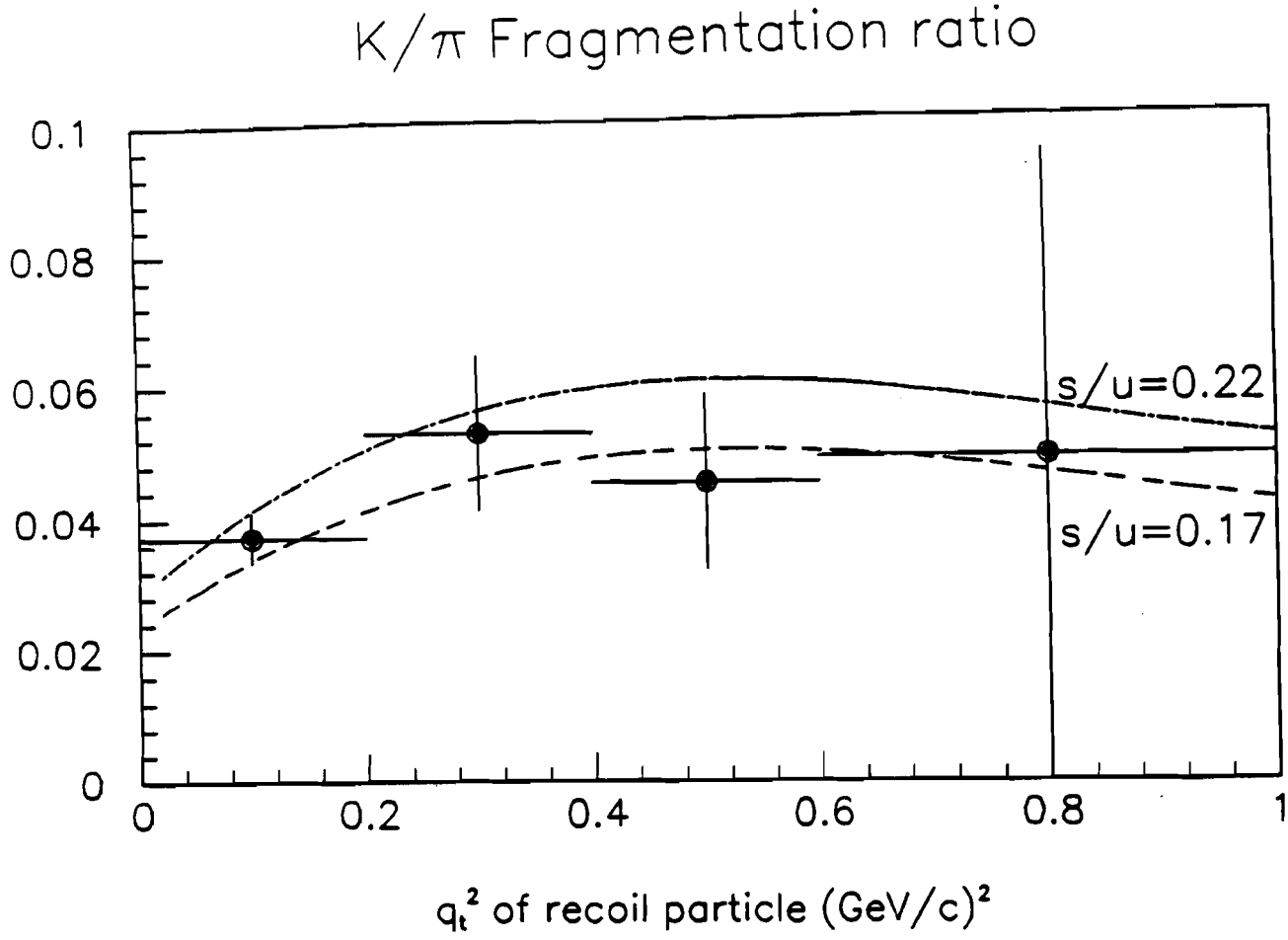

Figure 60 – K/π ratio as function of q_t^2.

measured from the acceptance corrected and side band subtracted jet events and the ratio is

$$\Lambda/K = 0.14 \pm 0.01$$

as compared to 0.1 predicted by ISAJET.

The ratio of $\overline{\Lambda}$ production to Λ was also calculated in the same way.

$$\overline{\Lambda}/\Lambda = 0.47 \pm 0.04$$

The ratio shows that the production of $\overline{\Lambda}$ is suppressed by a factor of two as

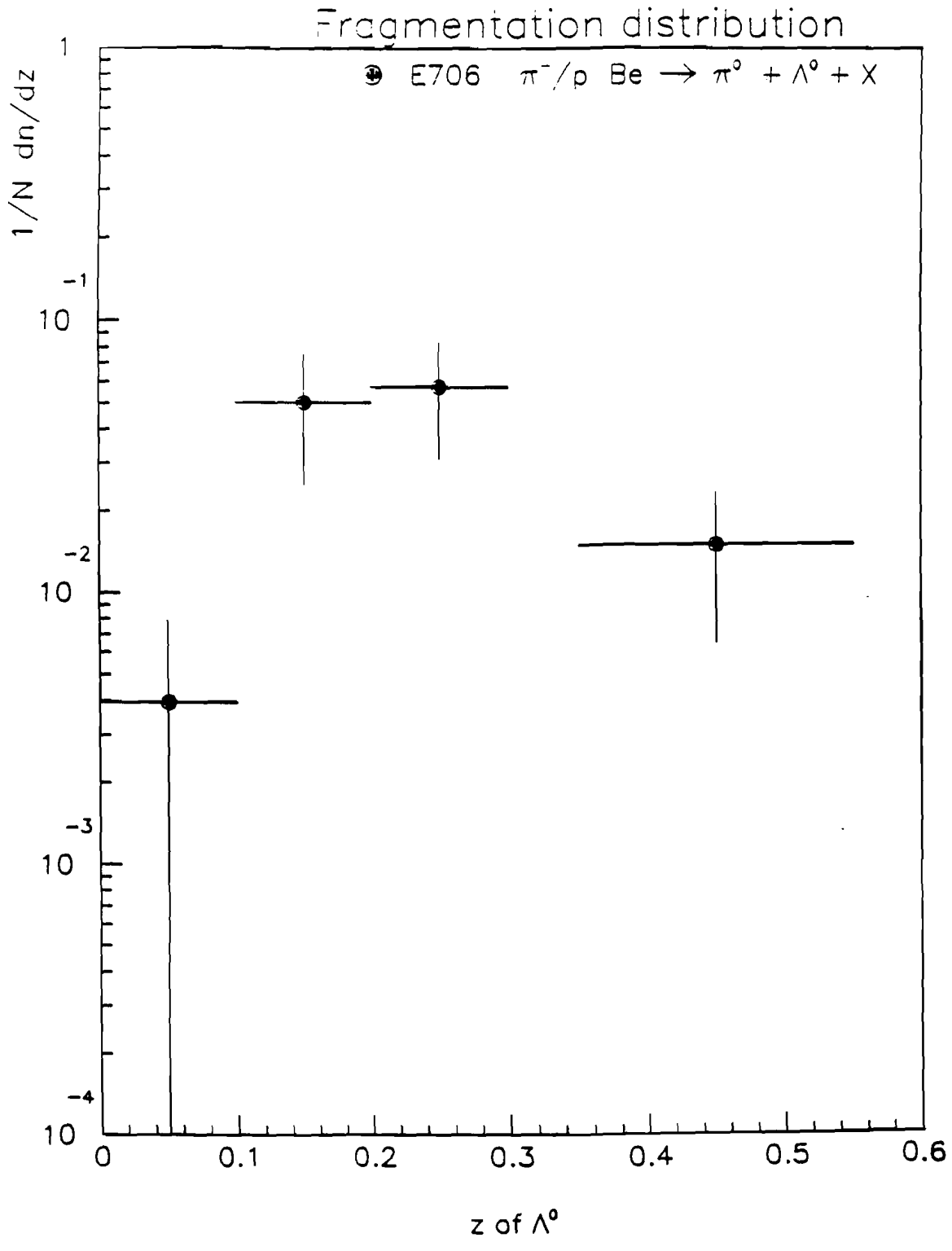

Figure 61 – Fragmentation function (z) for Λ particles for combined statistics.

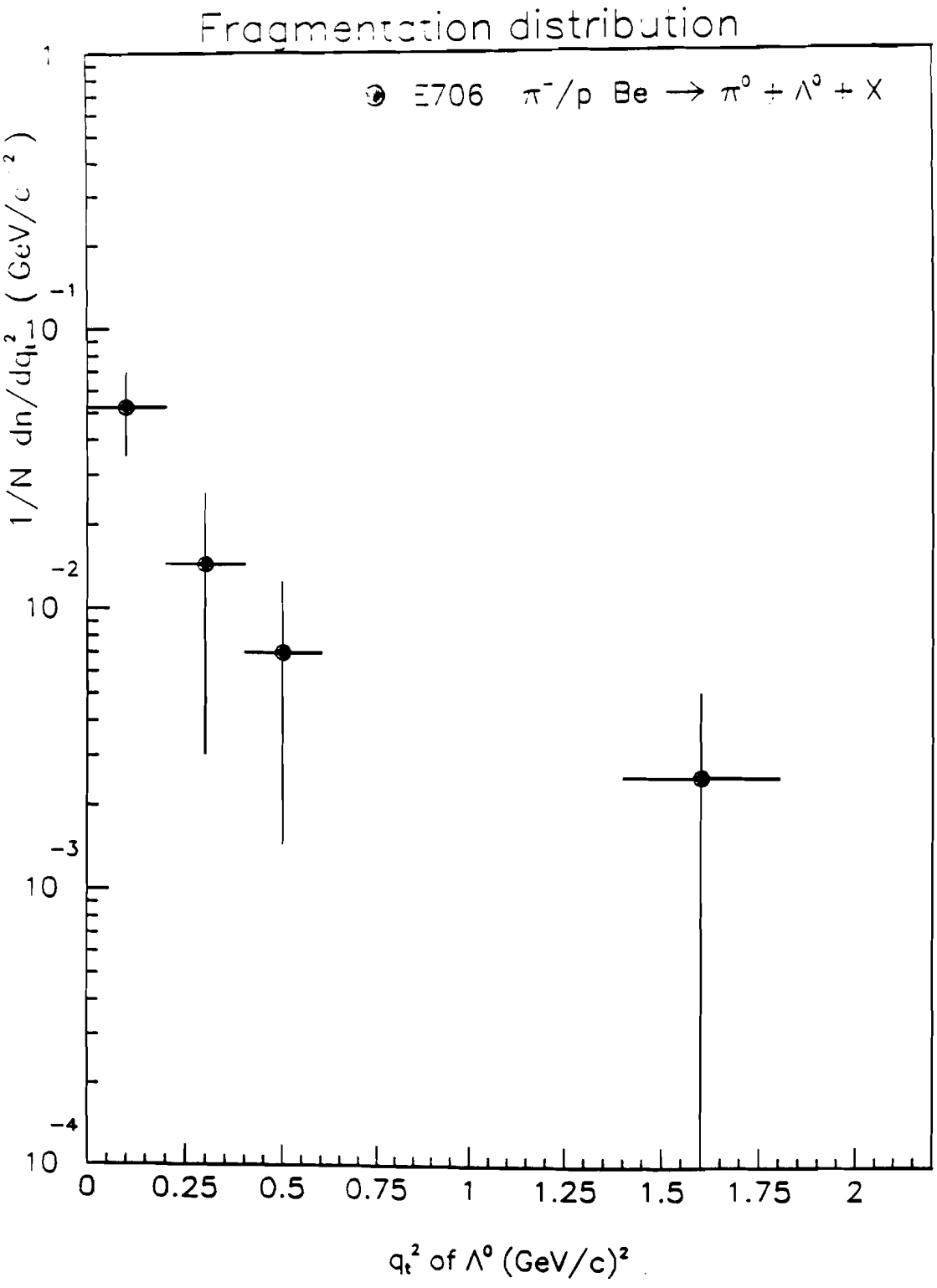

Figure 62 – Transverse momentum squared (q_t^2) distribution for Λ particles for combined statistics.

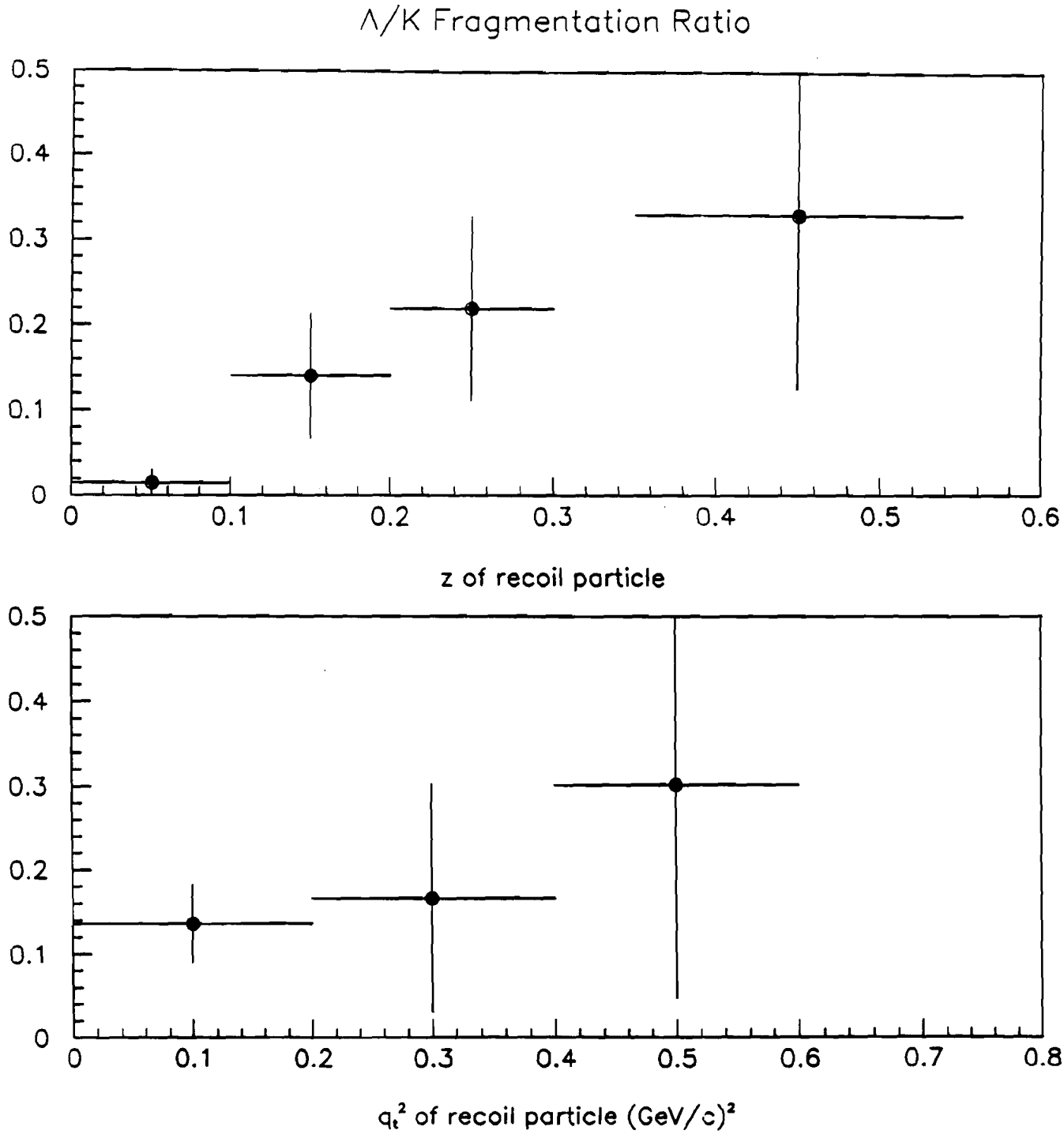

Figure 63 – Ratio of Λ to K production in away side jets recoiled against high p_T π^0 as a function of (a) z and (b) q_t^2.

compared to the production to Λ.

7. Conclusions

The fragmentation properties of strange particles produced in high transverse momentum interactions at $\sqrt{s} = 31.56$ have been measured. It was seen that charged particles distribution was in good agreement with the ISAJET predictions. Also the fragmentation distribution observed for π^--Be interactions was similar to p-Be interactions.

In the case of strange particles, the production mechanism for K°_s in high transverse momentum interactions shows the same z and q_t^2 dependence for π^- and p incident beam. Also the enhancement observed for the production of K° in K^- beam as compared to π^- beam indicates the presence of valence strange quark in the fragmentation process.

The K to π ratio was measured to be between 0.04 and 0.06 as compared to the value from 0.089 to 0.13 obtained by different experiments at very high range of $\sqrt{s}$ as reported by CDF experiment[46].

The fragmentation function for Λ gave further evidence for the softening of the fragmentation function with increasing mass.

The suppression factor for Λ to K was measured to be 0.14 ± 0.01 as compared to 0.1 predicted by ISAJET. Also the production of $\overline{\Lambda}$ to Λ was found to be suppressed by a factor of about two.

Therefore, within the scope of this study, we find that the production of strange particles is well predicted by the quark model and QCD.

REFERENCES

1. (a) S. Abachi *et al.*, HRS Collaboration, ANLHEP-PR-89-73 (1989); (b) W. Braunschweig *et al.*, TASSO Collaboration, DESY 89-156 (1989); (c) I.V.Ajinenko *et al.*, Z. Phys. C46 (1990) 525.
2. F. Halzen and A. D. Martin, *Quarks and leptons*, John Wiley, New York (1984).
3. T. Ferbel and W. R. Molzon, Rev. Mod. Phys. 56 (1984) 181.
4. R. P. Feynman, Phys. Rev. Lett. 23, (1969) 1415.
5. B. Alper *et al.*, Phys. Lett. 44B (1973) 521 and 527; M. Banner *et al.*, Phys. Lett. 44B (1973) 537; F.W. Busser *et al.*, Phys. Lett. 46B (1973) 471.
6. S. Berman, J. D. Bjorken and J. Kogut, Phys. Rev. D4 (1971) 3388.
7. R. P. Feynman, *Photon-hadron interactions*, Benjamin, New York, (1972).
8. J. F. Owens, Rev. Mod. Phys. 59 (1987) 465.
9. W. Hoffman, Int. Sym. of Strangeness in Hadronic Matter, June 1-5,1987, Bad Honnef, FRG, Nucl. Phys., A479 (1988) 337.
10. T. Sjostrand, Comput. Phys. Commun. 27 (1982) 243; 28 (1983) 229; 39 (1986) 347.
11. W. Kittel, Review Talk at the XXIth Recontre de Moriond, Les Arcs, March 1986.
12. H. Aihara *et al.*, Phys. Rev. Lett. 54 (1985) 2071.
13. B. Anderson, G. Gustafson, G. Ingelman, Phys. Lett. 85B (1979) 17.

14. R. Sosnowski, Proc. 19th Int. Conf. High Energy Physics, Tokyo (1978).

15. A. Breakstone *et al.*, Z. Phys. C25 (1984) 21.

16. A. Breakstone *et al.*, Z. Phys. C27 (1985) 205.

17. A. Breakstone *et al.*, unpublished.

18. B. R. Webber, Nucl. Phys. B238 (1984) 492.

19. S. L. Wu, DESY 83-007.

20. A. M. Smith *et al.*, Phys. Lett. 184B (1987) 293.

21. K. Jaeger *et al.*, Phy. Rev, D11 (1975) 2405; H. Kichimi *et al.*, Phys. Lett. 72B (1978) 411; H. Kichimi *et al.*, Phy. Rev. D20 (1979) 37; S. Erhan *et al.*, Phys. Lett. 85B (1979) 447; D. Drijard *et al.*, Z. Phys. C12 (1982) 217; M. Asai *et al.*, EHS-RCBC Collaboration, Z. Phys. C27 (1985) 11 and the references given therein.

22. Fermilab Computing Department, "ACP Software User's Guide for Event Oriented Processing" FNAL #GA0001 (1988).

23. Ioanis Kourbanis, PhD Thesis, Northeastern University (1989).

24. Sajan Easo, PhD Thesis, Pennsylvania State University (1989).

25. S. Mani, PhD Thesis, University of Pittsburgh (1986); E. Engels Jr. *et al.*, NIM A226 (1984) 59; NIM A253 (1987) 523-529.

26. W. E. Desoi, PhD Thesis, University of Rochester (1990).

27. C. Lirakis, PhD Thesis, Northeastern University (1989); A. Sinanidis, PhD Thesis, Northeastern University (1989).

28. R. Benson, PhD Thesis, University of Minnesota (1990).

29. C. M. Yosef, PhD Thesis, Northeastern University (1990).

30. G. Alverson and Ed Pothier, E706 MAGIC Guide, E706 internal memo #0139 and updates.

31. R. Brun *et al.*, ZEBRA User's Guide, CERN Computer Centre Program Library, DD/EE/85-6.

32. H. J. Klien *et al.*, PATCHY Reference Manual, CERN Computing Library, 1983.

33. J. P. Mansour, PhD Thesis, University of Rochester (1989).

34. K. Hartman, PhD Thesis, Pennsylvania State University (1990).

35. M. Asai *et al.*, EHS-RCBC Collaboration, Z. Phys. C27 (1985) 11.

36. K. Alpgard *et al.*, CERN-EP/82-61 (1982).

37. M. Derrick *et al.*, Phy. Rev D35 (1987) 2639.

38. R. Brun *et al.*, GEANT3 User's Guide, CERN Data Handling Division, DD/EE/84-1 (1987).

39. A. Bassetto *et al.*, Phys. Rep. 100 (1983) 202.

40. M. Bonesini *et al.*, WA-70 Collaboration, Z. Phys. C44 (1989) 71.

41. ISAJET version 6.21, F. paige and S. Protopopescu, Brookhaven National Lab, Upton, NY 11973.

42. R. D. Field and R. P. Feynman, Phys. Rev. D15 (1977) 2590; R. D. Field and R. P. Feynman, Nucl. Phys. B138 (1978) 1.

43. Vincenzo Cavasinni, CERN-EP/89-47, 29 March 1989.

44. Y. I. Azimov *et al.*, Z. Phys. C27 (1985) 65.

45. H. Aihara *et al.*, Phys. Rev. Lett. 53 (1984) 2378.

46. F. Abe *et al.*, Phy. Rev. D40 (1989) 3791.

Nuclear Instruments and Methods in Physics Research A279 (1989) 272–276
North-Holland, Amsterdam

PERFORMANCE CHARACTERISTICS AND RADIATION DAMAGE RESULTS FROM THE FERMILAB E706 SILICON MICROSTRIP DETECTOR SYSTEM *

E. ENGELS, Jr., S. MANI, D. ORRIS, P.F. SHEPARD and P.D. WEERASUNDARA
University of Pittsburgh, Pittsburgh, PA 15260, USA

B.C. CHOUDHARY, U. JOSHI, V. KAPOOR and R. SHIVPURI
Delhi University, Delhi, India

W. BAKER, D. BERG, D. CAREY, C. JOHNSTONE and C. NELSON
Fermilab, Batavia, IL 60510, USA

C. BROMBERG, D. BROWN, J. HUSTON, R. MILLER and A. NGUYEN
Michigan State University, East Lansing, MI 48824, USA

R. BENSON, P. LUKENS and K. RUDDICK
University of Minnesota, Minneapolis, MN 55455, USA

G. ALVERSON, W. FAISSLER, D. GARELICK, M. GLAUBMAN, I. KOURBANIS, C. LIRAKIS, E. POTHIER, A. SINANIDIS, G.-H. WU, T. YASUDA and C. YOSEF
Northeastern University, Boston, MA 02115, USA

S. EASO, K. HARTMAN, B.Y. OH, W. TOOTHACKER and J. WHITMORE
Pennsylvania State University, University Park, PA 16802, USA

G. BALLOCCHI, L. DEBARBARO, W. DESOI, G. FANOURAKIS, T. FERBEL, G. GINTHER, P. GUTIERREZ, A. LANARO, F. LOBKOWICZ, J. MANSOUR, G. PEDEVILLE, E. PREBYS, D. SKOW, P. SLATTERY, N. VARELAS and M. ZIELINSKI
University of Rochester, Rochester, NY 14627, USA

A charged particle spectrometer containing a 7120-channel silicon microstrip detector system, one component of Fermilab experiment E706 to study direct photon production in hadron–hadron collisions, was utilized in a run in which 6 million events were recorded. We describe the silicon system, provide early results of track and vertex reconstruction, and present data on the radiation damage to the silicon wafers resulting from the narrow high intensity beam.

1. Introduction

Fermilab experiment E706 is designed to measure direct photon yields from hadronic interactions in the p_T range 5–10 GeV/c. The experiment will also investigate hadronic jets produced in association with high p_T photons and the production of high mass ($m > 3$ GeV) e^+e^- and $\gamma\gamma$ states. E706 is a fixed target experiment using a high energy beam (800 GeV/c) of primary protons from the Fermilab Tevatron to produce both positive and negative 530 GeV/c secondary beams. The detectors are triggered on $p_T > 3.5$ GeV/c electromagnetic showers.

Fig. 1 shows a floor plan of the spectrometer in the M West laboratory. The apparatus for E706 consists of an array of silicon stip detectors (SSDs) before and

* Work supported in part by US DOE Contract no. DE-AC02-80ER 10667.

0168-9002/89/$03.50

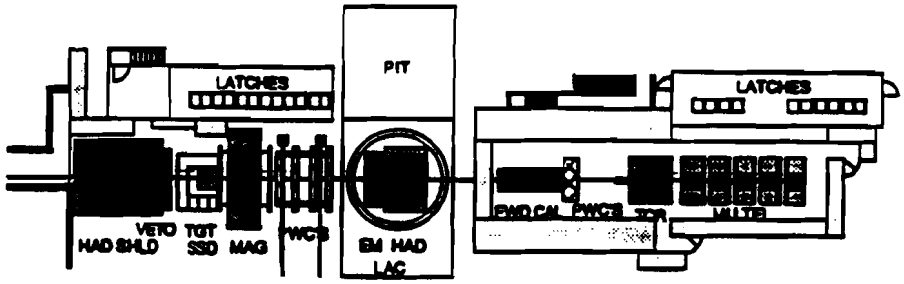

Fig. 1. Floor plan of the E706/672 spectrometer in the M West laboratory.

after a production target, a set of proportional chambers (PWCs) located after an analysis magnet, a large liquid argon calorimeter (LAC), and a small steel/plastic scintillator forward calorimeter. The forward calorimeter is followed by a muon system provided by E672 utilizing a toroidal magnet in conjunction with PWCs to identify muons.

The SSDs together with the PWCs after the analysis magnet constitute a magnetic spectrometer designed to measure the momenta of charged particles in hadronic jets associated with high p_T photons. In addition the SSDs serve as a vertex detector which accurately locates the position of primary and secondary interactions in the segmented target. The LAC [1] measures the position and energy of both photons/electrons and hadrons. The LAC has a central hole of 40 cm diameter; this area is covered by the forward calorimeter. Below we will restrict the discussion to only the SSD system.

2. SSD system

Fig. 2 shows the SSD/segmented target region. There are 7 X–Y modules or 14 SSD planes with a total of 7120 active strips. All of the SSDs have a 50 μm pitch and a thickness of 250–300 μm. The three X–Y modules upstream and the first X–Y module immediately downstream of the target contain 3×3 cm^2 wafers; the wafers of the last three X–Y modules are 5×5 cm^2. The size of SSD planes shown in fig. 2 is determined from the region of the wafer which is instrumented with preamplifiers. The segmented target appears to be optimum for efficiency of track reconstruction, primary vertex location, and secondary interaction vertex identification.

The E706 charged particle spectrometer was designed to operate at a 1 MHz interaction rate. The readout system provides digital information on the traversal of strips by minimum ionizing particles with high efficiency and small dead time. A minimum ionizing particle traversing one of our detectors produces $(2.0–2.4) \times 10^4$ electron–hole pairs, depending on the thickness of the wafer, and the charge is collected in ~ 20 ns. This charge is then fed into a Rel-Lab IO-323-C charge sensitive preamplifier. The output of these preamplifiers must be further amplified, then discriminated, and converted to logic signals for storage as digital data. Fig. 4 shows the entire readout system. The second stage amplifier–discriminator, latches, latch controllers and computer interface are manufactured by Nanometrics Systems, Inc. While this Nanometric system is designed primarily for use in reading out PWC information, we have adapted it for use with the SSD system so that the SSD and PWC systems in E706 have identical readout electronics past the preamplifier stage of the SSDs. The ECL data from the N-277C are latched into the N-278 latches which are controlled by

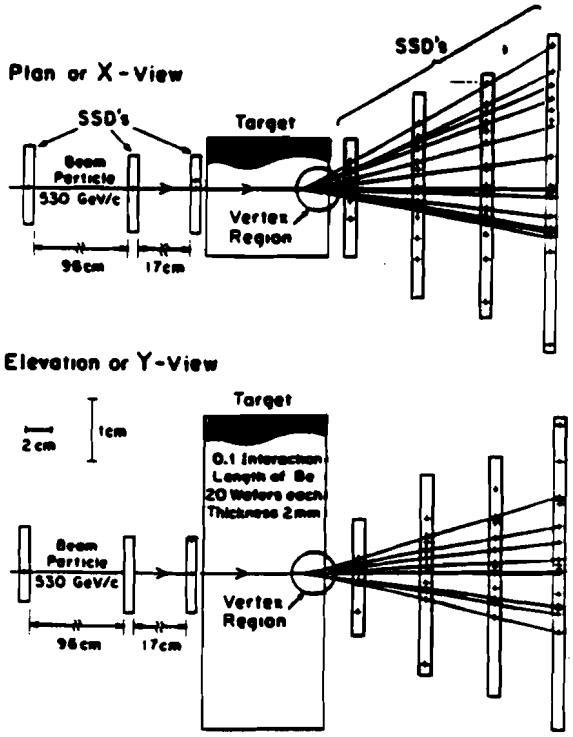

Fig. 2. Schematic of the segmented target/SSD system of E706. A typical multivertex event is superimposed on the planes.

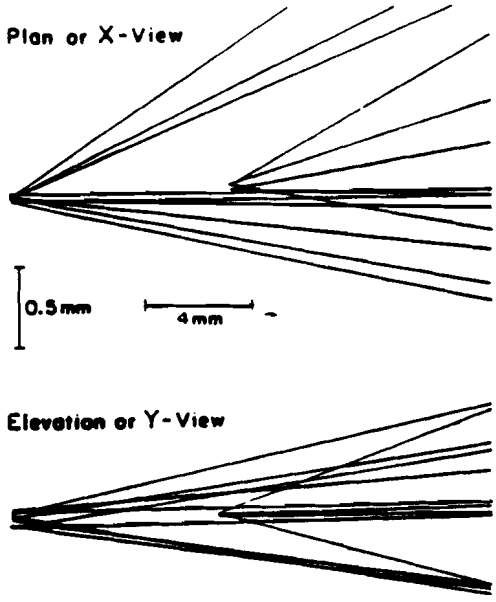

Fig. 3. An enlargement of the vertex region of the multivertex event.

the N-280 dedicated controller, all housed in standard CAMAC crates. The readout time of data from the latches to the controller is a maximum of 5 μs. The transmission of data from the controllers is done on an RS-422 data bus to the N-281 interface which is in turn monitored by a PDP-11 computer. The PWCs are read out by the same PDP-11 and the data are sent to a micro-vax for concatenation with the data from the other parts of the spectrometer.

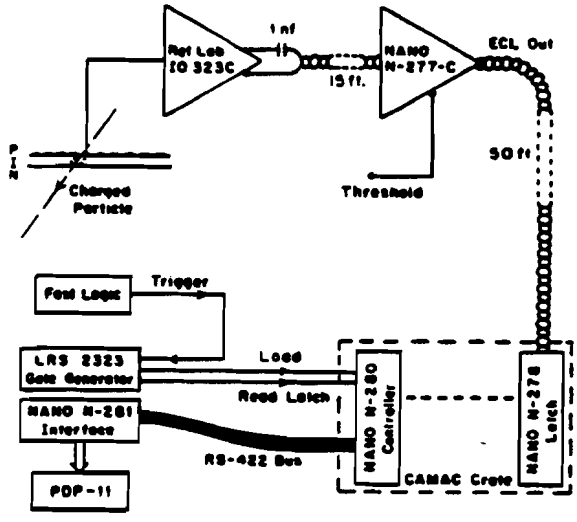

Fig. 4. A schematic of the readout electronics for the SSD system.

3. Track and vertex reconstruction

Fig. 2 shows a reproduction of an actual event observed during the course of the 1987–88 E706 data run in which 6 million events were recorded on magnetic tape. The elongated rectangles represent the instrumented region of the silicon wafers and the crosses within the rectangles represent the location of a "hit" resulting from a particle having traversed a silicon strip at that location. The straight lines connecting the "hits"

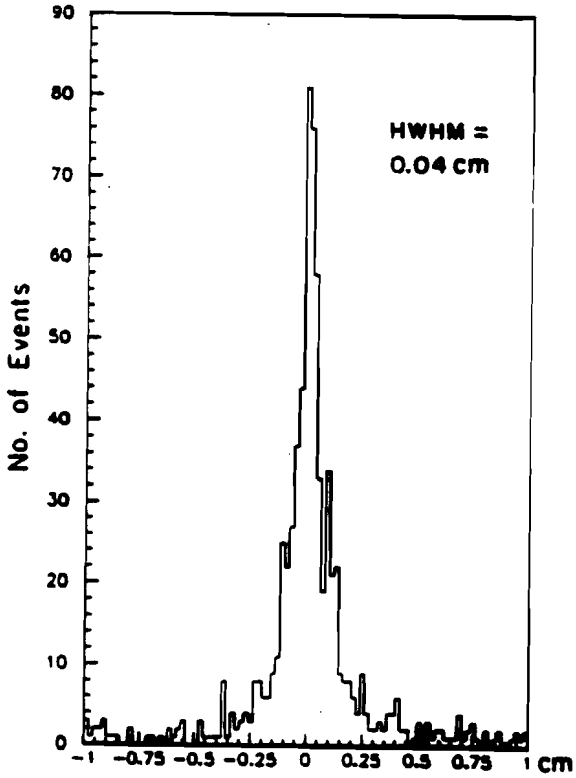

Fig. 5. The difference between the location along the direction of the beam of the vertices determined independently in the X and Y projections.

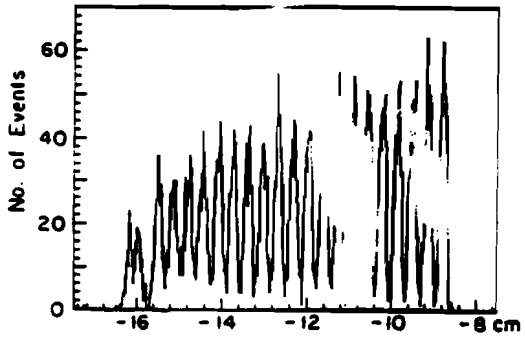

Fig. 6. A sample of events plotted as a function of their vertex location along the direction of the beam.

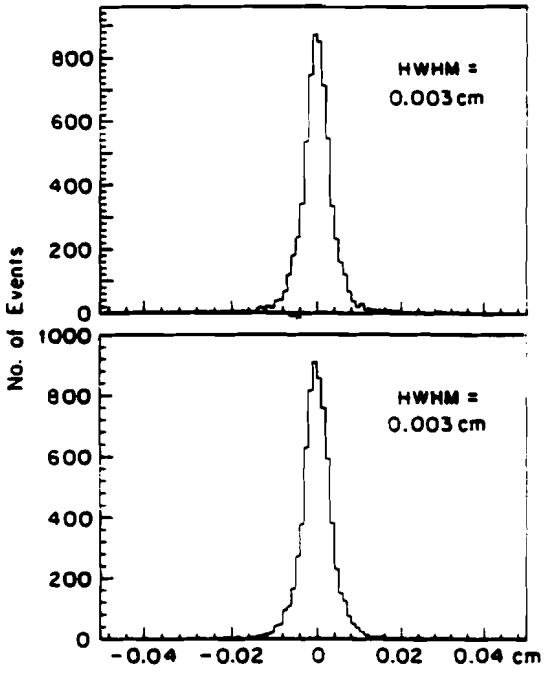

Fig. 7. A plot of the impact parameters of each of the secondary particles used in determining the location of the vertex in X and Y.

are the fitted tracks which converge at the vertex location. Only the four-hit tracks after the target have been drawn and there are a few three-hit tracks not shown in the figure.

The event shown is a multivertex event which is clear by examining fig. 3 which shows an enlargement of the vertex region of the event. The secondary vertex, which is probably due to a secondary interaction, is approximately 8 mm downstream of the primary vertex.

Fig. 5 is a plot of the difference between the location along the direction of the beam of the vertices determined independently in the X and Y projections. The HWHM value associated with the peak is 0.04 cm (400 μm). This measured value is in agreement with calculations that include the instrumental resolution as well as the multiple scattering of the secondary particles used to determine the vertex position. Fig. 6 is a plot of a sample of events plotted as a function of their vertex location along the direction of the beam. Apparent in this figure is the segmented structure of the target which consists of wafers of Be each of thickness equal to 2 mm and separated from the adjacent wafers by 1.6 mm. The small double-peak structure appearing at about the −16 cm location is due to the presence of two thin copper sheets located just upstream of the segmented Be target. Since the beam moves from left to right in this figure, it is apparent that the vertex resolution in the upstream Be wafers is slightly poorer than in the more downstream wafers. This difference is due to increased multiple scattering of secondary particles produced in the upstream interactions which experience a greater degree of multiple scattering in the subsequent target material, and the increased lever arm between the upstream interactions and the X–Y modules downstream of the target.

Fig. 7 is a plot of the impact parameters of each of the secondary particles used in determining the location of the vertex in X and in Y. The impact parameter in the X-view is the x coordinate of a secondary particle track minus the x value of the vertex location, both measured at the z value (coordinate along the beam line) of the best estimate of the vertex location. The HWHM value associated with the peak of the curve is 0.003 cm (30 μm). This value is also in agreement with calculations involving apparatus resolution and multiple scattering.

4. Radiation damage to silicon wafers

An array of p–i–n diodes, which is the basic structure of a silicon microstrip detector, exhibits the feature that the reverse-bias current under conditions of full

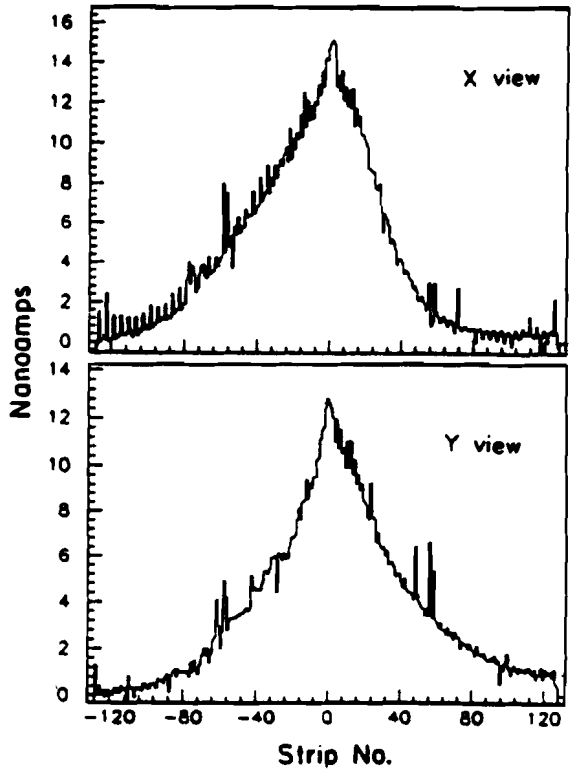

Fig. 8. A plot of the increase in leakage current per strip of the two most upstream wafers. These two curves agree with the measured beam profiles in the X and Y projections.

depletion increases linearly with the exposure to ionizing radiation. A parameter used to describe this effect is α, defined by the equation $I_L = \alpha\Phi$. I_L is the reverse bias (leakage) current in units of nA/cm^3. Φ is the integrated particle flux that has passed through the diode in units of particles/cm^2 and hence α is in units of nA/cm. The quantity α is of interest to experimenters using SSDs because of the impact of increased leakage current due to radiation damage on the design of the preamplification stage of the apparatus and because of the increased noise associated with the increase in leakage current.

Fig. 8 is a plot of the increase in leakage current per strip of the two most upstream wafers in the apparatus plotted as a function of strip number. These two curves agree with the measured beam profiles in the X and Y projections. Prior to exposing these wafers to beam, the leakage current per strip varied between 2 and 3 nA. As can be seen in the figure, the strips corresponding to the peak beam intensity experienced increases in leakage current up to as much as 14 nA during the data run. The integrated beam during the data run equaled 1.2×10^{12} particles which corresponds to an intensity at the peak of the profile equal to 8.3×10^{12}/cm^2.

Our values for the parameter α for the two wafers are:

$\alpha(X \text{ wafer}) = (3.0 \pm 0.2) \times 10^{-8}$ nA/cm,

$\alpha(Y \text{ wafer}) = (2.9 \pm 0.2) \times 10^{-8}$ nA/cm.

The error quoted in the above values reflects the uncertainty in subtracting the leakage current from each strip before the wafers were irradiated. We estimated this uncertainty to equal ± 0.25 nA/strip. There is an additional systematic uncertainty in the measurement of the total beam flux to which the detectors were exposed of approximately 5%.

Reference

[1] F. Lobkowicz et al., Nucl. Instr. and Meth. A235 (1985) 332.